UNIVERSIDAD Ð LA LAGUNA
Departamento de Astrofísica

Study of binary central stars of planetary nebulae with GALEX and corollary optical surveys

Memoria que presenta
D. Marco Antonio Gómez Muñoz
para optar al grado de
Doctor por la Universidad de La Laguna

INSTITUTO Ð ASTROFISICA Ð CANARIAS
Julio de 2020

Examination date: July 28th, 2020
Thesis supervisor: Dr. Arturo Manchado Torres
Tutor: Dr. Cesar Esteban Lopez
Thesis co-supervisor: Dra. Luciana Bianchi

Some of the material included in this document has been already published in *The Astrophysical Journal*.

A mi hija Ainhoa,
a mi esposa Viviana

Agradecimientos

Por fin. Después de tanto trabajo duro, por fin he terminado lo que parecía desde el principio algo muy lejano. Esto que presento aquí, esta tesis que me ha llevado a estar 4 años fuera de casa, refleja el trabajo duro de quienes estuvieron detrás mio, apoyándome. Primero que nada, agradecer a mis padres, Marco y Martha, por la paciencia y la perseverancia que en su momento hubo conmigo, pues de los dos hijos que tienen, no fui el mas facilito. Gracias infinitas por que sin su ayuda y sin su apoyo, siempre incondicional, no hubiera llegado hasta donde he llegado– y gracias además por enseñarme a ser quien soy, por creer en mi y por apoyarme y seguirme en mis ideas a donde quiera que fuese. Gracias también a mi hermana, Anais, quien ha tenido que soportar todas mis platicas de ciencia desde que inicie la cerrera en la Universidad, por su apoyo, su cariño y su comprensión.

Le doy gracias infinitas a mi esposa, Viviana, que sin ella esto no hubiera sido posible– ya te digo. Agradezco el sacrificio que fue abandonar todo en México, embarazada de 5 meses, para acompañarme en esta aventura en tierras lejanas, y por haberme dado una hija hermosa, quien ahora es una de mis mas grandes motivaciones para seguir adelante. Hija, si algún día te tomas la molestia de leerte este mamotreto, quiero que me disculpes por haber faltado muchas veces, y por haber perdido la paciencia en ocasiones donde lo único que querías era jugar. Esta tesis está dedicada a ustedes. Muchas gracias!

Quiero agradecer también al Insituto de Astrofísica de Canarias por haberme dado la oportunidad de hacer esta tesis. En este tiempo, muchas cosas han cambiado, he aprendido algunas y seguramente he olvidado otras, pero no quiero olvidarme de las personas a las que les debo este trabajo. En primer lugar, agradecer a mis directores de tesis, Arturo Manchado y Luciana Bianchi, quienes han luchado conmigo y han estado allí para darme comentarios y correcciones que han sumado y que han mejorado el trabajo que aquí presento. Gracias Arturo, por los consejos, y la sabiduría que has compartido conmigo–

he aprendido mucho– y gracias por que cuando la situación se puso fea (por el Covid-19) te mantuviste al tanto del progreso del trabajo, y no solo eso, si no también de que no nos faltase algo en casa. Quiero agradecer especialmente a Anibal, que ademas de ser una persona con gran calidad humana, siempre estuvo allí apoyándome y dándome palabras de motivación cuando la cosa parecía no ir muy bien. Gracias por esas charlas en el café, y por esos empujones que siempre son necesarios para no perder el rumbo de la cosas. Gracias al resto del grupo, Thomas, Olga, y Victor, por el buen trato y por la ayuda que me brindaron, tanto emocional como técnica, durante este tiempo.

Este trabajo también se debe a mis amigos, Kuba, Salvo y Camilo, que me aceptaron desde el primer día que llegue y me brindaron su amistad y su cariño. Gracias chicos, por todo el apoyo durante el tiempo que he estado aquí, gracias por esas invitaciones a comer, y por esas veces en que necesité algunas cachetadas para dejar de pensar en el trabajo y concentrarme en lo que tengo en casa. Sin ustedes chicos, la estadía no hubiese sido así de amena. Kuba!!, no tengo palabras para agradecer tu amistad y tu apoyo, amigo, gracias infinitas.

A Karla y Eduardo, por esas escapadas del trabajo, que aprovechábamos para ponernos al día y chismear por las tardes, por qué no?, con una taza de café. Y también por esas discusiones científicas que solíamos hacer cuando no estábamos de acuerdo con alguna publicación y/o comentarios de otros. También quiero agradecer a Jorge por sus consejos y por sus enseñanzas sobre abundancias químicas, que me ayudaron a sacar el primer artículo de este trabajo (que irónicamente es el último capítulo).

No me podré olvidar nuca de las personas que me motivaron a hacer este viaje, y a seguir por el camino del "lado oscuro". Gracias a la familia que formé en Ensenada, formada por Roberto, Mónica, Paco, Laurence, Luis Carlos, y Rodrigo. Roberto ¿qué te puedo decir?, gracias infinitas por todo el apoyo que me diste durante mi maestría, y por el tiempo, dinero y esfuerzo, para que todo esto fuera posible. Gracias por ser mi amigo, y por ser esa persona empática y por tener esa gran calidad de ser humano que te caracteriza. Mónica!, sin ti no me hubiera motivo a hacer lo que hice, sin tu experiencia y sin tus consejos, no hubiera terminado donde estoy ahora, gracias por haber sido esa inspiración que necesitaba. Paco, Luis, y Roy, gracias por su amistad, y por su apoyo, esto tampoco se hubiera logrado sin ustedes!.

Marco A. Gómez Muñoz

Resumen

Las nebulosas planetarias (PNe del inglés "planetary nebulae") son estrellas de masa baja e intermedia (0.8−8.0 $M_{\odot}$) que se encuentran en una fase evolutiva tardía entre la Rama Asintótica de las Gigantes (en inglés, Asymptotic Giant Branch, AGB) y la etapa de Enanas Blancas (en inglés, White Dwarfs, WD). En los últimos años se ha demostrado que la mayoría de las PNe (más del 80%) no son esféricas, presentando morfologías que van desde aquellas ligeramente elípticas hasta las que presentan lóbulos bipolares (o multipolares) y estructuras compactas con simetría puntual.

El objetivo de esta tesis es explorar la manera en que la binariedad afecta la evolución de estrellas de baja masa e intermedia en la fase de PNe. La metodología empleada ha consistido en determinar las distribuciones espectrales de energía (SED del inglés "spectral energy distribution") de estos objetos en un amplio rango de longitudes de onda, desde el ultravioleta hasta el infrarrojo cercano, con el objetivo de establecer la presencia de dobles picos o excesos de color indicativos de la presencia de una compañera fría.

Como punto de partida se utilizaron los catálogos de objetos en esta fase encontrados en la literatura, y la base de datos del satélite Galaxy Evolution Explorer (GALEX). En particular, las observaciones del satélite GALEX, que observó en el rango ultravioleta, son especialmente adecuadas para detectar las estrellas centrales de las PNe, cuya elevada temperatura efectiva es elusiva en las longitudes de onda ópticas. En la zona visible se han utilizado datos del Sloan Digital Sky Survey (SDSS) y del Panoramic Survey Telescope and Rapid Response System (PanSTARRS), que proporcionan 5 magnitudes en el óptico (SDSS *ugriz* y PS1 *grizy*). Estas bandas se han utilizado para correlacionar las PNe encontradas en GALEX con sus contrapartidas en el rango óptico. Hemos clasificado las PNe como resueltas (aquellos que tienen resolución espacial) cuando la PN presenta un brillo superficial mayor a dos veces la resolución de GALEX (∼5 ″), y como PNe no resueltas aquellos que no cumplan con este

criterio. Además, para las PNe resueltas se ha extraído el flujo de la estrella central usando fotometría de apertura. Estos datos se han recopilado en un catálogo, al que denominamos GPNcatxSDSSDR14xPS1DR2, y que contiene 326 PNe con fotometría UV-óptica de las cuales 222 son resueltas.

Un paso fundamental para comprobar la validez de la teoría binaria es analizar las SED de estrellas centrales de PNe sin tener en cuenta la morfología (para no sesgar la muestra). Se extrajo una muestra de 22 PNe catalogadas como resueltas en GPNcatxSDSSDR14xPS1DR2, seleccionada en base a sus colores en diagramas color-color y a su brillo superficial. Para analizar la muestra hemos construido un programa que identifica y caracteriza las estrellas centrales de PNe binarias, basado en la técnica de Marckov-Chain Monte-Carlo (MCMC). Se han podido caracterizar 22 estrellas centrales, resultando en 11 sistemas binarios confirmados de los cuales 7 son nuevas detecciones.

Para analizar las PNe no resueltas, se ha creado una malla de modelos de fotoionización utilizando el programa CLOUDY con el fin de tener una red de magnitudes sintéticas en las bandas UV-ópticas. Se analizó la contribución tanto de líneas de emisión nebulares como del continuo nebular en cada banda fotométrica. Con el fin de delimitar la posición de las PNe en el espacio de colores y en el futuro detectar nuevos objetos, hemos comparado nuestros modelos de magnitudes de las PNe con otros modelos teóricos y con observaciones de diferentes objetos astronómicos. Así mismo, se añadió a cada SED sintética un modelo de una estrella fría compañera para identificar la posición de las PNe con núcleos binarios en los diagramas de color. Hemos encontrado que el diagrama color-color GALEX FUV$-$NUV versus SDSS $r-i$ es el mejor para separar tanto las PNe como las PNe con estrellas centrales binarias (sobre todo con estrellas compañeras gigantes).

Finalmente, como caso particular, presentamos el análisis de la PN con núcleo binario NGC 2346 basado en datos de archivo del Explorador Internacional UV (IUE del inglés International Ultraviolet Explorer) y de observaciones de espectros ópticos de baja y alta resolución (3700$-$7300 Å). Al incluir en el análisis espectral la contribución del continuo estelar y nebular, hemos resuelto la discrepancia en el cálculo de la extinción, siendo este $E(B-V)$=0.18. Hemos reclasificado a la estrella compañera como A5IV mediante el análisis de las líneas de absorción de Balmer presentes en el espectro óptico de alta resolución (R=67 000). Usando la distancia Gaia de 1400 pc se construyó un modelo de fotoionización basado en las abundancias derivadas del espectro óptico de baja resolución obteniendo valores para la $T_{\rm eff}$ y luminosidad de 130 000 K y 170 $L_{\odot}$, respectivamente. Concluimos que el progenitor de NGC 2346 ha experimentado la fase de envoltura común en donde la estrella compañera ha acretado masa y por tanto evolucionado fuera de la Secuencia Principal.

Abstract

Planetary Nebulae (PNe) are the descendants of low- and intermediate-mass stars (0.8−8.0 $M_{\odot}$). The shape of the PN takes place at some point between the asymptotic giant branch (AGB) and the white dwarf (WD) stellar phases. Among the astrophysical phenomena, the PNe shows an impressive variety of complex morphologies. In fact, most of the PNe known are not spherical (more than 80%) and present shapes from slightly elliptical to bipolar (or multipolar), as well as knots and/or collimated outflows at high velocities, reaching 600 kms^{-1} in the most extreme cases.

The aim of this thesis is to explore how binarity affects the evolution of low- and intermediate-mass stars during the PN phase. We started by looking for photometric data of the known central stars of PNe (CSPNe) in different databases (from the ultraviolet to the near-infrared) in order to search for a double spectral energy distribution (SED) composed by a hot-star (the ionizing star) and a cool companion star.

We compiled a catalog of PNe by combining the coordinates PNe catalogs found in the literature, and matched them with the *Galaxy Evolution Explorer* (GALEX) database (GPNcat). The FUV and NUV photometry, included in GALEX, allow us to extract the hottest stellar objects, which are elusive in optical wavelengths due to its $T_{\rm eff}$ and luminosity. We matched the GPNcat with *Sloan Digital Sky Survey* (SDSS) and the *Panoramic Survey and Rapid Response System* (PanSTARRS) databases (GPNcatxSDSSDR14xPS1DR2), both providing five magnitudes in the optical range (SDSS *ugriz* and PS1 *grizy*). We separated the resolved PNe, with sizes (diameters) at least twice the resolution of GALEX, from unresolved PNe. For resolved PNe, the flux of the CS were isolated by using aperture photometry techniques. The final catalog, `GPNcatxSDSSDR14xPS1DR2`, contains 326 PNe with both UV and optical photometry of which 222 are resolved.

Most of the PNe are not spherical, and current single-star models cannot

explain the morphologies we observe. A binary interaction is the preferred channel to form non-spherical PNe. A fundamental step to corroborate this is to take a sample of PNe without discriminating the morphologies and analyze their CS. We search for spatially unresolved optical excess, by combining GALEX UV with optical SDSS and PS1 photometry, in a sample of 23 resolved CSPNe extracted from `GPNcatxSDSSDR14xPS1DR2`. We selected the PNe to be analyzed according to their colors in the color-color diagram and according with the accuracy of the match with its UV and optical counterparts. We have constructed a program to identify and characterize binary central stars of PNe based on the Markov-Chain Monte-Carlo (MCMC) method. We have characterized 11 binary CSPNe of which 7 are new binary CSPNe candidates.

We constructed a grid of synthetic SED of PNe using the photoionization code CLOUDY, obtaining synthetic magnitudes in GALEX FUV and NUV, and SDSS and PS1 optical bands. We compared our model colors with other theoretical and observed colors for different astrophysical objects to identify the position of PNe in the color space. After identification of PNe in the color space, we added a cool companion to each model SEDs to identify PNe with binary CS. We found that GALEX FUV−GALEX NUV versus SDSS r−SDSS i and GALEX NUV−SDSS r versus SDSS r−SDSS i color-color diagrams are the best ones for cleanly separating PNe and PNe with binary CS from other astrophysical objects.

Finally, as a particular case of study, we present an analysis of the binary central star of NGC 2346 based on archival data from the *International Ultraviolet Explorer* (IUE), and new low- and high-resolution optical spectroscopic observations. By including the stellar and nebular continuum, we reconciled long-time discrepancy UV and optical diagnostics from the literature and derived $E(B-V) = 0.18 \pm 0.01$. We classified the companion star's spectral type as A5IV by analyzing the wings of the Balmer absorption lines in the high-resolution (R=67 000) optical spectra (3700−7300 Å). Using the distance to the nebula of 1400 pc from Gaia DR2, we constructed a photoionization model based on abundances and line intensities derived from the low-resolution optical spectra to obtain the temperature ($T_{\rm eff}$=130 000 K) and luminosity (L = 170 $L_\odot$) of the ionizing star, which are consistent with the UV continuum. This analysis allows us to better constrain the binary system. We concluded that the progenitor star of NG 2346 has evolved through a common envelope phase, in which the companion star has evolved off the main-sequence.

Contents

1

Introduction

1.1 The origin of planetary nebulae

The planetary nebulae (PNe) are one of the most beautiful and impressive objects in the Universe; owing to the variety of complicated morphologies they are produced at the end of the life of low- and intermediate-mass stars ($0.8 \lesssim M \lesssim 8.0\,M_\odot$). The first PN was observed by Charles Messier in 1764 and was given number 27 in his catalog of nebulous objects. William Herschel assigned in 1785 the name of 'planetary nebula' as they vaguely reassemble the disk of a planet. After advanced telescopes appeared, the PNe become a separate object from other gaseous astronomical sources made up of stars (galaxies). William Huggins verified this distinction in 1864 with the first spectrum ever made of a PN, NGC 6543. He found that the spectrum of a PN is composed of emission lines, unlike the continuous spectrum of stars. PNe showed a definite structure and were tied to a hot central star, called white dwarf (WD, Shklovsky, 1956). Shklovsky (1956) stated that WDs descended from PNe and that red giants are the precursors of PNe. The need to consider PNe as one of the phases of stellar evolution was inevitable, and a few years later, Paczyński (1970,1971) described the PNe in terms of the Hertzsprung-Russel (H-R) diagram.

As we have mentioned above, PNe represent a key evolutionary stage in the evolution of low- and intermediate-mass stars. Figure 1.1 shows the relevant evolutionary phases of low- and intermediate-mass star in the H-R diagram. These stars spend most of their lives on the main sequence (MS) burning hydrogen (H) in their core. When the H in the nucleus is exhausted, the helium (He) core contracts and, for stars with masses less than $2.5\,M_\odot$, this core becomes de-

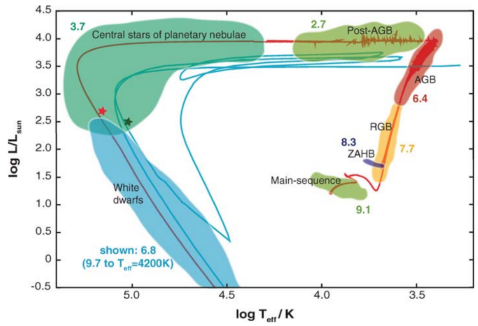

FIGURE 1.1— H-R diagram of a $2\,M_\odot$ evolution track for solar metalicity (red). The blue track shows a born-again evolution. The number labels for each evolutionary phase indicates the log approximate duration for a $2\,M_\odot$, in years. Adopted from Herwig (2005).

generated. At this point, the H fusion starts in a shell around the nucleus, and the star moves to the red giant branch (RGB) phase. The He-degenerate cores during the RGB phase are the product of the evolution of low-mass stars and they experience the so-called He-flash (when the He core grows to $\sim 0.45\,M_\odot$). However, intermediate-mass ($M \gtrsim 2.5 M_\odot$) stars can initiate core He burning under non-degenerate conditions and develop an electron-degenerate carbon-oxygen (C-O) nucleus after the He exhaustion. The temperature in the core increases and at some time becomes high enough to begin He-burning in the core, placing the star on the horizontal branch (HB). After the HB phase, both types of stars (low- and intermediate mass) moves to the asymptotic giant branch (AGB) phase where the star experience thermal pulses (the alteration of H- and He-burning in the shell) and starts mass loss (up to $10^{-5}\,M_\odot\,yr^{-1}$) (see e.g., Karakas & Lattanzio, 2014, for a review). The most important nucleosynthesis process (both light and heavy neutron-rich elements; Karakas & Lattanzio, 2014) take place during the AGB phase, and they will mark the following evolutionary phases (e. g., C−rich versus O−rich objects). The AGB phase ends with the complete removal of the external shells (H envelope) by the strong mass loss.When the strong AGB mass loss ceases and after a brief transition phase (the post-AGB phase; $\sim 10^2 - 10^4$ yrs), what remains in the

center is the hot compact central star. Eventually, the ultraviolet (UV) photons of the central star as well as shocks, can ionize the previously ejected envelope forming what we know as a PN.

1.2 Asymmetries in PNe

The formation of the PN occurs during a brief ($\sim 10^2 - 10^4$) post-AGB phase. Kwok et al. (1978) first proposed that the simplest morphological features (spherical or ellipsoidal) of PNe were the result of the interactive stellar wind (ISW), where the hot core (the central star of the PN; CSPN) low-density supersonic wind and radiation shape and ionize the previously expelled AGB shell (the slow-dense wind). However, many PNe show asymmetrical morphologies (see Figure 2). In a large PNe sample (225), taking into account projection effects, only 20% were found to be round, while the rest presented some asymmetries (63% were elliptical and 17% bipolar; Manchado, 2004). The fraction of bipolar PNe may be higher because bipolar PN would appear round if seen pole-on (Balick et al., 1987; Guerrero et al., 1996; Jones et al., 2012). Plausible explanations for the formation of bipolar PNe postulate a dense equatorial disk, produced by mass-loss in earlier phases, which collimates the fast stellar wind from the hot CSPN in the post-AGB phase (e.g., Balick et al., 1987; Icke, 1988; Icke et al., 1989; Mellema et al., 1991; Frank & Mellema, 1994). However, Soker (1992), and more recently García-Segura et al. (2014, 2018), have shown that a single star's angular momentum, or surface rotation, cannot produce a sufficient equatorial density enhancement. Also, the AGB wind asphericities could naturally arise in a binary system, via common envelope (CE) evolution in the initial phase of spiraling-in, when the interaction of the companion with the red giant's extended atmosphere causes about 25% of the CE to be ejected from the system (Sandquist et al., 1998; Ricker & Taam, 2012). Another mechanism that can explain the observed asphericities in PNe is called gravitational focusing; in close binaries the density distribution of the slow AGB wind is significantly modified by the gravity of the secondary, resulting in an enhanced density region close to the orbital plane of the system, and low-density regions elongated perpendicularly to the orbital plane (Gawryszczak et al., 2002).

Out of more than 2000 known PNe (Miszalski et al. 2012), only forty binary CSPNe are currently known; sixteen of which are post-CE systems. Most of them have been discovered through photometric variability, which favors the detection of periods shorter than three days (see Figure 1.3).

The binary interactions have become the preferred scenario for the formation of aspherical PNe and presently considered crucial evidence for CE evolution

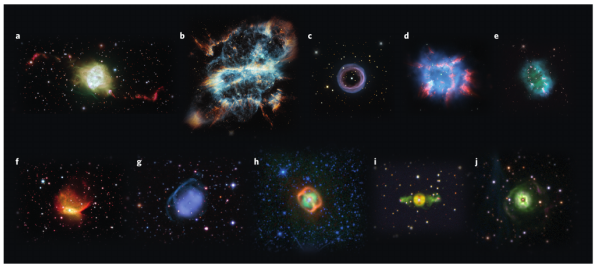

FIGURE 1.2— A selection of PNe known to host binary CSs and displaying a variety of morphologies (from round/elliptical to bipolar/multipolar). a) Fleming 1; b) NGC 5189; c) Shapley 1; d) NGC 6326; e) The Necklace; f) Hen 2-428; g) Abell 65; h) NGC 1514; i) ETHOS 1; and j) Hen 2-39. Adapted from Jones & Boffin (2017a).

(see Jones & Boffin, 2017a, for a review). The CE is a short-lived phase in the life of a binary system during which the two stars orbit inside a single shared envelope (Ivanova et al. 2013).

1.3 Detecting binary CSPNe

The first confirmed binary CS – UU Sagittae, the CS of Abell 63 – was found in 1976 by comparing the catalog of Galactic Planetary Nebulae and the General Catalog of Variable Stars (Bond, 1976). Since then, a small number of binary CSPNe were known from detailed individual studies (Bond & Livio, 1990; Bond, 2000). Many more binary CSPNe has be found with the increasing number of photometric surveys (e.g., Miszalski et al., 2008, 2009).

Now days, different methods exist that are used to find binary CSPNe. In this section, we discuss the most widely used: Photometry variability, Infrared excess, and Radial Velocity variations. We also discuss the method that we implemented in this thesis, based on a composite spectral energy distribution (SED) using the photometric information of the *Galaxy Evolution Explorer* UV catalog and its optical counterpart.

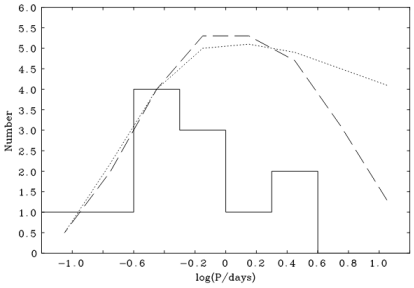

FIGURE 1.3— Histogram of the known irradiated companions by the hot star. The histogram shows a disproportinate number of systems with a period of less than one day compared to longer periods (solid line). Dashed line: predicted period histogram from Han et al. (1995) for post-CE binaries with a main-sequence companion where the ejection of the envelope was relatively inefficient. Dotted line: predicted period histogram from Han et al. (1995) for post-CE binaries with a main-sequence companion where the ejection of the envelope was relatively efficient. Figure from the work of De Marco et al. (2008).

1.3.1 Photometric variability

Detection methods for binary CSPNe have been centered on the light variation technique, where a central, unresolved binary undergoes eclipses, suffers ellipsoidal distortion or where the luminous hot CSPN irradiates the cool companion. This method is responsible for the detection of most of the known binary CSPNe.

? used the photometric variability techniques to detect binaries via periodic variability due to irradiation of the cool companion by the hot star. This photometric survey has taken place over three decades and found that 10% to 15% of about 100 monitored CSPNe are close binaries with periods shorter than 3 days. Most of the periods have been proven to be less than 1 day (De Marco et al., 2008). Miszalski et al. (2009) used the Optical Gravitational Lensing Experiment (OGLE) II and III surveys to carry out similar searches for periodic binaries, detecting 21 periodic variables CSPN (see Figure 1.4).

The main caveats of this method are that it is biased against; 1) binaries that have the orbital plane near the plane of the sky; 2) longer period binaries

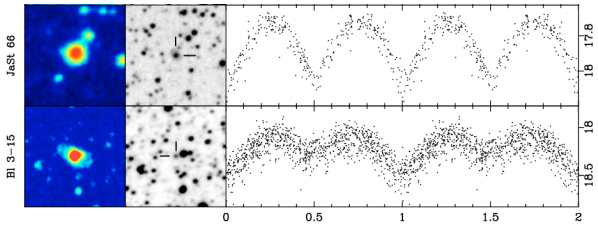

FIGURE 1.4— Images and phased lightcurves of 2 confirmed binary CSPNe. Each row per panel depicts *left-to-right*: H_α image of the nebula, an OGLE $I-$band image, and a phase OGLE $I-$band lightcurve of the CS. Image adapted from Miszalski et al. (2009).

(more than three weeks); and 3) companions with a very small stellar radius (less than $1\,R_\odot$).

1.3.2 Infrared Excess

One of the most popular methods is the infrared (IR) excess technique. The pioneers of this technique were Zuckerman et al. (1991), and a few years later Frew & Parker (2007). Due to the fact that most of the companion stars of the CSPNe are in to the main-sequence, they can be detected in a spatially unresolved binary system because the CS radiates primarily in UV wavelengths, and the main-sequence companion star radiates mostly in the red and IR wavelengths. This technique requires at least two blue photometric bands and one IR band. The blue bands are mainly used to correct for interstellar extinction by comparing the observed colors (normally the $B-$ and $V-$bands) with a stellar atmosphere model appropriate for high temperatures (i. e., to model the emission of the ionizing CSPN). After correcting the photometry with the derived interstellar extinction, a comparison of the difference between the modeled colors and the observed colors (normally the $I-$ or $J-$band) is made to detect the IR excess (e.g., De Marco, 2009; Douchin et al., 2015; Barker et al., 2018). An example of this method can be seen in Figure 1.5, adapted from Bilikova et al. (2009).

Although this method is widely used to calculate the binary fraction of PNe by searching for IR excess in the $I-$ and $J-$band fluxes (De Marco et al., 2013; Douchin et al., 2015), or in the $i-$ and $z-$bands of the Sloan Digital

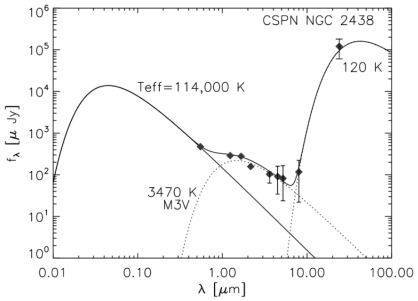

FIGURE 1.5— The SED of the CSPN of NGC 2438 is fitted with three blackbody curves; implying the presence of a hot-star ($T_{\rm eff}$=114 000 K), an M3V (∼3470 K) and of dust (120 K) companion. Taken from Bilikova et al. (2009).

Sky Survey (SSDS) (Douchin et al., 2015; Barker et al., 2018), the IR excess method is mostly biased toward finding low-mass main-sequence companions, given that the principal assumption to obtain the reddening correction is that the companion is not contributing to the flux in the blue bands. Furthermore, little evidence of more evolved companions are found in the literature (e.g., Abell 70 and NGC 2346; Miszalski et al., 2012; Gómez-Muñoz et al., 2019, respectively).

1.3.3 Radial velocity

Another method to search for binaries is via periodic radial velocity (RV) variations of the stellar lines. This method is based on the *Doppler effect*. In a binary system, the barycenter of the system is located between the two stars (depending on the mass ratio). Over the last 30 years only a few surveys used this method (see De Marco, 2009, for a review). Méndez (1989) took 1−5 high-resolution spectrograms of each CSPN in a sample of 28 objects and concluded that 18% were variable. A few years later, Sorensen & Pollacco (2004) carried out a survey at intermediate resolution and determined that 39% of their sample (33 objects) were RV variables. More recently, Dr. David Jones lead a long-term monitoring campaign of several CSPNe (e.g., Jones & Boffin, 2017b; Jones et al., 2017, 2019). As an example, Figure 1.6 shows the phase-folded

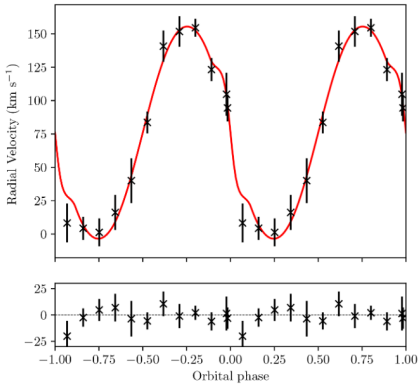

FIGURE 1.6— Phase-folded radial velocity curve of the hot component of the central star system of PN M 3−1. The upper panel shows the radial velocity data alongwith the corresponding curve of the best-fitting model. The lower panel shows the residuals between the model and the radial velocity data. Adapted from Jones et al. (2019).

radial velocity of the hot component of the CS system of PN M 3−1.

The main caveats of this method is that the period detection is limited to the resolution of the spectroscopic observations (i. e., to positively detect the RV variation a resolution higher than the amplitude of the variation is needed), and that no period were detected in most of the studied objects, so that RV variability could be the product of the wind variability (or pulsations of the CS) in several objects. Another limitation of this method is the needed of long-term monitoring to detect a binary CSPN.

1.3.4 UV-optical composite spectrum

Most of the methods to detect binary CSPN are based in optical or IR surveys, or in optical spectra long-term monitoring, looking for the cool component. Hot-WD in binaries in particular offer invaluable clues to stellar evolution. However, binaries with a hot-WD and a MS companion or giant companion, are extremely hard to identify unless UV data were available (the presence

of the very-hot, low-optical luminosity star being often indistinguishable from optical data). Most of the light emitted by a hot-WD is located toward the UV wavelength range. The *Galaxy Evolution Explorer* (GALEX; Martin et al., 2005) performed imaging surveys of the sky with a 1.2° field-of-view in two UV bands: the far-UV (FUV; 1344−1786 Å) and near-UV (NUV; 1771−2831 Å). GALEX UV catalog matched with optical surveys has been proven to be an important tool in the detection of hot-WD plus main-sequence companions (Bianchi et al., 2011a, 2018b), making the GALEX survey a unique database to search for binary CSPNe (e.g., Miszalski et al., 2012). The SED of a binary CSPN is composed by the emission of the ionizing star with $T_{\rm eff} > 30,000$ K, and the companion star with a cooler $T_{\rm eff}$. Figure 1.7 show a two component SED fitting of the unresolved GALEX plus SDSS photometry of the hot−WD system GALEXJ010853.7−005457, and is clearly seen the existence of the UV excess.

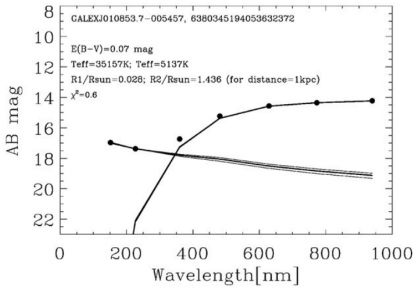

FIGURE 1.7— Two component of the SED fitting of the unresolved GALEX plus SDSS photometry of the WD GALEXJ010853.7−005457 (radius given for a reference distance of 1 kpc). Adapted from Bianchi et al. (2018b).

This thesis aims to take advantage of the GALEX survey to search for binary CSPNe, and characterize the ionizing star and the cool companion, after classifying the emission of the observed PNe (between point-like and extended, see Section 2.3 for more details). The main limitation of this method is related to the GALEX survey because most of the PNe that are located near the Galactic plane were not observed due to the GALEX safety limits (Bianchi et al., 2017). Another limitation is that the possibility to detect late-type stars

(e. g., M3V and later) is practically impossible as these stars are usually too faint compared with the emission of the CS in the optical region.

1.4 CSPNe model parameters

Up to this point we mentioned in Section 1.3.4 that the binary CSPNe is composed by a hot-WD and a cool companion, and that our main goal is to characterize the stellar parameters (mainly the $T_{\rm eff}$ of both stars) by using the UV and optical catalogs. To characterize the SED, it is necessary to describe it in terms of a synthetic model. In this thesis we are using the stellar atmosphere models for two kind of analysis: 1) to fit the SED observed by comparing with a synthetic SED computed with the stellar atmosphere model spectra (see Chapter 3 for details), and 2) to compute photoionization models to compare the observed colors of point-like PNe with the model colors that includes the stellar flux and the nebular emission (nebular continuum and emission lines; see Chapter 4).

For a precise SED analysis of hot stars, observations with good quality (high signal-to-noise and accurate photometry) and stellar-atmosphere models that account for solid physics and deviations from the assumptions of local thermodynamic equilibrium (LTE) are necessary. In the last century, non−LTE model atmospheres initially require high computational times and a lot of work on atomic data. Hence, the use of blackbody spectra to represent hot stars had been a standard approximation in practice where ionizing fluxes were required. Several well documented non-LTE codes have been developed: PHOENIX[1] (Hauschildt, 1999; Hauschildt & Baron, 2010), TLUSTY[2] (Hubeny, 1988), TMAP[3] (Werner et al., 2012), and CMFGEN[4] (see Herald et al., 2005). The first one is mostly being used for dwarf stars and earlier type stars (O- and B-type stars), whereas the latter two are widely used, for example, in spectral analysis of hot, compact stars.

The Figure 1.8 shows, as an illustrative example, the difference between a non-LTE TMAP model and a blackbody spectrum for a typical WD ($T_{\rm eff}$=110,000 K and $\log(g)$=7.0). It is clear that differences at longer wavelengths than 900 Å are of a few percents. However, it becomes very different at short ward wavelengths than 900 Å. This fact is very important, for example, in the modeling of a photoionized gas envelope by a hot compact star, because most of the ionizing photons have energies corresponding to wavelengths shorter than 1100 Å where

[1] https://www.hs.uni-hamburg.de/EN/For/ThA/phoenix
[2] http://nova.astro.umd.edu
[3] http://www.uni-tuebingen.de/de/41621
[4] http://kookaburra.phyast.pitt.edu/hillier/web/CMFGEN.htm

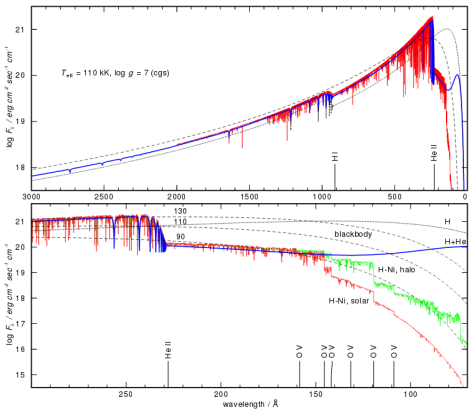

FIGURE 1.8— Top: comparison of non−LTE TMAP model atmosphere fluxes ($T_{\rm eff}$=110 kK, and $\log(g) = 7$) calculated with different chemical composition. Short-dashes: pure H model, thick line: H+He, thin line: H−Ni with $[Z]$=0. Note that the main deviations from blackbody (long dashes, 110 kK) of the synthetic spectra occur shortwards of H I and He II ground state thresholds. Lower panel: Detail of the upper panel; in addition, a H−Ni model with $[Z]$=−1 (thin line), and three blackbody fluxes (long dashes for $T_{\rm eff}$=90, 110, 130 kK) are shown. The prominent He II and OV absorption edges are indicated. Note the drastic decrease of the flux at short wavelengths, if the opacities of metals are considered. Taken from Rauch (2003).

a blackbody becomes unrealistic.

Our study of CSPNe photometry and SED modeling, make use of the grid of non-LTE atmosphere models of Bianchi et al. (2011a), computed with TLUSTY code, with an extended grid (but with much smaller parameters step) of stellar parameters ($T_{\rm eff}$ and $\log(g)$).

1.5 Photoionization models for compact PNe

A PN is assumed to be made up of two components: a CS and a surrounding gaseous envelope. As the CS is among one of the hottest stellar objects, most

of its energy is emitted in the UV. These UV photons will be able to ionize the atoms in the nebula. The electrons ejected in the ionization process (photoionization) provide a pool of kinetic energy for the collisional excitation of the heavy atoms (C, N, O, etc.). Then, spontaneous emission from the various excited states of the different atoms and ions (recombination) are responsible for the rich nebular emission seen in the UV and visible range. Then, unlike stars which show a continuous spectrum, the spectrum of PN is dominated by emission lines and nebular continuum (being stronger in the visible range). In compact PNe, the flux integrated over an aperture to obtain the observed magnitude at an specific wavelength is composed by the stellar plus nebular continuum and emission lines. In this way, isolate the CS flux is not an easy task. The best way to carry out with this problem is to model of PN that includes both; the stellar flux and nebular emission. This models are often called *photoionization models*.

Zanstra (1927) already suggested that the emission line spectrum of a nebula was caused by the radiation of high temperature star. Later on, Seaton (1959), calculated the recombination spectrum of the hydrogen atom, where the free electrons have a maxwellian velocity distribution, with equilibrium between heating and cooling. The emission lines and continuum radiative transfer have to be solved simultaneously in the photoionization models. Storey & Hummer (1995) calculated a detailed recombination cascade of H-like ions, for a wide range of temperatures and density values. First attempts to determine the chemical abundances of a gaseous nebula were based on models which included the collisionally excited emission lines and the ionizing photons from the central stars (e.g., Williams, 1967; Rubin, 1968; Harrington, 1969). More recent codes were developed by Binette et al. (1993), (who introduced dust in their code called MAPPINGS[5]), and more recently Sutherland et al. (2013), introduced shocks in the code. Ercolano et al. (2003) developed a three-dimensional Monte Carlo photoionization code called MOCASSIN[6]. However, nowdays the most complete photoionization code is CLOUDY[7] (Ferland et al., 1998). CLOUDY was available to the astronomy community, and improved over the years (to the last version see Ferland et al., 2017). One of the big problems with the photoionization codes is to choose the right atomic parameters, as it has been shown in several relevant reviews (e.g., Luridiana et al., 2011; Juan de Dios & Rodríguez, 2017). CLOUDY selects the best atomic parameters for each ion, which makes it the most reliable photoionization code until now.

[5] https://miocene.anu.edu.au/mappings/
[6] https://mocassin.nebulousresearch.org/
[7] https://nublado.org

Cloudy is a non-LTE spectral synthesis code and plasma simulation code designed to simulate astrophysical environments within clouds (e. g., PN, active galactic nuclei, and H II regions) and predict their emission line spectra. It has been used to infer the physical parameters by matching the models to observational spectra of compact PNe (e.g., van Hoof & van de Steene, 1999). Bohigas (2008) used observed emission lines to construct a photoionization model of thirteen PNe, obtaining satisfactory match.

In this thesis, a grid of Cloudy photoionization models is calculated, and both emission lines and broad band magnitudes are used to analyze the PNe that are unresolved or with a small diameter. This analysis is useful not only to model color magnitudes of unresolved PNe but also to investigate the nebular emission and emission lines that are affecting the observed magnitudes.

1.6 Thesis outline

This thesis aims to take advantage of GALEX, a satellite that imaged the sky in FUV and NUV broad bands simultaneously matched to optical surveys (Morrissey et al., 2007; Bianchi, 2009), to search for binary CSPNe. Studies of both the nebula and the CS benefit by observations in the UV bands, where crucial diagnostic atomic transitions of important chemical elements abound (e.g., Bianchi, et al. 2012, 2016). CSPNe emit mostly at the UV wavelengths or short-wards as these objects are among the hottest stars known. GALEX, when matched with optical bands, has been proven to be very useful in the detection and characterization of WD stars and WD plus a cool companion star (Bianchi, et al. 2007, 2009, 2011, 2018). The main difference between this method for searching binary CSPNe with respect to others is the sensitivity of the GALEX UV bands to the CSPN emission.

In Chapter 2, we start by constructing a catalog of PNe detected in the UV and optical bands. This work makes use of the GALEX pipeline data to characterize the detected PNe and classify them into resolved and unresolved sources. Then we isolated the CS flux from those resulting resolved PNe using aperture photometry techniques. The SED of the CS magnitudes is used in Chapter 3 to find binary CSPNe by a statistical method.

In Chapter 4, we construct a grid of model SEDs of PNe by using the Cloudy photoionization code to compare the emergent spectra of PNe. We use this model-grid to analyze the unresolved PNe that resulted from the analysis in Chapter 2 and classify them in color-color diagrams.

In Chapter 5, we analyze a unique case of a binary CSPN, NGC 2346, that has passed through a CE phase. We use UV and optical spectra to resolve a

significant discrepancy with the interstellar extinction, and to derive its stellar parameters.

2

Catalog of Planetary Nebulae detected by GALEX and optical corollary data

Nada de lo que sucede se olvida jamás
aunque tú no puedas recordarlo.
El viaje de Chihiro (2001)

Abstract– **We compiled a catalog of PNe (PNcat) by combining the coordinates from the Kerber, Stanghellini, and Wiedmann catalogs, and complemented by the HASH database, and matched the coordinates from the PNcat with the GALEX database (GPNcat). GALEX imaged the sky in the ultraviolet (UV) range in both far-UV (FUV; 1344−1786 Å) and near-UV (NUV; 1771−2831 Å), simultaneously, allowing us to extract the hottest stellar objects, which are elusive in optical wavelengths. We matched the GPNcat with SDSS and the PanSTARRS1 (PS1) databases (GPNcatxSDSSxPS1), both proportioning five magnitudes in the optical range (SDSS *ugriz* and PS1 *grizy*) in addition to FUV and NUV. We separated the resolved PNe, with sizes (diameters) at least twice the resolution of GALEX, from unresolved PNe. For resolved PNe, the flux of the CS were isolated by using aperture photometry techniques. Since both SDSS and PS1 only cover the northern hemisphere, leaving some southern GALEX sources out, 14 PNe located in the southern hemisphere were observed using the telescopes from Las Cumbres Observatory (LCO). The final catalog, `GPNcatxSDSSxPS1`, contains 392 PNe with both UV and optical photometry of which 269 are resolved.**

2.1 Introduction

SEVERAL models have been proposed to explain the morphologies observed in PNe. Central star (CS) binarity is now thought to be critical for understanding the formation and evolution of bipolar PNe, which are a large fraction of PNe (∼17% in a sample of 225 PNe; Manchado, 2004). Binaries may play an important role in stellar evolution. Out of more than 2000 PNe known, only 40 binary CSPN are currently known (Jones & Boffin, 2017a). Most of them have been discovered through photometric variability, which favors the detection of periods shorter than 3 days, as seen in Figure 1 of De Marco et al. (2008) (see Chapter 1).

In this chapter we examine a sample of PNe within the footprint of the *Galaxy Evolution Explorer* (GALEX; Martin et al., 2005) matched to *Sloan Digital Sky Survey* (SDSS; York et al., 2000) and *Panoramic Survey Telescope and Rapid Response System* (PanSTARRS; Chambers et al., 2016) sky surveys. We extract the photometry of the CS in all UV-optical bands; the ionizing stars have effective temperature higher than 30 000 K, being more sensitive in UV-bands, whereas the cool companion is more sensitive in optical bands. The broad band coverage, from UV to optical range, will reveal if a cooler companion exist.

In Section 2.2 we explain how we choose the sample of Galactic PNe, and how the GALEX, SDSS, and PanSTARRS matches were made. We then separate resolved PNe those with sizes (diameters) at least twice the resolution of GALEX of 4.2/5.″3 in FUV/NUV, from unresolved PNe, and isolate the CS flux from the nebular emission.

2.2 Constructing a UV-optical photometric catalog of PNe

2.2.1 Assembling the PN sample for our study: PNcat

We assembled an extensive list of known PNe, that we will refer to as PNcat, by combining several compilations of confirmed or candidate PN as follows. We used coordinates from the catalog of *Coordinates of Galactic Planetary Nebulae*[1] (CGPNe; Kerber et al., 2003). The catalog compiled the position of 1312 PNe. Of these, the position of 1086 PNe with visible CS (a CS that is recognizable, clearly resolved from the nebular body) or with small diameter

[1]The catalog on Vizier: `http://vizier.u-strasbg.fr/viz-bin/VizieR-3?-source=J/A%2BA/408/1029`

(point-like sources) listed in the Strasbourg ESO catalog (Acker et al., 1992a), its supplement (Acker et al., 1996), and the 2000 version of the catalog of PNe (Kohoutek, 2001), were combined using the 2nd generation Guide Catalog (GSC-II. Cat.), with an absolute position accuracy of $\sim 0\farcs35$. For the another 226 extended PNe in CGPNe, with unresolved CS, the positions were compiled based on the second epoch of the *Digital Sky Survey* (DSS-II) with a reported accuracy of $\sim 5\ ''$.

We also included the catalog by Stanghellini & Haywood (2010), and *CSPNe: New spectral classification catalog* (Weidmann & Gamen, 2011) which include 25 additional PNe not included in the CGPNe. In addition, we also included all the PNe presented in *The Hong Kong/AAO/Strasbourg H_α catalog of PNe* (HASH; Parker et al., 2016), which includes, new PN candidates from H_α surveys and amateur astronomers. The HASH catalog includes objects with "status" such as: T for True PN, L for Likely PN, and P for probably PN, with a reported positional accuracy between $1-10\ ''$. We included all the PNe to further analyze also those that are classified as L or P using UV and optical data. A total of 3687 PNe are included in our compilation (hereafter PNcat).

PNcat includes information related to the PNe sizes as extracted from HASH database (`MajDiam` and `MinDiam` for maximum and minimum diameter, respectively). Information about the spectral type of the central star (`SpT`), extracted from Weidmann & Gamen (2011) catalog, is also included. The final catalog, with a mean positional accuracy of $\sim 5\ ''$, is available in `http://research.iac.es/proyecto/PNeGrid`.

2.2.2 Matching PNcat with the GALEX database: GPNcat

The *Galaxy Evolution Explorer* (GALEX) imaged the sky in the far-UV (FUV, 1344–1786 Å, $\lambda_{\rm eff} = 1538.6$ Å) and near-UV (NUV, 1771–2831 Å, $\lambda_{\rm eff} = 2315.7$ Å) simultaneously, with a field-of-view of 1.2° diameter and a spatial resolution of $4\farcs2$ and $5\farcs3$, respectively (Morrissey et al., 2007). The images, reconstructed from photon counting detector recordings, are sampled with virtual pixels of $1\farcs5$ size (see Bianchi, 2009). The widest sky coverage is provided by the All-Sky Imaging Survey (AIS) and the Medium (depth) Imaging Survey (MIS), that reach typical depths of 19.9/20.8 mag (FUV/NUV) and 22.6/22.7 mag (FUV/NUV), respectively, in the AB magnitude system (see Bianchi, 2009; Bianchi et al., 2011a; Bianchi, 2014; Bianchi et al., 2017, for a review and for sky coverage).

In this work, we used data from the GALEX sixth and seventh releases (GR6/GR7) with sky coverage of 24 790 $\deg^2$ and 2251 $\deg^2$ for AIS and MIS, respectively (Bianchi et al., 2017, 2019). The data were extracted from the

Space Telescope Science Institute (STScI) *Mikulski Archive for Space Telescope* (MAST[2]), at the CASJobs SQL interface[3]. Our PNcat was matched to GALEX `visitphotoobjall` table with a match radius of 5″. This radius was chosen to include objects with positional error <= 5 ″, similar to the measured positional errors in PNcat.

The GALEX archive contains multiple observations of the same object when fields overlap or were repeated. We kept existing duplicate measurements to check for flux variation. This is also useful for objects that were observed in FUV and NUV at different epochs if one of the detectors (most often FUV) was not exposed. The GALEX database also contains information related to the *artifacts* on the images. According to the GALEX GR6[4] documentation, the only artifact flags causing real concern are *Dichroic reflection* (*artifact*=4 or 64) and *Window reflection* (NUV only; *artifact*=2). It is also recommended to remove objects that are near the edge of the field-of-view as these sources could have *edge reflection* or the *rim artifact* (*artifact*=32) set (Bianchi et al., 2011a; Bianchi, 2014; Bianchi et al., 2017). This could be done by removing the sources with `fov_radius` $> 0.55°$.

Out of the 3687 PNe listed in PNcat, 1401 measurements of 625 unique PN were found in the GALEX UV imaging surveys (GPNcat); 333 of the 625 have multiple measurements in the GALEX database. The distribution in magnitude and FUV−NUV color of objects (including multiple measurements) are shown in Figure 2.1. The magnitudes correspond to the best fit of each source shape as determined by the pipeline. Vertical dashed lines correspond to the non-linearity limit for FUV and NUV (13.73 and 13.85 ABmag, respectively; see Bianchi & Thilker, 2018, for details on non-linearity limits). About 622 of PNe have NUV measurements but only 213 PNe have both FUV and NUV measurements.

2.2.3 Matching PNcat to SDSS

The *Sloan Digital Sky Survey* (SDSS) Legacy Survey project (York et al., 2000) has mapped the sky in five broad bands using a dedicated 2.5 m telescope located at the Apache Point Observatory (APO) in New Mexico. The telescope used a wide-field of view camera to acquire the images and a 0.5 m telescope was used for photometric calibration. The SDSS covers the range from 3040 Å to 10833 Å, with five pass bands: u (3048–4028 Å, $\lambda_{\rm eff}$ = 3594.9 Å), g (3783–5549 Å, $\lambda_{\rm eff}$ = 4640.4 Å), r (5415–6989 Å, $\lambda_{\rm eff}$ = 6122.3 Å), i (6689–8389 Å,

[2] `http://archive.stsci.edu/`
[3] `http://galex.stsci.edu/casjobs/`
[4] `http://galex.stsci.edu/GR6/?page=ddfaq#6`

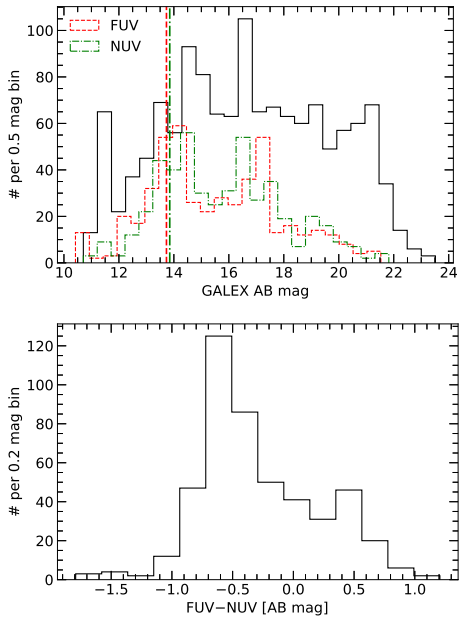

FIGURE 2.1— Distribution of GALEX magnitudes (top) and FUV−NUV color (bottom) for the PNe found in the GALEX UV surveys. A total of 622 PNe have NUV measurements (black histogram in the left panel) but only 213 PNe have both FUV and NUV measurements (blue and orange histograms, respectively). The vertical lines mark the flux saturation limit of each band.

TABLE 2.1— PNe from GPNcat matched to SDSS DR14.

PNG	RAJ2000	DEJ2000	Matches$_{GALEX}$ (gmSize)	Matches$_{SDSS}$ (smSize)
003.3+66.1	14:16:22	+13:52:24	4	3
009.6+14.8	17:14:04	−12:54:38	2	4
011.1+11.5	17:28:34	−13:26:21	2	1
013.3+32.7	16:21:04	−00:16:11	3	11
026.0+46.6	15:50:55	+14:59:33	2	9

Note: The number of matches found in GALEX and SDSS catalogs for a given PN. A total of 62 PNe have GALEX and SDSS measurements. (This table is available in its entirely in machine-readable form.)

$\lambda_{\rm eff}$ = 7439.5 Å) and z (7960–10 830 Å, $\lambda_{\rm eff}$ = 8897.1 Å), with a spatial resolution of $\sim 1''.4$.

In this work, we used the SDSS data release 14 (DR14; Abolfathi et al., 2018) covering a unique footprint of 14 724 deg^2 of sky (from AREAcat[5]; Bianchi et al., 2019). The data were extracted from the STScI MAST database, at the CASJobs SQL interface[6]. Sources were extracted from the `photoobjall` table with a match radius of $5''$ and removing objects with "edge" flag set[7]. We only kept objects with `mode`$\leq$`3` set which includes "primary", "secondary" (re-observations), and "family" (blended or de-blended sources) objects. Note that all objects with `mode=3` set should be treated carefully as may include objects wrongfully deblended.

Out of the 3687 PNe listed in PNcat, only 472 measurements of 139 unique PN were found in the SDSS DR14 database; 93 of the 139 have multiple measurements in SDSS. Only 62 PNe from GPNcat have a match in SDSS DR14, 41 of which with multiple measurements.

2.2.4 Matching PNcat to PanSTARRS

The *Panoramic Survey Telescope and Rapid Response System* (PanSTARRS; Chambers et al., 2016) is a system for wide-field camera astronomical imaging in northern hemisphere (Dec. $> -30°$). PanSTARRS1, PS1, is the first part of PanSTARRS to be completed and is the basis for the current data releases; DR1 (3π survey) and DR2 (Medium Deep survey; hereafter MDS). The PS1 survey

[5] `http://dolomiti.pha.jhu.edu/uvsky/area/AREAcat.php`
[6] `https://skyserver.sdss.org/casjobs/`
[7] `https://www.sdss.org/dr16/algorithms/photo_flags_recommend/`

used a 1.8 meter ground-based telescope, located at Haleakala Observatory in Hawaii, and its 1.4 Gigapixel camera to image the sky in g (3943–5593, $\lambda_{\rm eff}$ =4775.6), r (5386–7036, $\lambda_{\rm eff}$ =6129.5), i (6778–8304, $\lambda_{\rm eff}$ =7484.6), z (8028–9346, $\lambda_{\rm eff}$ =8657.8), and y (9100–10838, $\lambda_{\rm eff}$ =9603.1), with a field-of-view of 3 ° and a single epoch depth ($5\,\sigma$) of 22.0, 21.8, 21.5, 20.9, and 19.7 mag, respectively.

We matched the PNcat and GPNcat with PS1 MDS using the CasJobs interface at MAST[8] with a match radius of 5 ″. Sources were extracted from the `MeanObjectView` joined to `StackObjectAttributes` tables.

Table 13 of Chambers et al. (2016) lists flags relative to the quality of the extracted photometry contained in the `MeanObjectView` table. We restricted our results to sources with `objInfoFlag` containing the "GOOD" flag (Good quality measurement in our data (e.g., PS)) and sources which have mean magnitudes in $g\ r\ i\ z$ (i.e., at least 3 detection in each band that can be used for the mean mag; `nDetections`≥ 3).

There was an un-reported problem with the CasJobs interface on February 2017 using the PS1 3π survey. Our query resulted in containing objects with greater distance than the search radius required. These extra objects were removed from the CasJobs output table with a Python script written by us. This error was solved with the version 2, the one that we finally used in this work.

The `MeanObjectView` table contains the mean photometry for objects based on single epoch data. We match the PNcat and GPNcat using a match radius of 5 ″. In most cases, the closest source corresponds to the object of interest but as can be seen in Figure 2.2 this is not always true. We visually inspected all sources with multiple matches using the interactive sky atlas Aladin (Bonnarel et al., 2000) in conjunction with the *Tool for Operations on Catalogues And Tables* (TOPCAT; Taylor, 2005), to keep track the multiple matches and add them to the final table. To obtain the multiple-epoch photometry of each match, we cross correlated the `objID` from the `MeanObjView` with the `Detection` table, which contains single epoch photometry of individual detections from a single exposure.

Of 3687 PNe in PNcat, 6557 measurements of 2171 unique PN are included in PS1 MDS `MeanObjectView` table. Of the 2171 PNe, 1662 have multiple matches in PS1 MDS. Only 389 PNe from GPNcat have a match in PS1 MDS, 121 of which with multiple matches.

[8] `https://panstarrs.stsci.edu`

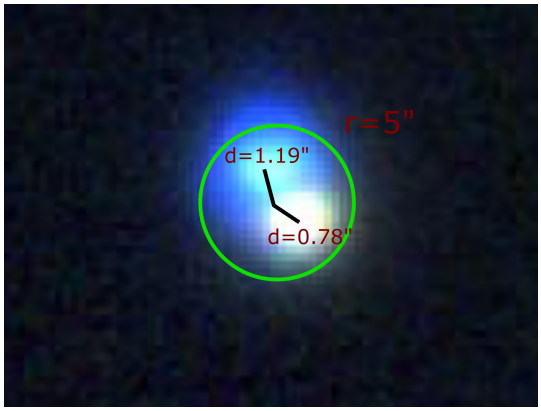

FIGURE 2.2— Example of PN A 33 in i_{PS1} (red), r_{PS1} (green), and g_{PS1} (blue). The source at the center-down is the closest match to the reference coordinates, whereas the source at the center-top is the second match.

2.2.5 Multiple matches

As mentioned in Section 2.2.2, GALEX archive contains multiple observations of the same source when some fields overlap or were repeated, and having all measurements is useful for variability studies. For our present purpose we constructed a catalog containing multiple measurements of the same source. This include both repeated measurements and field stars.

To facilitate the analysis we created tags, similar to those in Bianchi et al. (2011a,b) and Bianchi & Shiao (2020), by which repeated measurements and probable field stars could be identified. We defined the tag `PNRank` to classify the type of the match being =0 if is the only match to this PN, =1 if is the closest of more than one match to this PN (hereafter primary), =2 if it is considered possible duplicated, and =3 if it is considered probable field star. We also added the `GrpRank` tag to keep track the number of members of each classification when `PNRank`>1, ranked in order of distance from the PN.

For a given GALEX source, `gPNRank`=0 implies that the PN only have

TABLE 2.2— PNe from GPNcat matched to PS1 MDS.

PNG	RAJ2000	DEJ2000	Matches$_{GALEX}$ (gmSize)	Matches$_{PS1}$ (pmSize)
000.1−01.7	17:52:49	−29:41:59	2	3
000.1−02.3	17:55:21	−29:57:36	1	2
000.2−01.9	17:53:46	−29:43:46	1	6
000.5−01.6	17:53:25	−29:17:09	2	6
000.7+03.2	17:34:55	−26:35:57	1	1

Note: The number of matches found in GALEX and PS1 catalogs for a given PN. A total of 388 PNe have GALEX and PS1 measurements. (This table is available in its enterely in machine-readable form.)

one measurement. If within the match radius, of 2.″5, around the closest source to the PN we find other sources, from different observation (with different `photoExtractID`), we assign `gPNRank`=1 to the best measurement of this group (primary); the best measurement is the one with the longest exposure (`galex_exptime`) or –for equal exposure– the closest to the field center (`fov_radius`). GALEX sources were considered possible duplicated if they lied within 2.″5 from the primary but from different observation (`gPNRank=2` and `gGrpRank=x` with x the number of members within this group). If the GALEX sources are within 2.″5 but from the same observation as the primary, they were considered possible field stars (`gPNRank=3`). For any other condition is given `gPNRank=4`. The choice of a 2.″5 match radius to the primary is based on the consideration that the deblending of sources closer than this separation is not always robust due to the instrumentation resolution (∼4.2/5.″3, FUV/NUV; see Bianchi et al., 2007, 2011a, 2017).

A given PN in our PNcat may have also multiple SDSS and PS1 MDS matches within the search radius (5 ″), given the higher spatial resolution of SDSS and PS1 (∼1.″4 and 1.″2, respectively). Particularly, in the case of SDSS sources, we follow the same procedure as with GALEX sources. We "ranked" the multiple SDSS matches based on the distance to the PN. The closest SDSS match is retained as the primary measurement for the PN and is ranked with `sPNRank=1` and `sGrpRank=1`. If the SDSS sources are within 1.″4 from the primary but with `mode=2` (re-observation) is marked as repeated measurement and is given `sPNRank=2` and `sGrpRank=x`. In any other case is given `sPNRank=3`. In the case of PS1 MDS, we ranked only by distance, being the closest PS1 match marked as the primary measurement for the PN (`pPNRank=1` and `pGrpRank=1`) as the `MeanObjView` table only contains unique objects. Multiple matches were

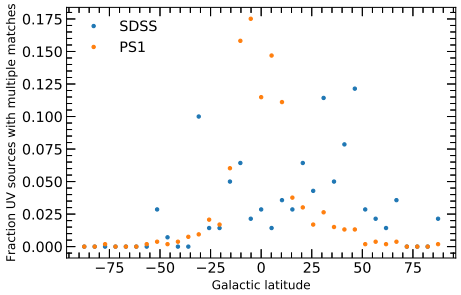

FIGURE 2.3— Fraction of UV sources having multiple optical matches within a 5 ″ match radius, as a function of Galactic latitude. The data is binned every 5 °. Blue dots are SDSS matches and orange dots are PS1 matches.

also noted and ordered by distance (`pPNRank=3` and `pGrpRank=x`). Repeated PS1 MDS measurements for each match were acquired from the `Detection` table and included in a different table (see Section 2.2.5).

Note that, in all cases, we retained all the multiple matches resulted for each PN in our PNcat, because, even though the closest optical source may be the actual GALEX counterpart, at GALEX resolution(∼4.3/5.″2 in FUV/NUV), the photometry may be a composite measure of two or more optical sources (see Figure 2.2).

Figure 2.3 shows the fraction of UV sources having multiple optical matches within a 5 ″ match radius as a function of Galactic latitude. The number of multiple optical matches increases toward the Galactic center as expected. The scatter of SDSS over the Galactic latitudes is related to the inclusion of re-observations and family sources. However, the fraction increases up to 17.5% and 7.5% in PS1 and SDSS, respectively, for latitudes $|b| < 15$ ° because of the higher density of stars in the disc of the Milky Way. The fraction was calculated dividing the sum of the number of matches per each PN per 5 ° bin in Galactic latitude by the total number of PS1 or SDSS matches.

2.3 Analysis of the PNe detected by GALEX

In this section we will investigate the effect of the nebular emission in the CSPNe photometry from our `GPNcatxSDSSDR14xPS1`. A separation between resolved and unresolved PNe, taking into account the GALEX resolution, will me made. For those resolved PNe we will isolate the CS flux from the nebular emission by applying aperture photometry techniques.

2.3.1 Effect of Nebular emission in CSPNe photometry

We must assess the consistence and accuracy of the GALEX, SDSS, and PS1 photometry for our sample. In general, the measurements may contain flux from both CS continuum and PN nebular emission (lines and continuum). To isolate the CS photometry, an analysis of the nebular emission has been made.

Figure 2.4 shows the optical PN spectrum of NGC 1501[9], with the transmission curves of SDSS u, g, r, and i (top), and PS1 g, r, i,z, y (middle). Figure 2.4 bottom also shows the IUE SWP28952 and LWP08948 UV spectra with the transmission curves of GALEX FUV and NUV overlaid. In the optical range, an [O III] emission line is prominent in g band, and H_α and [N II] emission lines in r band. In the UV range, C IV and He II emission lines in FUV, and He II and [Ar IV] lines in NUV.

Nebular emission complicates measurements of the CS flux, particularly for those PNe that have bright central emission and compact PNe. For extended PNe (compared with the instrumental PSF), we measured the CSPN flux with an aperture of the size of the instrumental PSF and corrected for the nebular contribution estimated in an annulus (of the size of the extended emission) to extract the PN emission plus local background flux. The accuracy of the correction depends on the radial profiles of the flux in the lines contributing to each filter. In particular, if the correction is small with respect to the CS flux the estimated error will be small. E.g., Bianchi & Thilker (2018) show seven PNe radial profiles from GALEX and in some of them the nebular emission is several orders of magnitudes fainter than the CS flux. However, for hot CSPNe ($T_{\rm eff}$>45 000 K), the extracted CS flux could be affected by the PN contribution to the He II λ1640 emission line, stronger in the inner parts of the PNe, close to the CS.

[9]Taken from the Gallery of PNe spectra: `https://web.williams.edu/Astronomy/research/PN/nebulae/`

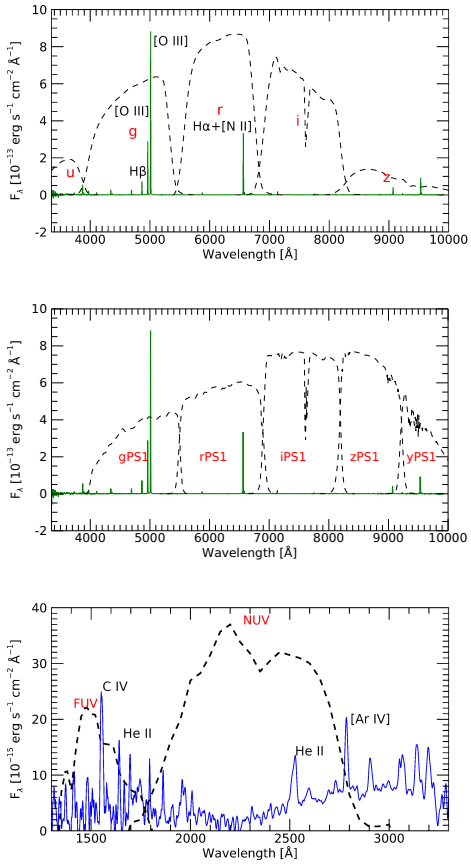

FIGURE 2.4— Optical (top and middle) and UV (bottom) spectra of the PN NGC 1501. The SDSS (top), PS1 (middle), and GALEX (bottom) transmission curves are shown overlaid.

2.3.2 PNe resolved by GALEX

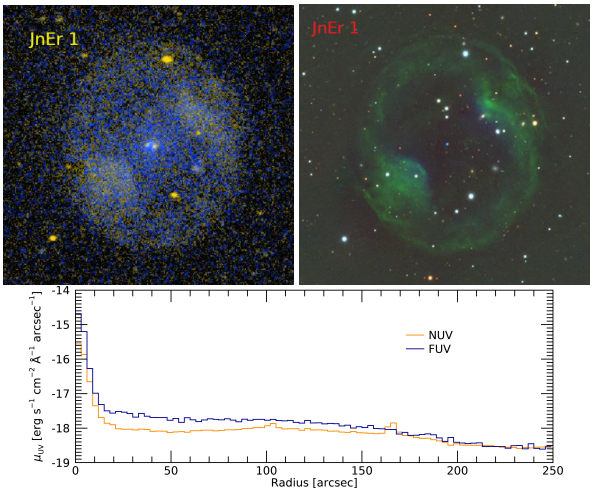

FIGURE 2.5— Example of extended (∼120″) and resolved PN JnEr 1 observed by GALEX (left, Bianchi et al., 2017) in FUV (blue) and NUV (yellow), and by PS1 (right) in g (blue), r (green), and y (red). In GALEX imaging, the CS appears very bright and resolved but the "best" measurement will include most of the nebular emission and, in PS1 it will be measured as a point-like. A radial profile for the two GALEX bands (bottom) is also shown. North is up and East is left.

The size and the morphology of a PN depends on the ionization structure, the projection effect, and the sensitivity of the instrument/depth of the exposure. A number of observational surveys have measured the sizes of PNe at different wavelengths (e.g., Acker et al., 1992b; Stanghellini & Haywood, 2010; Frew et al., 2013). We used the size measurements reported in Stanghellini & Haywood (2010) catalog and those compiled in the HASH database to separate the resolved PNe from point-like PNe and include them in the PNcat. As a first approximation we assume a PN as resolved in GALEX imaging if the size

reported is at least twice the resolution of GALEX in NUV band (5.″2). A total of 375 resolved PNe were found (PNe with diameter >10″). However, as all sizes were measured in the optical range it is necessary to investigate resolved PNe using the GALEX images and compare them with those resolved in optical bands.

GALEX database provides different measurements of the flux for each source, such as Kron-like elliptical aperture (`MAG_AUTO`), isophotal (`MAG_ISO`), and circular apertures (`MAG_APER`). The "best" measurement (`fuv_mag` and `nuv_mag`) corresponds to the best fit of the source shape as determined by the pipeline. Problems can occur when the nebula is large enough to appear non-stellar. Due to the resolution of GALEX, of 4.3/5.″2, the "best" measurement may contain the flux of the entire PNe. Figure 2.5 shows the extended PN G164.8+31.1 (JnEr 1) and its radial profile as an example.

In order to separate the flux of the CS from that of the PNe in GALEX, we compared the magnitudes measured in different apertures provided by the pipeline: `FUV_MAG_APER_X` and `NUV_MAG_APER_X`, with X=1–7 (see Table 2.3 for radius sizes). Aperture corrections are described in the Figure 4 of Morrissey et al. (2007) and discussed in de la Vega & Bianchi (2018, see their Figure 3). Figure 2.6 shows the curve-of-growth of the `MAG_APER_4` compared with the larger apertures. For a point-like object, it is expected that the difference between the aperture magnitude (after aperture correction) compared with a fixed aperture should be nearly zero. All objects with `MAG_APER_4`−`MAG_APER`> 0 were cataloged as resolved. We used `MAG_APER_4` to separate the resolved objects (Fig. 2.6, bottom) as this aperture is twice the resolution of GALEX and, by comparing known PN diameters from previous catalogs (Figure 2.6) , the difference `NUV_MAG_APER_4`−`NUV_MAG_APER_5`>0 is a good indicator of resolved PN. The distribution in magnitude of resolved and unresolved PNe by GALEX (selecting only unique and primary measurements, `gPNRank`=0 and 1, respectively) is shown in Figure 2.7. A total of 417 resolved measurements were found (and given `galexClass=1`).

We found 54 and 289 of the resolved PNe from GPNcat in SDSS and PS1 catalogs, respectively. Also, we classify the resolved objects found in SDSS and PS1 (`sdssClass=1` and `ps1Class=1`, respectively). SDSS classified extended objects based on the difference of `psfMag`−`cmodelMag`>0.145. In the case of PS1, we identified extended PNe as described by Farrow et al. (2014), with `MeanPSFMag`−`MeanKronMag`>0.05.

Some PNe that are not classified as a resolved PN in both UV and optical bands, are not necessarily compact PNe. This may be PNe with an extended envelope and low surface brightness that is not significantly contributing to the flux. On the contrary, optically extended PNe, with sizes $\lesssim 5$ ″, may be

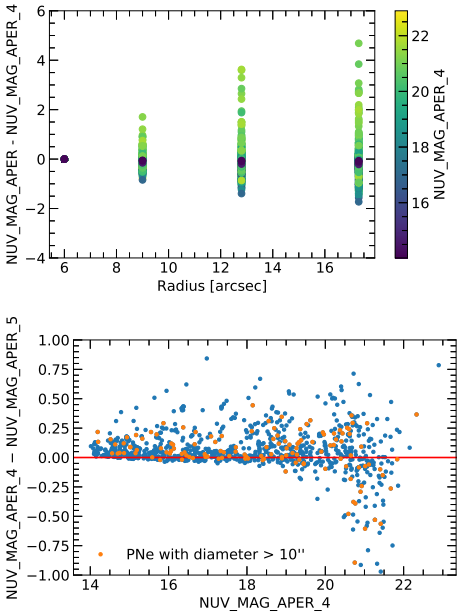

FIGURE 2.6— Curve-of-growth of GALEX NUV NUV_MAG_APER_4 compared with magnitudes measured in larger GALEX apertures (top; applying the different aperture correction to each aperture described in Table 2.3). Values above zero (red solid line) indicate that the object is resolved and values below zero indicates that the object is unresolved and may include the CS and PN line emission (also, bright objects present more negative values as indicated in the colorbar). We used NUV_MAG_APER_4 to separate resolved objects from unresolved objects (bottom).

TABLE 2.3— Aperture correction for the different apertures provided by the GALEX pipeline as determined by Morrissey et al. (2007).

Aper No.	radius	FUV_{corr}	NUV_{corr}
	(″)	(AB magnitude)	
APER_1	1.5	1.65	2.09
APER_2	2.3	0.96	1.33
APER_3	3.8	0.36	0.59
APER_4	6.0	0.15	0.23
APER_5	9.0	0.10	0.13
APER_6	12.8	0.09	0.09
APER_7	17.3	0.07	0.07

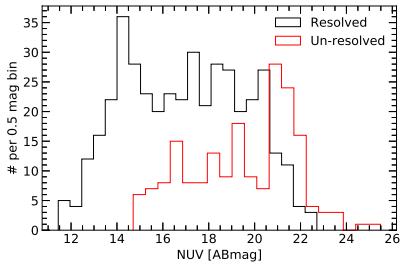

FIGURE 2.7— Distribution of GALEX magnitudes for resolved and unresolved PNe. A total of 417 resolved PNe were found.

unresolved in GALEX.

2.3.3 CSPNe photometry

Here we describe how we separated the emission of the CS from the nebular emission in the GALEX FUV/NUV and the optical SDSS and PanSTARRS images. We have selected only PNe with the flag "Resolved" in the `galexClass` tag (see Table 2.8) and with `gPNRank=0` or 1, to be consistent with extended objects in both UV and optical bands. We also selected PNe with GALEX FUV/NUV measurements with errors less than 0.1 mag to avoid bad photometry measurements.

To extract the CS photometry, an analysis of the 2D images from GALEX, SDSS, and PanSTARRS, was made. The CS photometry was calculated in three steps.

- We downloaded the 2D images from GALEX (`https://galex.stsci.edu/GalexView/`), SDSS (`https://dr12.sdss.org/fields`), and PS1 (`https://ps1images.stsci.edu/cgi-bin/ps1cutouts`), for each PNe field. SExtractor (Bertin & Arnouts, 1996) was used to find the brightest unsaturated objects on each downloaded field and to perform multiple aperture photometry. In the case of GALEX images, we used the equations to transform count rates to AB magnitude as described by Morrissey et al. (2007), with

$$m_{\rm FUV} = -2.5\log(f_{\rm FUV}) + 18.82, \tag{2.1}$$

$$m_{\rm NUV} = -2.5\log(f_{\rm NUV}) + 20.08, \tag{2.2}$$

  whereas for SDSS we used the transformation equations described in Stoughton et al. (2002)

$$m_{\rm SDSS} = -2.5\log(f_{\rm SDSS}) + 25.5, \tag{2.3}$$

  and for PS1, as we used the cutout images and they have already been converted to standard linear flux scale[10], we used

$$m_{\rm PS1} = -2.5\log(f_{\rm PS1}/{\rm exptime}) + 25.0, \tag{2.4}$$

  where f is the flux integrated on each aperture (see Table 2.4). The multiple aperture photometry was applied only to stars (i.e., where `CLASS_STAR`> 0.9 according to SExtractor output catalog).

[10] Visit: `https://outerspace.stsci.edu/display/PANSTARRS/PS1+Image+Cutout+Service`, for more information related to flux conversions.

- For each downloaded field we calculated the aperture correction employing a curve-of-growth analysis for each bright star in the field, using the previously derived multiple aperture photometry. We used the median value of the aperture correction derived for all stars as our final value. Errors were estimated according to the dispersion on each field's aperture correction.

- Individual aperture photometry was performed on each CSPNe from our catalog. The coordinates from the `GPNcatxSDSSDR14xPS1` were used to find the CSPNe and then the centroid positions were re-calculated to center the apertures (`rRA` and `rDEC`). We corrected from the nebular contribution estimated in an annulus to extract the PN emission plus local background flux. Aperture was set to fixed radius of 6 ″ to match the `APER_MAG_4` in GALEX (Table 2.4), and then the integrated count rates were converted to the AB magnitude system according to equations 2.1–2.4, applying the corresponding aperture correction (AC),

$$m_{\rm AB} = m_{\rm X} - AC \tag{2.5}$$

where X corresponds to FUV, NUV, SDSS, or PS1. Errors were estimated as

$$\sigma^2 = \sigma_{AC}^2 + \sigma_m^2. \tag{2.6}$$

Resulting CSPNe fluxes, for a total of 4 and 33 resolved PNe extracted from the `GPNcatSDSSDR14xPS1DR2` catalog, are presented in Tables 2.5 and 2.6 along with their diameters, MajDiam, and the separation between the PNe coordinates (from the original catalog; RA and DEC top) and the revised coordinates (RA and DEC bottom).

TABLE 2.4— Aperture radii used to measure the aperture correction of each field.

Aperture (No.)	GALEX	SDSS (″)	PS1
1	1.5	0.396	0.258
2	2.3	0.594	0.387
3	3.8	1.000	0.645
4	6.0	1.584	1.032
5	9.0	1.980	1.290
6	12.8	2.970	1.935
7	17.3	3.564	2.322

TABLE 2.5— The CS measurements for the SDSS objects from GPNcatxSDSSDR14xPS1 revised positions.

PNG	RA DEC	MajDiam (arcsec)	Sep. (arcsec)	FUV	NUV	u	g	r	i	z
						(AB magnitude)				
219.1+31.2	08:54:13 +08:53:53	970	0.37	13.436	14.069	14.759	15.192	15.749	16.087	16.355
	08:54:13 +08:53:53		0.07	0.100	0.001	0.019	0.053	0.004	0.008	0.014
144.3−15.5	02:45:24 +42:33:05	20	1.21	17.850	18.606	19.397	19.979	20.279	19.927	19.972
	02:45:24 +42:33:04		0.45	0.022	0.043	0.023	0.059	0.047	0.037	0.116
003.3+66.1	14:16:22 +13:52:24	50	0.19	16.117	16.791	17.717	18.189	18.671	18.859	18.976
	14:16:22 +13:52:23		0.23	0.100	0.022	0.008	0.005	0.007	0.013	0.072
211.4+18.4	07:55:11 +09:33:09	105	0.58	15.571	16.136	17.063	17.543	18.119	18.514	18.848
	07:55:11 +09:33:09		0.04	0.100	0.002	0.006	0.028	0.010	0.101	0.059

Notes: RA and DEC are the positions from the `PNcat` (top) and from the revised positions from `GPNcatxSDSSDR14xPS1DR2` (bottom). Sep. indicates the separation between `PNcat` and GALEX coordinates (top) and `PNcat` and SDSS coordinates (bottom).

TABLE 2.6— The CS measurements for the PS1 MDS objects from GPNcatxSDSSDR14xPS1 revised positions.

PNG	RA DEC	MajDiam (arcsec)	Sep. (arcsec)	FUV	NUV	g	r	i	z	y
						(AB magnitude)				
003.3+66.1	14:16:22 +13:52:24	50	0.88	16.117	16.790	18.246	18.668	18.911	19.075	19.209
	14:16:22 +13:52:23		0.31	0.100	0.021	0.014	0.006	0.006	0.015	0.024
017.3−21.9	19:46:34 −23:08:13	152	3.02	14.552	15.132	15.195	15.149	15.173	15.972	15.479
	19:46:34 −23:08:16		0.23	0.001	0.001	0.049	0.042	0.037	0.034	0.040
019.8−23.7	19:57:32 −21:36:45	312	0.27	16.879	17.508	18.006	18.282	18.537	18.752	18.856
	19:57:32 −21:36:45		1.22	0.037	0.029	0.004	0.004	0.004	0.007	0.032
025.0-11.6	19:19:18 −12:14:37	94	2.46	16.885	17.628	18.379	18.751	18.894	19.069	19.272
	19:19:18 −12:14:37		4.21	0.100	0.006	0.023	0.042	0.026	0.037	0.051

Continued on next page

Table 2.6 – continued from previous page

PNG	RA DEC	MajDiam (arcsec)	Sep. (arcsec)	FUV	NUV	g	r	i	z	y
				(AB magnitude)						
028.0+10.2	18:06:01 +00:22:39	50	0.48	16.941	17.538	17.398	17.535	17.716	17.841	17.981
	18:06:01 +00:22:39		0.08	0.100	0.140	0.096	0.071	0.065	0.055	0.066
033.0−05.3	19:10:26 −02:20:23	57	1.06	19.756	20.257	19.932	19.850	19.867	19.933	20.209
	19:10:26 −02:20:24		0.74	0.062	0.060	0.022	0.077	0.036	0.066	0.086
034.1−10.5	19:31:07 −03:42:32	86	0.21	16.411	17.255	16.852	16.850	16.909	16.977	17.151
	19:31:07 −03:42:31		0.92	0.011	0.003	0.022	0.024	0.027	0.031	0.045
038.1−25.4	20:31:33 −07:05:18	45	0.82	17.860	18.834	18.173	17.584	17.332	17.226	17.135
	20:31:33 −07:05:17		0.35	0.048	0.054	0.010	0.034	0.039	0.034	0.043
042.5−14.5	20:00:39 +01:43:40	28	0.44	16.017	16.870	17.834	18.362	18.426	18.564	18.657
	20:00:39 +01:43:40		0.80	0.047	0.045	0.022	0.046	0.041	0.089	0.089
043.5−13.4	19:58:27 +03:03:00	74	1.42	18.007	18.644	19.369	19.719	20.094	20.292	21.246
	19:58:27 +03:03:01		0.50	0.081	0.065	0.025	0.023	0.023	0.042	0.245
047.0+42.4	16:27:34 +27:54:33	162	0.74	13.880	14.656	15.401	15.825	16.224	16.493	16.700
	16:27:34 +27:54:33		0.31	0.014	0.023	0.027	0.011	0.013	0.013	0.011
050.4+05.2	19:04:32 +17:57:07	37	0.15	17.428	18.110	17.760	17.842	17.967	18.057	18.182
	19:04:32 +17:57:07		0.53	0.100	0.067	0.027	0.020	0.029	0.031	0.038
051.5+06.1	19:03:37 +19:21:23	56	2.04	19.038	19.711	18.390	17.975	17.684	17.481	17.374
	19:03:37 +19:21:25		0.46	0.034	0.046	0.018	0.024	0.038	0.040	0.033
059.7−18.7	20:50:02 +13:33:30	154	0.53	14.083	14.868	15.838	16.294	16.655	16.940	17.179
	20:50:02 +13:33:30		0.18	0.067	0.044	0.017	0.022	0.020	0.026	0.021
077.6+14.7	19:19:10 +46:14:52	203	0.77	15.266	15.829	17.072	17.546	17.931	18.240	18.447
	19:19:10 +46:14:51		0.22	0.040	0.019	0.013	0.029	0.026	0.034	0.032
104.1+07.9	21:46:09 +63:47:29	86	1.01		19.157	18.736	18.538	18.577	18.425	18.311
	21:46:09 +63:47:30		0.47		0.066	0.0178	0.014	0.018	0.016	0.043
104.2−29.6	23:35:53 +30:28:06	354	1.04	14.007	14.901	15.847	16.255	16.681	16.930	17.152
	23:35:53 +30:28:05		0.02	0.048	0.035	0.025	0.024	0.016	0.013	0.043

Continued on next page

Table 2.6 – continued from previous page

PNG	RA DEC	MajDiam (arcsec)	Sep. (arcsec)	FUV	NUV	g	r	i	z	y
						(AB magnitude)				
110.6−12.9	23:39:11 +48:12:29	33	0.92	19.070	20.065	20.480	20.698	20.825	20.896	20.949
	23:39:11 +48:12:30		0.41	0.061	0.047	0.0302	0.040	0.037	0.060	0.097
117.5+18.9	22:42:25 +80:26:32	34	0.96	17.052	17.792	18.839	19.113	19.454	19.742	20.038
	22:42:25 +80:26:33		1.15	0.115	0.039	0.024	0.033	0.027	0.029	0.053
122.1−04.9	00:45:35 +57:57:35	36	1.83		20.185	19.960	20.026	20.177	20.338	20.103
	00:45:35 +57:57:36		0.66		0.080	0.0310	0.040	0.033	0.043	0.054
138.8+02.8	03:10:19 +61:19:01	46	2.74		18.960	16.711	16.461	16.428	16.362	16.376
	03:10:19 +61:19:03		0.17		0.100	0.0155	0.030	0.036	0.028	0.035
144.3−15.5	02:45:24 +42:33:05	20	1.22	17.997	18.665	19.856	19.987	19.894	19.914	19.837
	02:45:24 +42:33:04		0.41	0.049	0.051	0.0262	0.015	0.016	0.024	0.033
144.5+06.5	04:06:59 +60:55:14	57	2.44	16.535	16.749	14.657	14.252	14.200	14.280	14.161
	04:06:60 +60:55:15		1.51	0.092	0.021	0.015	0.034	0.021	0.019	0.040
153.7+22.8	06:43:55 +61:47:25	148	0.72	17.228	17.943	18.494	18.805	19.037	19.215	19.209
	06:43:55 +61:47:24		0.27	0.002	0.040	0.022	0.021	0.017	0.026	0.038
164.8+31.1	07:57:52 +53:25:17	394	2.32	14.673	15.602	16.854	17.370	17.786	18.067	18.280
	07:57:51 +53:25:18		0.10	0.059	0.045	0.019	0.019	0.046	0.037	0.029
171.3-25.8	03:53:37 +19:29:39	54	2.00	18.048	18.550	18.007	18.066	18.253	18.274	18.335
	03:53:36 +19:29:38		2.13	0.020	0.039	0.015	0.011	0.032	0.015	0.021
205.1+14.2	07:29:03 +13:14:49	750	1.52	14.147	14.737	15.752	16.210	16.554	16.894	17.097
	07:29:03 +13:14:48		0.29	0.028	0.081	0.023	0.023	0.018	0.013	0.024
211.4+18.4	07:55:11 +09:33:09	105	0.64	15.610	16.200	17.624	18.159	18.566	18.884	19.224
	07:55:11 +09:33:09		0.07	0.086	0.031	0.040	0.085	0.053	0.052	0.061
217.1+14.7	07:51:38 +03:00:21	396	4.68	15.121	15.787	17.158	17.644	18.056	18.355	18.531
	07:51:38 +03:00:18		0.17	0.039	0.055	0.023	0.018	0.032	0.033	0.038
219.1+31.2	08:54:13 +08:53:53	970	0.37	13.508	14.160	15.315	15.801	16.141	16.354	16.473
	08:54:13 +08:53:53		0.24	0.100	0.037	0.012	0.025	0.025	0.021	0.025

Continued on next page

Table 2.6 – continued from previous page

PNG	RA DEC	MajDiam (arcsec)	Sep. (arcsec)	FUV	NUV	g	r	i	z	y
						(AB magnitude)				
253.5+10.7	08:57:46 −28:57:36	110	1.58	16.572	16.828	17.090	17.405	16.676	17.450	16.771
	08:57:46 −28:57:36		0.64	0.012	0.036	0.066	0.027	0.015	0.021	0.031
270.1+24.8	10:34:31 −29:11:15	54	1.31	14.387	15.022	16.294	16.742	17.046	17.367	17.564
	10:34:31 −29:11:14		0.22	0.014	0.041	0.012	0.012	0.041	0.012	0.013
326.7+42.2	14:04:26 −17:13:41	47	1.11	17.870	18.493	17.704	17.186	16.956	16.876	16.804
	14:04:26 −17:13:41		0.76	0.057	0.084	0.021	0.008	0.014	0.019	0.013

Notes: RA and DEC are the positions from the `PNcat` (top) and from the revised positions from `GPNcatxSDSSDR14xPS1DR2` (bottom). Sep. indicates the separation between `PNcat` and GALEX coordinates (top) and `PNcat` and PS1 MDS coordinates (bottom).

2.4 New Observational Data for Southern GALEX PNe

Since SDSS and PS1 only cover the northern hemisphere, leaving some southern GALEX sources out, we obtained observations of the southern hemisphere of 13 PNe using the telescopes from Las Cumbres observatory (LCO). We only selected PNe containing the flag "Resolved" in the, `galexClass`=1, column in `GPNcatxSDSSDR14xPS1DR2` catalog.

The CCD camera SBIG mounted on the 0.4 m telescopes of the LCO network was used to obtain images in the SLOAN g, r, and i bands. The STL-6303 detector was used. The detector has 1534×1024 pixels with a pixel scale of $1\farcs142\,\mathrm{pix}^{-1}$ (with a binning of 2×2). The resulting field-of-view is 15×10'. Observation logs are presented in Table 8.1. Data were reduced by using a dedicated LCO reduction pipeline (called BANZAI[11]). Astrometry was carried out using the `Astrometry.net`[12] web tool.

Fluxes were extracted using a PYTHON script using the *Source Extraction and Photometry* (SEP; Barbary, 2016) tool. SEP is mostly based on SExtractor routines. Aperture photometry (using a radius of $3\farcs5$) was performed on each field using the photometric scale of the American Association of Variable Star Observers Photometric All-Sky Survey (APASS), which provides magnitudes in the AB magnitude system. This procedure directly calibrates the SLOAN g, r, and i bands common to both LCO and APASS, using local standard stars (field stars).

To calibrate our fields to the APASS photometric scale, we performed differential aperture photometry. The aperture magnitude, m, of a star is related to the measured instrumental magnitude by

$$m = m_{\mathrm{inst}} + ZP + kX \tag{2.7}$$

where ZP is the instrumental zero point (defined as the magnitude of an object that produces one count per second on the CCD), k is the atmospheric extinction, and X is the airmass in the middle of the observation. The ZP and the kX coefficient are equal for all the stars in the frame. As a result, the difference in magnitude between two stars, 1 and 2, is given by

$$\begin{aligned} m_1 - m_2 &= m_{\mathrm{inst}\,1} + ZP + kX - (m_{\mathrm{inst}\,2} + ZP + kX) \\ &= m_{\mathrm{inst}\,1} - m_{\mathrm{inst}\,2} \end{aligned} \tag{2.8}$$

[11] https://github.com/LCOGT/banzai
[12] nova.astrometry.net

and finally,

$$m_1 = m_{\mathrm{inst}\,1} + (m_2 - m_{\mathrm{inst}\,2}) = m_{\mathrm{inst}\,1} + zp \tag{2.9}$$

with $zp = (m_2 - m_{\mathrm{inst}\,2})$.

Aperture photometry, with an aperture radius of $3''.5$, was performed also on each observed field to obtain zp. Then, we performed aperture photometry on the CSPN using the same aperture. A local annulus (with size twice the aperture used) was employed to subtract the nebular emission from the CS. Then, we used equation 2.9 to calibrate the CS magnitude to the AB system. Results are shown in Table 2.7.

TABLE 2.7— The isolated CSPNe sample o the PNe observed at LCO.

PNG	RA DEC	MagDiam (arcsec)	Sep. (arcsec)	FUV	NUV	g	r	i
				(AB magnitude)				
243.8−37.1	05:03:02 −39:45:44	21	1.21	13.422	14.192	15.433	15.769	16.176
	05:03:02 −39:45:44			0.011	0.009	0.044	0.044	0.050
274.3+09.1	10:05:46 −44:21:33	42	0.53	14.763		16.624	17.089	17.359
	10:05:46 −44:21:34			0.014		0.057	0.057	0.067
283.6+25.3	11:26:44 −34:22:11	200	1.31	14.589	15.293	16.005	15.816	15.642
	11:26:44 −34:22:10			0.013	0.046	0.086	0.086	0.165
286.8−29.5	05:57:02 −75:40:23	61	0.73	14.029	14.736	15.953	16.344	16.637
	05:57:02 −75:40:22			0.075	0.044	0.035	0.035	0.035
291.4+19.2	11:52:29 −42:17:39	30	0.70	15.197	15.134	16.657	16.802	17.037
	11:52:29 −42:17:39			0.1334	0.054	0.039	0.039	0.067
308.2+07.7	13:28:05 −54:41:58	19	0.20		17.542	17.202	17.344	17.496
	13:28:05 −54:41:58				0.039	0.070	0.070	0.066
309.1−04.3	13:53:57 −66:30:51	10.7	2.65		14.200	9.976	9.688	10.808
	13:53:57 −66:30:53				0.013	0.074	0.074	0.130
316.1+08.4	14:18:09 −52:10:40	14	2.34		14.090	12.443	11.983	12.421
	14:18:09 −52:10:38				0.010	0.082	0.082	0.073
326.0−06.5	16:15:42 −59:54:01	1.8	2.69		14.378	12.890	12.325	12.772
	16:15:42 −59:53:59				0.012	0.075	0.075	0.054
329.0+01.9	15:51:41 −51:31:28	72	1.38		15.772	14.126	13.764	13.563
	15:51:41 −51:31:29				0.022	0.038	0.038	0.053
331.3+16.8	15:12:51 −38:07:34	7	2.95	13.827	14.100	11.353	12.303	13.486
	15:12:51 −38:07:31			0.011	0.006	0.164	0.164	0.101
349.3−01.1	17:22:16 −38:29:03	48	3.79		16.787	15.574	15.239	15.173
	17:22:16 −38:28:60				0.041	0.133	0.133	0.140
358.9−00.7	17:45:58 −30:12:01	9	0.61		16.581	12.315	10.579	10.859
	17:45:58 −30:11:60				0.011	0.090	0.090	0.164

Notes: RA and DEC are the positions from the `PNcat` (top) and from the revised positions from the observed CSPNe (bottom). Sep. indicates the separation between `PNcat` and GALEX coordinates.

2.5 Description of the GPNcatxSDSSDR14xPS1 Catalog

The catalog includes a total of 2411 PNe with measurements in either GALEX, SDSS DR14, or PS1 MDS surveys (GPNcatxSDSSDR14xPS1; a total of 8917

rows by including multiple matches and repeated observations), from a total of 3687 PNe in our PNcat. The catalog, in addition to the default column tags on each survey, also includes columns tags with measurements of sizes (diameters; Parker et al., 2016), distances (Stanghellini & Haywood, 2010; González-Santamaría et al., 2019, ; flux and Gaia DR2 distances, respectively), and the spectral classification of the CS (Weidmann & Gamen, 2011) for each PN when available. The new observations and the extracted CSs photmetry is also included for the selected PNe (see Sections 2.3.3 and 2.4). Table 2.8 gives the description of each column tag included in the catalog.

Table 2.8— Catalog columns.

Tag	Description
RA	source's Right Ascension (degrees) (see `cat_ref` to see the coordinate reference catalog).
DEC	source's Declination (degrees) (see `cat_ref` to see the coordinate reference catalog.
RAJ2000	Same as `RA` (hms).
DEJ2000	Same as `DEC` (dms).
PN	Planetary Nebula common name.
PNG	Name given in PN G nomenclature (PN GLLL.1+BB.b).
d	Distance to the PN (pc; Stanghellini & Haywood, 2010).
e_d	Error in distance to the PN (pc; Stanghellini & Haywood, 2010).
F5GHz	Flux at 5GHz (Stanghellini & Haywood, 2010).
coord_ref	Catalog of coordinates reference (Kerber et al., 2003; Parker et al., 2016; Stanghellini & Haywood, 2010; Weidmann & Gamen, 2011).
SpT	Spectral type of the CS (Weidmann & Gamen, 2011).
r_SpT	.
PNstat	Status of the PN: L=Likely, T=True, and P=Probably (Parker et al., 2016).
Catalogue	Catalog reference for PN diameter measurements. Obtained from Parker et al. (2016).
MajDiam	Major diameter (arcseconds).
MinDiam	Minor diameter (arcseconds).
IAUName	GALEX IAU name for the source.

Continued on next page

Table 2.8 – *Continued from previous page.*

Tag	Description
galex_objid	GALEX identifier for the source.
photoExtractID	Pointer to photoExtract table.
galex_ra	GALEX Right Ascension for the source. (degrees)
galex_dec	GALEX Declination for the source. (degrees)
E_bv	$E(B-V)$ Galactic reddening (from Schlegel et al., 1998, maps).
glon	GALEX Galactic longitude for the source (degrees).
glat	GALEX Galactic latitude for the sources (degrees).
fov_radius	GALEX field-of-view radius from the center of the field to the source (from visits table).
x_flux	GALEX "best" flux measurement (photon counts; x=fuv or nuv).
x_fluxerr	GALEX "best" flux error measurement (photon counts).
x_mag	GALEX "best" magnitude measurement (AB mag).
x_magerr	GALEX "best" magnitude error measurement (AB mag).
x_artifact	FUV or NUV artifact (logical OR near source).
x_MAG_ISO	GALEX Isophotal magnitude (AB mag).
x_MAGERR_ISO	GALEX Isophotal magnitude error (AB mag).
x_MAG_APER_n	GALEX Aperture magnitude (AB mag; n=1–7).
x_MAGERR_APER_n	GALEX aperture magnitude error (AB mag).
x_MAG_AUTO	GALEX Kron magnitude (AB mag).
x_MAGERR_AUTO	GALEX Kron magnitude error (AB mag).
x_KRON_RADIUS	Kron apertures in units of A or B.
x_A_IMAGE	Profile rms along major axis (in image units).
x_B_IMAGE	Profile rms along minor axis (in image units).
x_THETA_IMAGE	Position angle (in image units).
x_ELLIPTICITY	1−A_IMAGE/B_IMAGE
x_FWHM_IMAGE	FWHM assuming a Gaussian core.
x_CLASS_STAR	S/G classifier output.
gPNRank	gPNRank=0 if is the unique measurement. gPNRank=1 if there is more than 1 match within a 2.″5 match radius from different observation (primary). gPNRank=2 if there is more than 1 match within a 2.″5 match radius but from same observation. gPNRank=3 otherwise.

Continued on next page

Table 2.8 – *Continued from previous page.*

Tag	Description
gGrpRank	Number of members inside each `gPNRank` status > 1.
sdss_objid	SDSS identifier for the source.
mode	SDSS mode=1 for "primary" object. mode=2 for "secondary" object (re-observation). mode=3 for "familly" object (de-blended source).
sdss_type	Type classification of the object in SDSS (3=GALAXY, 6=STAR).
psfMag_x	SDSS PSF magnitude (AB mag; with x=u, g, r, i, z).
psfMagErr_x	SDSS PSF magnitude error (AG mag).
petroMag_x	SDSS Petrosian magnitude (AB mag).
petroMagErr_x	SDSS Petrosian magnitude (AB mag).
flags_x	Object detection flags per band.
sdss_ra	SDSS Right Ascension (degrees).
sdss_dec	SDSS Declination (degrees).
psffwhm_x	FWHM per band.
specObjID	SDSS pointer to the spectrum of object, if exists, else 0.
x	SDSS model magnitude (AB mag; x=u, g, r, i, z).
err_x	SDSS model magnitude error (AB mag).
sPNRank	sPNRank=0 if is the closest source with mode=1 ("primary"). sPNrank=1 if is within 1.″4 from the "primary" and with mode=2. Otherwise sPNRank=3.
sGrpRank	Number of members inside each `sPNRank` status >0.
objName	PS1 object name designation.
ps1_objID	PS1 identifier for the source.
objInfoflag	Information flag bitmask indicating details of the photometry.
qualityFlag	Subset of objInfoFlag denoting whether this object is real or a likely false positive.
raMean	PS1 Mean Right Ascension (degrees).
decMean	PS1 Mean Declination (degrees).
nDetection	The sum of the detections from a single exposure (the number is the sum of the detection of all bands).
xMeanPSFMag	PS1 Mean PSF magnitude (AB mag; with x=g, r, i, z, y).
xMeanPSFMagErr	PS1 Mean PSF magnitude error (AB mag).
xMeanKronMag	PS1 Mean Kron magnitude (AB mag).

Continued on next page

Table 2.8 – *Continued from previous page.*

Tag	Description
xMeanKronMagErr	PS1 Mean Kron magnitude error (AB mag).
xMeanApMag	PS1 Mean Aperture magnitude (AB mag).
xMeanApMagErr	PS1 Mean Aperture magnitude error (AB mag).
pPNRank	pPNRank=0 if is the unique match. Otherwise pPNRank=1 for the primary measurement.
pGrpRank	Number of members with pPNRank¿1.
gmSize	Number of GALEX multiple matches per PN.
smSize	Number of SDSS multiple matches per PN.
pmSize	Number of PS1 multiple matches per PN.
galexClass	GALEX unresolved (=0) and resolved (=1) classification.
sdssClass	SDSS unresolved (=0) and resolved (=1) classification.
ps1Class	PanSTARRS unresolved (=0) and resolved (=1) classification.
GaiaDR2	Gaia DR2 object identifier.
Plx	Measured of parallax by Gaia DR2 (mas).
e_Plx	Measured parallax error by Gaia DR2 (mas).
Dist	Estimated distance (parsec).
e_Dist_x	Estimated low error distance (%).
E_Dist_xa	Estimated high error distance (%).
Height	Galactic height (parsec; González-Santamaría et al., 2019).
Rad	Nebular angular radius (arcsec).
RV	Radial velocity (km/s).
mx	Extracted CSPNe photometry (only resolved PNe; ABmag). x stands for FUV, NUV, SDSS u g r i z, and PS1 g r i z y.
rRA	Revised RA (degrees).
rDEC	Revised DEC (degrees).
m$x$err	Extracted CSPNe photometry error (only resolved PNe; ABmag).
mAperCorr$x$	Aperture correction employed to each filter (ABmag).
mAper$x$	Aperture used for the derived photometry (arcsec).

TABLE 2.9— PS1 Detection table for each PN match in Table 2.8

Tag	Description
RA	source's Right Ascension (degrees) (see `cat_ref` to see the coordinate reference catalog).
DEC	source's Declination (degrees) (see `cat_ref` to see the coordinate reference catalog.
RAJ2000	Same as `RA` (hms).
DEJ2000	Same as `DEC` (dms).
PN	Planetary Nebula common name.
PNG	Name given in PN G nomenclature (PN GLLL.1+BB.b).
ps1_objID	PS1 unique object identifier. Same as in Table 2.8.
detectID	Unique detection identifier.
filterID	Filter identifier (=1–5).
obsTime	Modified Julian date at the midpoint of the observation.
pltScale	Local plate scale at the location of the plate (arcsec/pixel).
posAngle	Position angle (sky-to-chip) at this location (degrees).
ra	Right Ascension (degrees).
dec	Declination (degrees).
zp	Photometric zeropoint (magnitudes).
expTime	Exposure time of the frame/exposure (seconds).
airMass	Airmass at the middle of exposure.
psfFlux	Flux from PSF fit (Janskys).
psfFluxErr	Error on flux from PSF fit (Janskys).
psfMajorFWHM	PSF major axis FWHM.
psfMinorFWHM	PSF minor axis FWHM.
psfTheta	PSF major axis orientation (degrees).
apFlux	Flux in seeing-dependent aperture (Janskys).
apFluxErr	Error on flux seeing-dependent aperture (Janskys).
apRadius	Aperture radius (arcsec).
kronFlux	Kron flux (Janskys).
kronFluxErr	Error on Kron flux (Janskys).
infoFlag	Information flag bitmask indicating details of the photometry.

2.6 Summary

We constructed a photometric catalog of PNe that are in the footprint of the GALEX GR6/GR7 UV surveys and in the SDSS DR16 and PS1 MDS optical databases, covering a unique spectral range from 1340–10 838 Å (FUV–y_{PS1}). Out of the 3687 PNe in PNcat, only 326 are in GALEX, SDSS, and PS1 MDS. The final catalog, GPNcatxSDSSDR14xPS1, contain a total of 8917 rows, which includes the multiple measurements and multiple matches found for each PN in PNcat in a 5 ″ match radius. We ranked each multiple measurement according to its distance to the PN and classified them using the tag `PNRank` for the unique and primary PN UV-optical counterparts (`PNRank=0 and 1, respectively`), "repeated" measurements (re-observations; `PNRank`=2), and field stars (`PNRank>2`).

A separation of resolved and unresolved PNe was made according to GALEX resolution (∼5 ″) We analyzed the different aperture magnitudes provided by the GALEX pipeline and found that, by comparing known PN diameters from previous catalogs (also included in our final table), the difference `NUV_MAG_APER_4`−`NUV_MAG_APER_5`>0 is a good indicator of resolved PN. A total of 417 are classified as resolved in GALEX imaging, and of those, only 54 and 289 have optical counterpart in SDSS and PS1, respectively. For those resolved PNe in GALEX imaging, we extracted the CS flux of a total of 37 PNe using aperture photometry techniques, taking into account that some nebular emission lines (such as He IIλ164 in FUV and [O III]λ4959+5007 in g band) are present in different transmission bands. New observations were made for those resolved PNe found in GALEX imaging in the southern hemisphere (13 PNe).

In general, for statistical analyses, taking `PNRank=0 and 1` may result in the requested PNe measurements. However, for individual SED analysis, each PN should be treated carefully as the catalog may contain fluxes from nearby objects to it. Also, special attention should be made when for a given GALEX source a multiple SDSS or PS1 matches are found. This may indicate that the GALEX flux is a composition of at least 2 stellar sources that are not resolved by GALEX (these objects were assigned with `PNRank>2` to facilitate the analysis).

3

Characterization of binary central stars of planetary nebulae detected by GALEX

Do not look at stars as bright spots only.
Try to take in the vastness of the universe.
Maria Mitchell

ABSTRACT– **The majority of the PNe are not spherical, and current single-star models cannot explain the morphologies we observe. A binary interaction is the preferred channel to form non-spherical PNe. In order to evaluate the role of binarity, we analyze the CS in a sample of PNe with a range of morphologies. In this chapter, we search for double-star spectral-energy distributions , by combining GALEX UV with optical SDSS and PS1 photometry, in a sample of 23 PNe. We select the PN to be analyzed according to their colors in the color-color diagram, and according to the `PNRank` tag for unique and primary measurements in the `GPNcatxSDSSDR14xPS1` catalog. We have constructed a program to identify and characterize binary central stars of PNe based on the Markov-Chain Monte-Carlo method. We have characterized 14 binary CSPNe of which 7 are new binary CSPNe candidates.**

3.1 Introduction

IN this chapter, we will continue the analysis of central stars of planetary nebulae detected in GALEX and optical surveys. We will focus on the resolved

PNe in GALEX imaging (see Chapter 2) from which we isolated the central star photometry.

One of the most important advantages of the use of GALEX UV and optical catalogs is the possibility of detecting a hot and cool component of a possible binary system. A popular method for searching a binary system is the infrared (IR) excess method (see Chapter 1.3.2). The IR excess method is based on the premise that the companion star (main-sequence stars) radiates mostly on IR wavelengths whereas the ionizing star on UV wavelengths (U or B bands). If the system is composed by a hot-star and cool-star then the IR excess method looks for energy excess in IR bands (e.g., normally in I) band. The main difference with respect to the IR excess method is that we will use the entire range of the spectral energy distribution instead of measurements of the excess in specific bands to fit simultaneously the ionizing star (UV excess) and the cool companion. There are many works in the literature, based only in optical photometry, in which they have identified binary systems with a white dwarf component (e.g., Rebassa-Mansergas et al., 2012, 2013). However, the optical photometry is biased toward finding only white dwarf (WD) plus M-type dwarf star systems. The only way to find more massive and hotter white dwarfs with earlier companion stars is through the UV photometry because the ionizing star emits most of its flux toward shorter wavelengths (λ <3000 Å; $T_{\rm eff}$>30 000 K; Bianchi et al., 2018a).

Here we attempt to develop a new method to detect and characterize binary stars in the nucleus of a PN using photometry alone. The aim of the method is to allow the detection and preliminary characterization prior to any spectroscopic analysis.

3.2 Objects selection

3.2.1 Overview

The combined photometry of the GALEX UV catalog with the optical SDSS and PS1 MDS catalogs significantly increase the sensitivity towards high effective temperatures. This can be seen, for example, in Figure 3.1, taken from Bianchi et al. (2011a), which shows the distribution of sources found in GALEX cross correlated with SDSS in the plane FUV−NUV versus NUV−r. Figure 3.1 shows a density plot of extended (black points) and point-like (purple points) sources from Bianchi et al. (2011b), and overlaids are models of main-sequence (MS; red line) stars, super giant (SG; yellow line) stars, white dwarfs (WD; purple line), galaxies (gree line), and quasi stellar objecets (QSO; cyan lines). In this figure is possible to separate the very hot sources from other stellar

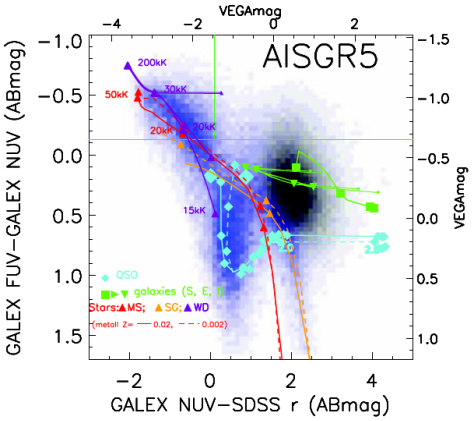

FIGURE 3.1— Color–color diagrams for the GALEX UV sources matched to SDSS sources, at AIS depth. Blue/black densities are point-like/extended sources, respectively. Overlaid are models of stars, QSO, and galaxies, labeled in the figure. Taken from Bianchi et al. (2011a).

objects (see Bianchi et al., 2011a, and references therein).

GALEX matched with optical surveys could be very useful to detect binary stars in the core of PNe. If the binary components differ in their $T_{\rm eff}$, the individual contribution of each component to the overall observed magnitudes is non-uniform across the spectral energy distribution (SED). In a binary central star of PN (CSPN), a double peaked SED is expected. The ionizing star will have $T_{\rm eff}$ higher than 30 000 K, while the companion may have cooler $T_{\rm eff}$. Figure 3.2 shows an example of a single CSPN (left), with $T_{\rm eff}$=100 000 K, and a binary CSPN (right), with an $T_{\rm eff\,hot}$ = 100 000 K and $T_{\rm eff\,cool}$ = 4700 K.

3.2.2 Color-color diagrams analysis

The observed PNe detected in UV and optical bands from GPNcatxSDSSDR14xPS1 (GPNSPcat), are shown in color-color diagrams in Figure 3.3. Model colors of major classes of astrophysical objects, taken from Bianchi et al. (2007, 2011a),

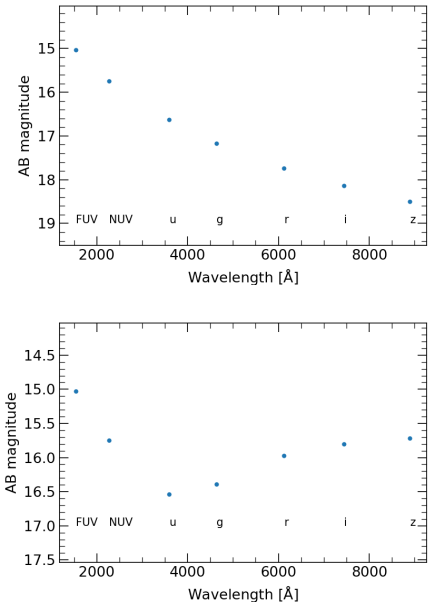

FIGURE 3.2— Model SED in GALEX plus SDSS filters of a WD with an $T_{\rm eff}$=100 000 K (top) and the SED of a binary CSPNe (bottom) composed by a hot star with $T_{\rm eff}$=100 000 K, a cool star with $T_{\rm eff}$=4700 K, $R_{\rm cool}/R_{\rm hot}$ = 40, at a distance of 1 kpc.

are also shown to guide the eye in interpreting the distribution of PNe. We refer to Bianchi et al. (2007, 2011a); Bianchi & Shiao (2020) for other similar figures and description of the model grids. For unresolved PNe, as the majority of the objects are assumed to be compact PNe, we used the best GALEX magnitude, the `petromag` from SDSS, and the `MeanKronMag` from PS1. These magnitudes are the integrated flux of the best-fit source shape on each database. In the case of the resolved PNe, we used the CS photometry of PNe as estimated in Section 2.3.3.

In Figure 3.3, unresolved PNe are shown with blue diamonds and CS photometry of resolved PNe with red crosses. Also, unresolved and resolved sources, as classified by SDSS `class`, are shown as a density blue and black points, respectively, for the sources in the *Galex Ultraviolet Catalog* (GUVcat, Bianchi et al., 2017) matched with SDSS DR14 (Bianchi et al., 2019). Model colors are shown with different symbols and colors, explained in the legend. The effect of interstellar dust is shown as an arrow in the upper-right corner of each panel, for a Galactic typical extinction with $R_{\rm V} = 3.1$ and $E(B-V) = 0.3$ mag.

In all the colors, but specially in FUV−r versus r−i (top panel of Fig. 3.3) the unresolved PNe are very well separated from the CSPNe. A number of unresolved PNe that are located in the same color space as the CSPNe correspond to a PNe with low surface brightness (i.e., the nebular emission is not significantly contributing to the stellar flux).

An interesting feature of both color-color plots is that most of the CSPNe have colors redder than the WD loci (purple line). This could be an indication, as stated before by Bianchi et al. (2007, 2011a); Bianchi & Shiao (2020), that the CSPN has a cool companion (e.g., Douchin et al., 2015; Barker et al., 2018), or that the PNe is reddened by high amounts of circumstellar dust.

It is also remarkable, as shown in the bottom panel of Fig. 3.3, that unresolved PNe are very well separated from all other astrophysical objects. Most of the PNe are unresolved in GALEX imaging (or with a diameter less than 5 ″) but may include contamination by PNe resolved in optical bands (with diameters between 1.5–5.0 ″).

From the point of view of stellar evolution, the sample presented in this work includes essentially all stages of the PN evolution: from probably young PNe (or post-AGB stars) that have just expelled their envelopes and are rapidly crossing the H-R diagram towards higher $T_{\rm eff}$ at constant luminosity, to compact PNe (or with small diameter) and hot WDs, which are fading both in $T_{\rm eff}$ and luminosity (e.g., extended PNe with very low surface brightness). This is supported by the CSPNe loci, as $T_{\rm eff} \gtrsim 50\,000$ K for most of them (as inferred by the WDs model colors in the top panel of Fig. 3.3).

Starting from the available photometry from the `GPNcatSDSSDR14xPS1` cat-

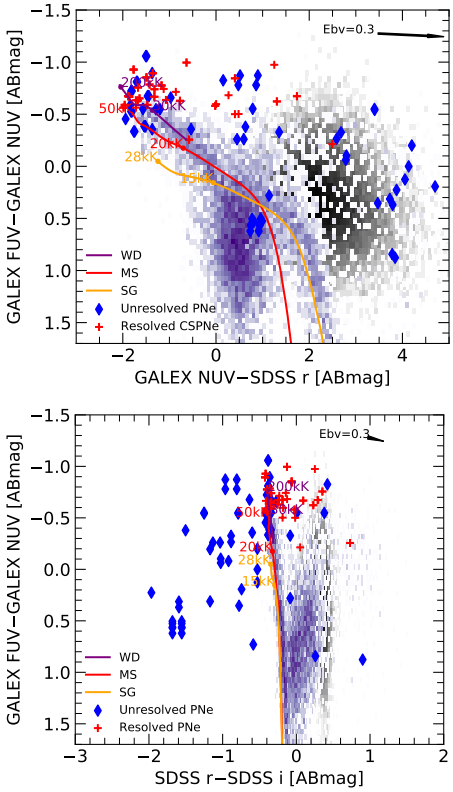

FIGURE 3.3— Color-color diagrams for unresolved PNe (blue diamonds) and CSPNe photometry of resolved PNe (red crosses) detected in GALEX UV matched with SDSS and PS1. Blue/black densities are point-like/extended sources, respectively (Figure adapted from Bianchi et al., 2007, 2011a). The purple stellar sequence (label 'WD') is for $\log(g) = 7.0$. Main-sequence (red) and supergiant (yellow) stellar sequences are for $\log(g) = 5.0$ and $\log(g) = 3.0$, respectively.

alog we have selected PNe that have both UV bands, FUV and NUV, from the CSPNe presented in Chapter 2, that are classified as "unique" or "primary" measurement (see Chapter 2.3). Among these objects, we also selected PNe that were classified as unresolved, located in the same color space as the WD loci.

3.3 The fitting method

3.3.1 Model magnitudes

Before the characterization of binary CSPNe using single epoch photometry we have to select the appropriate set of model atmospheres that will be used in the fitting process. For the cool companion, we used the local thermodynamic equilibrium (LTE) BT−Settl stellar atmosphere models from Phoenix/NextGen group (Hauschildt, 1999; Allard et al., 2012). The BT-Settl models offer synthetic spectra with 2600 K$<T_{\rm eff}<$70 000 K and $-0.5 < \log(g) < 5.5$. In the case of the hot star (WD star) we used the H-He non-LTE TLUSTY (Hubeny, 1988) atmosphere models developed by Bianchi et al. (2007) which covers the range 30 000 K$<T_{\rm eff}<$200 000 K and 4.0$<$ log(g) $<$9.0. In both cases, we used the solar composition atmosphere models. For this analysis, we fixed the value of $\log(g_{\rm hot})$=7 for the hot-WD star as has been proven that it is not very sensitive to the colors of the binary system (see Table A1 from Barker et al., 2018). In the case of the companion star, we fix the value to $\log(g_{\rm cool})$=5, as most of the companion stars found in the literature using a color excess methods are presumed to be MS stars (e.g., De Marco et al., 2013; Rebassa-Mansergas et al., 2013; Douchin et al., 2015; Barker et al., 2018).

For each model atmospheres, we integrated the theoretical spectra in the GALEX UV bands, and SDSS and PanSTARRS optical bands. The convolution of the flux, $f(\lambda)$, with the response curve of the relevant filters,$R(\lambda)$, is

$$F_\nu = \frac{\int f(\lambda) R(\lambda) \lambda \, d\lambda}{c \int R(\lambda) \lambda^{-1} \, d\lambda}, \tag{3.1}$$

where c is the speed of light (2.99792548×10^{18} Å s^{-1}). The resulted flux and the parameters of the spectra were compiled in two separated tables: one for the cool companion, and one for the hot star. The `model magnitude` tables contain the columns: $T_{\rm eff}$, log(g), FUV, NUV, SDSS *u, g, r, i* ,*z*, and PS1 *g, r, i , z* and *y*. Magnitudes of both stars are combined in order to create the combination of colors to be used in the fitting process (see 3.3.2).

TABLE 3.1— Example of color indexes using GALEX and SDSS filter systems.

Color indexes:					
FUV−NUV	FUV−u	FUV−g	FUV−r	FUV−i	FUV−z
	NUV−u	NUV−g	NUV−r	NUV−i	NUV−z
		$u-g$	$u-r$	$u-i$	$u-z$
			$g-r$	$g-i$	$g-z$
				$r-i$	$r-z$
					$i-z$
Free parameters:					
$T_{\rm hot}$		$T_{\rm cool}$		β	

3.3.2 Basic equations

Theoretically, the equation that describes the magnitude observed, in the AB system, of a binary CSPNe is described by, with no extinction,

$$m_{\rm AB} = -2.5\log([F_\nu^{\rm hot} + F_\nu^{\rm cool}\beta^2]\alpha^2) - 48.6, \tag{3.2}$$

with

$$\begin{aligned}\beta &\equiv \frac{R_{\rm cool}}{R_{\rm hot}} \\ \alpha &\equiv \frac{R_{\rm hot}}{D}\end{aligned} \tag{3.3}$$

where $R_{\rm cool}$ and $R_{\rm hot}$ is the radius of the cool star and the WD star, respectively, and D is the distance to the CSPNe.

The Equation 3.2 would be enough to fit any binary. However, it is very difficult to achieve accurate values of the stellar parameters ($T_{\rm hot}$, $T_{\rm cool}$, α, and β) with few observable values (7 points from GALEX and SDSS or GALEX and PS1). Then, if we consider only color indexes instead of magnitudes, the ratio of the $R_{\rm hot}$ and distance, D, would be eliminated, as the logarithmic nature of the magnitude makes these factors cancel out in the subtraction. For a two filter system, A and B, this would be

$$m_{\rm A} - m_{\rm B} = -2.5\log\left(\frac{A_\nu^{\rm hot} + A_\nu^{\rm cool}\beta^2}{B_\nu^{\rm hot} + B_\nu^{\rm cool}\beta^2}\right) \tag{3.4}$$

If we extrapolate Equation 3.4 to a seven filter system, then we will have 21 color combinations and 3 free parameters as shown in Table 3.1.

Note that the model magnitudes from each component will be retrieved from its own table and that the fluxes will be interpolated between parameters. The extinction will be assumed according to the values observed in the literature (see Section 3.5).

3.3.3 SED fitting methodology

Now that we have defined the basic equations, the next step is to define the method function that we used to fit the model to the observed SED. This is, for a given set of categorized observed data, and a model that predicts the population of each category, the χ^2 statistic describes the goodness of fit. This is

$$\chi^2 = \sum_{i=1}^{n} \frac{(y_i - E_i)^2}{\sigma_i^2} \tag{3.5}$$

where E_i is the model from Equation 3.4, y_i is the observed data, σ is the error of the observation, and n is the nth category (color index). As we were using the color index of each observation, the error (σ) is defined as

$$\sigma^2 = \sigma_{\rm A}^2 + \sigma_{\rm B}^2 \tag{3.6}$$

where $\sigma_{\rm A}$ and $\sigma_{\rm B}$ represent the error of the observed magnitudes in the filters A and B, respectively.

We then proceeded to minimize the value of χ^2 varying the stellar parameters of the models. The idea behind this method is that the difference between the model values and observed values must be only statistic fluctuations if the models are qualitatively correct. From know on, we will call the resulted parameters of χ^2 method as the *maximum likelihood estimation* (MLE).

Besides the stellar parameters we also calculated the uncertainties related to them. By examining a random sample from the observed distribution was possible to obtain the errors related to the fitted parameters. In other words, we required to find an estimate of the posterior probability function (the distribution of parameters that is consistent with our observed values) of the stellar parameters of the system given by our observations.

In mathematics, the posterior probability function is defined as

$$p(\mu|y) \propto p(y|\mu)p(\mu) \tag{3.7}$$

where μ indicates a set of parameters of interest (in this case the $T_{\rm eff}$ of both stars and α) and y indicates the observed data (color indexes). The likelihood function, $p(y|\mu)$, is defined as

$$\ln[p(y|\mu)] = -0.5 \sum_{i=1}^{n} \frac{(y_i - E_i(\mu))^2}{\sigma_i^2}, \tag{3.8}$$

whereas the prior function, $p(\mu)$, is given by

$$\ln[p(\mu)] = 0 \text{ if } \begin{cases} 30\,000\,\mathrm{K} < T_{\rm hot} < 200\,000\,\mathrm{K} \\ 2600\,\mathrm{K} < T_{\rm cool} < 70\,000\,\mathrm{K} \\ |\beta| > 1,\ \beta = 0 \text{ otherwise} \end{cases} . \tag{3.9}$$

The algorithm that maximizes the likelihood function is called *Markov-Chain Monte-Carlo* (MCMC). The implementation of the MCMC algorithm was carried out using the PYTHON "emcee" code (Foreman-Mackey et al., 2013) under the *Non-Linear Least-Squares Minimization and Curve-Fitting for Python* (LMFIT[1]) library. The MCMC maximized the probability of observing certain data-set of colors given a set of parameters. This is

$$\ln[p(T_{\rm hot}, T_{\rm cool}, \beta|color)] = \ln[p(color|T_{\rm hot}, T_{\rm cool}, \beta)] + \ln[p(T_{\rm hot}, T_{\rm cool}, \beta)]. \quad (3.10)$$

Given the need for a smooth parameter space for the MCMC algorithm, we used the "scipy" (Virtanen et al., 2020) library to interpolate the synthetic magnitudes across the parameters space. We used the MLE to initialize the MCMC in favor of the convergence.

Finally, the stellar parameters resulted from the Eq. 3.4 were used to solve the Eq. 3.2. This time, we assigned only the $T_{\rm hot}$, $T_{\rm cool}$, and the α factor as free parameters.

The SED fitting method was repeated two times: one for single star system (setting β=0) and one for a binary system. Both fits were tested with Eq. 3.5 and the best fit was taken as the final result.

Note that with this analysis made with UV and optical bands is possible to identify binary systems composed by a hot-WD and a cooler companion. However, the fitted scaling factors, α and β, are conditioned to the value of $E(B-V)$, $\log(g_{\rm hot})$, and $\log(g_{\rm cool})$ assumed. Hence, the scaling factors should be taken as lower limits allowing the detection of binary systems and preliminary characterization. Nevertheless, further spectroscopic analysis would be needed.

3.4 Testing the SED fitting code

Every code must be checked first before being implemented in real-world cases. In this section, we will test the code in one example with extreme parameter values and, a second one with a PN example.

3.4.1 Test 1: WD plus M2V star companion

The first test used the parameters shown in Table 3.2. We generated synthetic data from the model described by Equation 3.4 and added some Gaussian noise around the errors expected from the observed magnitudes (see Figure 3.4).

The corner-plot, shown in Figure 3.5, presents the result of the posterior probability function of Eq. 3.4 (top panel) and Eq. 3.2 (bottom panel). It repre-

[1] https://lmfit.github.io/lmfit-py/

TABLE 3.2— Parameters of Test1 for a binary CSPNe.

Parameter	WD	M-type
$T_{\rm eff}$	100 000 K	3500 K
$\log(g)$	7.0	5.0
R_* [$R_\odot$]	0.02	0.4
D [pc]	1000	

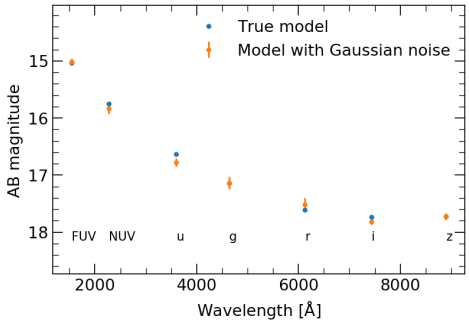

FIGURE 3.4— Binary CSPNe composed by a WD in the cooling track and a main-sequence M-type star. Errors are generated from Gaussian noise around errors expected from real observations.

sents the correlation for each parameter and the diagonals shows the marginalization of each value independently. The Figure 3.5 demonstrates the successful constraining of the β ratio and $T_{\rm cool}$. However, $T_{\rm hot}$, for such high $T_{\rm eff}$, is a little overestimated as UV GALEX bands alone are not sensitive to $T_{\rm eff} \geq 10^5$ K (see Figure 7 from Bianchi et al., 2011a). It is worth to point out that the residual values between the real parameters of the model and those resulted from the posterior probability function are very small, and that the method can provide a reliable estimation of the stellar parameters of the CSPNe.

3.4.2 Test 2: Abell 70

In the same way, as Test 1, we tested the method by trying to find the stellar parameters of the binary CSPNe of PN G037.1−25.4 (Abell 70). The photometry values was taken from Table 2.6, described in Chapter 2.3, from the matched catalogue of GPNSPcat. The photometry was extinction corrected using c(H_β)=0.07 from Acker et al. (1992b) using the extinction law of Cardelli et al. (1989).

It is possible to obtain a rough value of the $T_{\rm hot}$ by using the difference in the UV color. Assuming that the companion star is not contributing to the flux in the FUV−NUV=−0.824 color, we can infer that the $T_{\rm eff}$ of the CS is, at least, $T_{\rm hot} > 100\,000$ K (see Figure 7 in Bianchi et al., 2011a). However, we can see from Figure 3.6 that there is a very good correlation between the stellar parameters of the companion star.

We can infer the radius of the companion star by assuming a nominal value for the ionizing star $R_{\rm wd} = 0.06$, obtaining $R_{\rm cool} = 5.37\,{\rm R}_\odot$. This radius correspond with a G8IV star as suggested by Miszalski et al. (2012).

It is evident in any case that the weakness of the method is whether it is possible to identify a cool companion earlier than an M0V-M2V. We are testing here a WD that is in the cooling track with an M2V companion star in Test 1 (Section 3.4.1) and a WD with a probably G8IV companion in this section. If the WD were in the constant luminosity phase, its radius would be one order of magnitude larger, making impossible to identify companion stars of later types than K5V (see Figure 2 of Barker et al., 2018). Although it is not possible to fit $T_{\rm hot} \geq 100\,000$ K, as GALEX UV bands are too broad to be sensitive to $T_{\rm eff}$, it is possible the identification of a binary system and a preliminary characterization of the cool companion star.

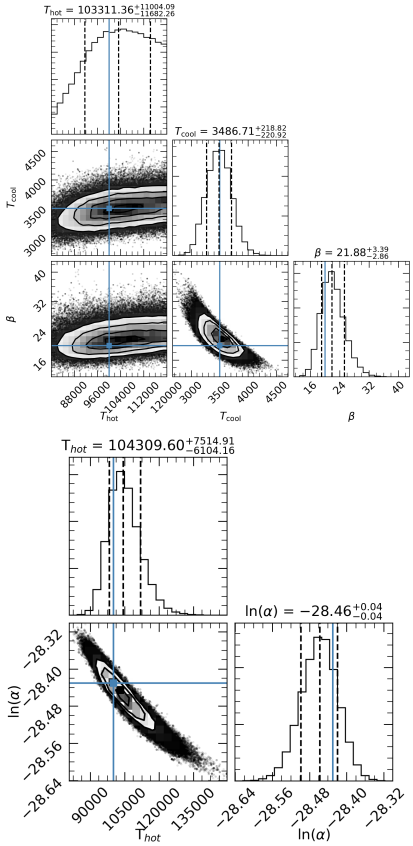

FIGURE 3.5— The corner-plot of the solution of the posterior probability function of the Eq. 3.4 (top panel) and Eq. 3.2 (bottom panel). It shows the correlation between the different parameters. The diagonal particularly shows the marginalized distribution for each parameter independently. The blue lines indicate the true values, whereas the dashed lines represent the quantiles at 15%, 50%, and 85%.

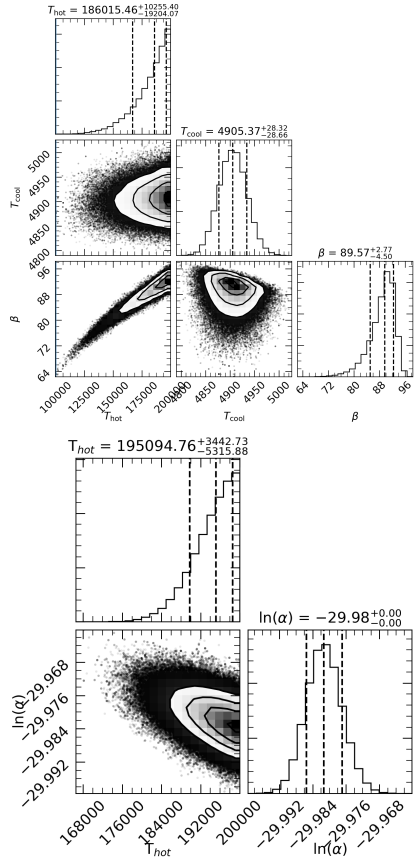

FIGURE 3.6— Same as Figure 3.5 but for Abell 70. In this example the $T_{\rm hot}$ is out of the range of parameters, however, there is a good correlation for the companion star.

3.5 Results

In this section, we will present the results obtained from fitting the observed photometry of GPNSPcat.

The interstellar extinction is an important factor in the SED fitting process. In some cases, depending of the observed filters and on $T_{\rm eff}$ of each component of the binary system, the value of $E(B-V)$ is degenerated with the stellar parameters of the system (e.g., Figure 3.7). Objects that are located at low Galactic latitudes (near the Galactic plane) are more affected by the interstellar extinction. In the fitting process, we adopted the values $E(B-V)$ found in the literature (as shown in Tables 3.3 and 3.4). The reddening map of Schlafly & Finkbeiner (2011) and Green et al. (2018) were also used for those PNe with no previous $E(B-V)$ literature measurement.

The fitting process was carried out in two groups: PNe located at high Galactic latitudes and PNe with a reliable Gaia DR2 distance. Objects at low Galactic latitudes were rejected for the reason described above. Some exceptions were those with a reliable estimation of $E(B-V)$ found in the literature.

3.5.1 PNe with $|b| > 15$

Table 3.3 shows the results obtained from the posterior probability function for 12 PNe at high Galactic latitudes. Ten of the PNe presented here (83%) resulted in a binary system. It is interesting to note that the majority of the binary detections consist of a hot-WD plus a late-type star companion, as judged by the resulted $T_{\rm cool}$, in agreement with previous works (Barker et al., 2018; Douchin et al., 2015). This is also due to the wavelength coverage available, that has less sensitivity to binaries with a moderately hot companion (see the color-color diagrams in Bianchi & Shiao, 2020).

In the case of PN G038.1−25.4 and PN G283.6+25.3, the best fitting parameters show clear evidence of a cool companion star in the SED. However, the observed colors are beyond the range of model colors, implying a hotter CS than the maximum $T_{\rm eff}$ of the fitting range of parameters that is not likely, or most probably some photometric error of extra component in the flux such as emission lines (see Section 2.3). Similarly, PN G171.3−25.8, where the $T_{\rm eff}$ is presumed to be colder than the fitting range of parameters.

Figure **??** and **??** shows the photometry of the PNe overlaid with 100 samples of the distribution of the posterior probability function. We corrected the photometry for extinction using the Cardelli et al. (1989) (hereafter CCM89) extinction law with the values reported in Table 3.3. The best solution is where most of the samples overlap (darker parts of the SED). However,

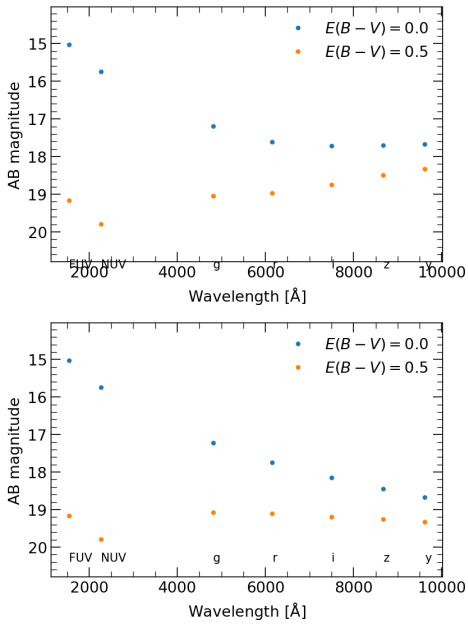

FIGURE 3.7— Binary CSPN composed by a WD with $T_{\rm hot} = 100\,000$ K and a main-sequence companion with a $T_{\rm cool} = 3500$ K (top). Single CSPN WD star with $T_{\rm hot} = 100\,000$ K (bottom). Both are fixed at a distance of 1 kpc and with $R_{\rm cool}/R_{\rm hot} = 20$. The shape of the Binary CSPN SED could be reproduced by adding high amount of extinction.

TABLE 3.3— Results of the fitting process for PNe located at high latitudes.

PNG	$E(B-V)$ (mag)	$T_{\rm hot}$ (K)	$T_{\rm cool}$ (K)	$\log(\alpha)$	β
003.3+66.1	0.00±0.06 (1)	100 000:	4245.89±90.0	−12.56±0.01	10.37±0.50
019.8−23.7	0.00±0.05[a]	74 531±14000	8850.00±50.0	−-12.65±0.01	6.87±0.60
038.1−25.4	0.0479 (2)	195 000:	4905.37±30.0	−13.02±0.01	82.24±4.00
117.5+18.9	0.1208[a]	150 000:		−12.66±0.06	
144.3−15.5	0.0852[a]	190 000:	4068.37±50.0	−12.97±0.01	27.87±1.10
153.7+22.8	0.13±0.03 (3)	45 660±2000	3804.86±400.0	−12.33±0.01	5.89±1.00
171.3−25.8	0.1000[a]	30 000±100	8000.00±300.0	−12.30±0.01	7.28±2.00
211.4+18.4	0.0000 (1)	85 500±15 000		−12.39±0.04	
270.1+24.8	0.0454[a]	81 642±5000	4000.00±700.0	−12.09±0.02	2.33±0.60
283.6+25.3	0.1027 (4)	70 000±4000	4000.00±300.0	−11.99±0.02	25.24±4.80
286.8−29.5	0.0520[a]	130 700:	4680.70±1000.0	−12.14±0.10	8.28±3.0
291.4+19.2	0.1488[a]	190 000:	6200±1000.0	−12.30±0.02	9.12±1.80

[a] Interstellar reddening calculated from the Galactic dust extinction from Schlafly & Finkbeiner (2011) unless otherwise indicated in References. See `https://irsa.ipac.caltech.edu/applications/DUST/`.
Refs. (1) Douchin et al. (2015), (2) Acker et al. (1992b), (3) De Marco et al. (2013), (4) Ciardullo et al. (1999).
Note: Errors were not reported for $T_{\rm hot} > 100\,000$ K, marked with ":", as these $T_{\rm eff}$ are very uncertain (see Section 3.4.1).

PN G117.5+18.9, PN G211.4+17.4, and PN G286−29.5 have large errors in their solution. This errors could be related to a degeneracy of parameters, including extinction.

3.5.2 PNe with Gaia distances

In this section, we analyzed the ten PNe that have a reliable Gaia DR2 distance from the work of González-Santamaría et al. (2019). Four of the PNe presented here resulted in a binary system (40%). By using the Gaia distance, we can infer the stellar parameters of the CSPNe using the results obtained for $\log(\alpha)$ and β in the fitting process. This is, for the stellar radius of the hot star, we used

$$R_{\rm hot} = 10^{\log(\alpha)} D \tag{3.11}$$

where D is the distance to the CSPN, whereas the luminosity for the hot star is

$$L_{\rm hot} = 4\pi\sigma_{\rm SB} R_{\rm hot}^2 T_{\rm hot}^4 \tag{3.12}$$

TABLE 3.4— Results of the fitting process for PNe with reliable Gaia DR2 distances.

PNG	$E(B-V)$	$T_{\rm hot}$	$T_{\rm cool}$	$R_{\rm hot}$	$R_{\rm cool}$	D	$L_{\rm hot}$	$L_{\rm cool}$
	(mag)	(10^3 K)		($R_\odot$)		(pc)	($L_\odot$)	
047.0+42.4	0.0800[a]	62.3±3.5		0.0671±0.0007		984±6	60.02±6.8	
059.7−18.7	0.0652[a]	77.5±14.0		0.0685±0.0007		1395±15	152.35±50.0	
077.6+14.7	0.0589[a]	113.2:		0.0319±0.0023		1635±13	151.20±40.0	
104.2−29.6	0.0835[a]	106.0:		0.0315±0.0029		808±8	112.87±30.0	
144.5+06.5[b]	0.5247[a]	45.5±2.5	8.2±0.1	0.3084±0.0138	1.4434±0.2204	1679±74	368.44±36.9	89.74±4.5
164.8+31.1	0.0100[a]	88.0:	<3000	0.0256		979.2±97	40±30.0	
205.1+14.2	0.0419 (1)	45.5±6.0		0.0331±0.0016		530.6±24	4.23±1.3	
217.1+14.7	0.0279[a]	102.9:		0.0146±0.0015		691.2±69	21.66±6.5	
219.1+31.2	0.0100 (2)	40.0±2.0	2.9±0.2	0.0398±0.0019	0.3489±0.0321	504±23	3.65±0.8	0.008±0.002
326.7+42.2	0.1000[a]	30.0:	5.0±0.1	0.0437±0.0100	1.04±0.5	1867±429	1.39±0.06	0.61±0.7

[a] Interstellar reddening calculated from the distance modulus method as described by Green et al. (2018).
[b] Pulsating DA WD (Hermes et al., 2017).
Refs. (1) Frew et al. (2013) - (2) Douchin et al. (2015).
Note: Errors were not reported for $T_{\rm hot} > 100\,000$ K or for those marked with ":", as these $T_{\rm eff}$ are very uncertain (see Section 3.4.1).

where $\sigma_{\rm SB}$ is the Stefan-Boltzmann constant (5.6704×10^{-5} erg cm^{-2} s^{-1} K^{-4}). Similarly, we derived the radius of the companion star with

$$R_{\rm cool} = \beta R_{\rm hot}, \tag{3.13}$$

and luminosity by using Equation 3.12. In this case, errors were propagated as

$$\Delta f = \sqrt{\Sigma \frac{\partial f}{\partial x_i} \Delta x_i}. \tag{3.14}$$

Table 3.4 shows the stellar parameters obtained from the analysis of PNe with reliable Gaia DR2 distances. In this case, only three binary CSPNe resulted from the fitting process, as determined by the value of β ratio. We can infer that the PN G144.5+06.5, PN G219.1+31.2, and PN G326.7+42.2 have an A-type star companion, M-type star companion, and G-type star companion, respectively, as judged by the derived temperature and stellar radius. Furthermore, Table 3.4 also shows a probable binary CSPN in PN G164.8+31.1 that contains an M-type star companion. However, the large errors estimated in the fitted values, and the temperature obtained, is out of the model parameters used in the fitting process. It is important to note that errors estimated for the stellar values are mostly dependent of the errors reported in Gaia DR2 distances.

3.6 Individual objects

In this section, we will discuss on individual binary CSPNe resulted from our fitting method. A total of 12 PNe resulted in binary CSPNe detection out of

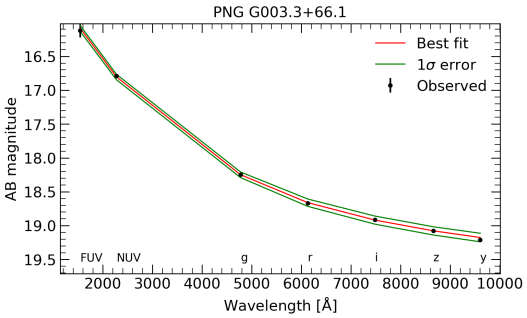

FIGURE 3.8— SED fit of the GALEX FUV, NUV + PS1 *g, r, i, z, y* photometry of the PN G003.3−66.1. Best fit and 1σ error are shown as red and green lines, respectively, and the black points are the observed photometry with error bars.

22 PNe analyzed. We exclude from this analysis the PN G144.5+06.5, as the observed GALEX photometry show some anomalies in the FUV band probably because of the CS is a pulsating DA WD (Hermes et al., 2017).

3.6.1 PN G003.3+66.1

The PN SkAc 1 (PN G003.3+66.1) was classified as binary CSPN by Douchin et al. (2015) using the IR excess method. Douchin et al. (2015) derived an $T_{\rm hot}$ ∼35 000 K for the ionizing star employing the Zanstra method with their derived V magnitude and the H_α flux from Frew et al. (2013) and detected an M4V companion with low confidence in I band, but confirmed detection using J band. In this work, we derived $T_{\rm hot}$ = 100 000 K, much hotter than obtained by Douchin et al. (2015), and $T_{\rm cool}$=4245 K for the companion (Figure 3.8). If we assume that the companion is on the main sequence, because it has to be in an earlier evolutionary stage that the ionizing star, it will be a M0V star. Despite that SDSS magnitudes measured in Douchin et al. (2015) and in this work are similar (withing the estimated errors), differences on the determination of the stellar parameters of both stars could be arising due to the fact that we are using UV photometry, which is more sensitive to the flux of the ionizing star.

In addition, PN SkAc 1 is an extended low-surface brightness PN detected

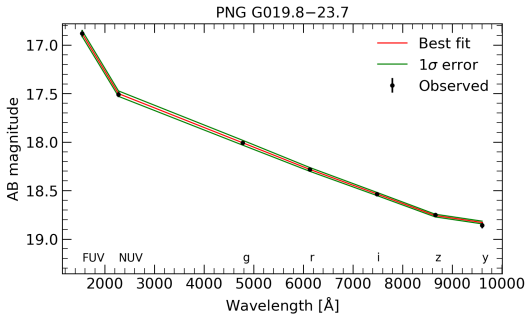

FIGURE 3.9— SED fit of the GALEX FUV, NUV + PS1 *g, r, i, z, y* photometry of the PN G019.8−23.7. Best fit and 1σ error are shown as red and green lines, respectively, and the black points are the observed photometry with error bars.

in GALEX, optical photometric bands, and in H_α flux (see Figure 10 of Douchin et al., 2015). Simulations of dynamical evolution of the circumstellar material around PNe demonstrated that nebular shells accelerates during their evolution (Villaver et al., 2002) and that nebular gas tent to dim as they get older. Hence, $T_{\rm hot}$ ∼35 000 K would rather indicate that the PN is young which is incompatible with H_α and optical imaging observations (e.g., Frew et al., 2013; Douchin et al., 2015, respectively).

3.6.2 PN G019.8−23.7

The Abell 66 (PN G019.8−23.7) is a round, resolved, and faint PN, ideal for the analysis with UV and optical bands. As a first iteration, using the reddening value from GALEX database ($E(B-V)$=0.1625; Schlegel et al., 1998), we derived $T_{\rm hot}$=74 531 ± 14 000 K for the ionizing star and $T_{\rm cool}$=8850 ± 50 K for the companion (Figure 3.9). The effective temperature for both stars and the radius ratio shown in Table 3.3, assuming an A2V companion, yield values for the stellar radius of 1.78 $R_\odot$ and 0.26 $_\odot$ for the companion star and the ionizing star, respectively.

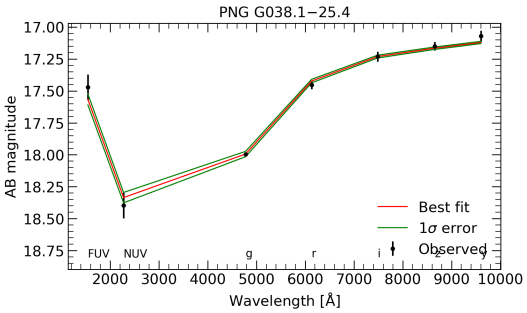

FIGURE 3.10— SED fit of the GALEX FUV, NUV + PS1 g, r, i, z, y photometry of the PN G038.1−25.4. Best fit and 1σ error are shown as red and green lines, respectively, and the black points are the observed photometry with error bars.

3.6.3 PN G038.1−25.4

Abell 70 (PN G038.1−25.4) is a PN known for its diamond ring appearance due to the superposition with a background galaxy. The CSPN is presumed Ba star binary system (Miszalski et al., 2012), where the companion es presumed to be a giant or subgiant star (the 2MASS $J - K = 0.70$ color for the CSPN suggest the presence of a G8IV-V companion; Miszalski et al., 2012).

Abell 70 is a Type I elliptical PN ionized by a star with $T_{\rm hot} = 190\,000$ K (Figure 3.10), as derived here (similar to that compiled in Stanghellini et al., 2006a). Stellar parameters derived in this work for the companion star also suggest an spectral type G8V due the $T_{\rm cool}$=4900±30 K, which is a typical value for this kind of stars. Assuming a stellar radius of $R = 0.9$ R$_\odot$ for the companion star, which is typical for the assumed spectral type, the ionizing star would have a radius of $R = 0.01$ $_\odot$.

3.6.4 PN G144.3−15.5

Abell 4 (PN G144.3−15.5) is a resolved PN with a small diameter (18 ″ as measured in GALEX images) and according to our models, the CSPN is a binary system composed by a ionizing star with an $T_{\rm hot}$=190 000 K and a presumably main-sequence K8-0V star with an $T_{\rm cool}$=4068±50 K (Figure 3.11). Typically,

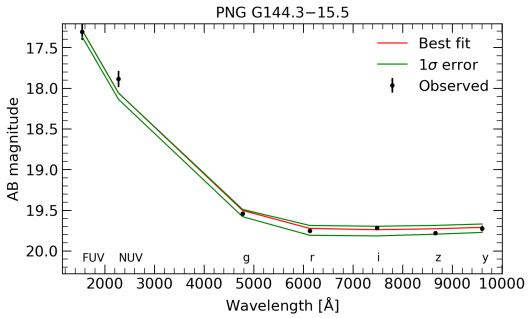

FIGURE 3.11— SED fit of the GALEX FUV, NUV + PS1 *g, r, i, z, y* photometry of the PN G144.3−15.5. Best fit and 1σ error are shown as red and green lines, respectively, and the black points are the observed photometry with error bars.

the radius of a K8-0V star is in the range of $R = 0.7 - 0.8$ R$_\odot$ yielding a stellar radius for the ionizing star of $R \simeq 0.03$ R$_\odot$.

With information of the the stellar radius of both stars, is possible to estimate the distance to the PN using the Equation 3.11, yielding roughly $d = 6$ kpc. Abell 4 is apparently an old PN due to the effective temperature and stellar radius of the ionizing star obtained with the MCMC method, and its apparent small diameter would be explained by the estimated distance.

3.6.5 PN G153.7+22.8

Abell 16 (PN G153.7+22.8) is a round PN with a very low surface brightness with a diameter of ∼25 ″. The CSPN is a binary system where we derived $T_{\rm hot}$=45 660±3800 K for the ionizing star and $T_{\rm cool}$=3800±400 K for the companion star (Figure 3.12); assuming, again, that the companion is a main-sequence star (see Section 3.6.1) it would be a M0V star. De Marco et al. (2013) obtained similar results for this PN by using the IR excess method.

Assuming a typical stellar radius for the M0V companion star $R = 0.62$ R$_\odot$ we roughly estimate a value for the stellar radius of the ionizing star $R = 0.1$ R$_\odot$ and a distance to the PN of $d = 5$ kpc, twice the value reported in De Marco et al. (2013, and references therein).

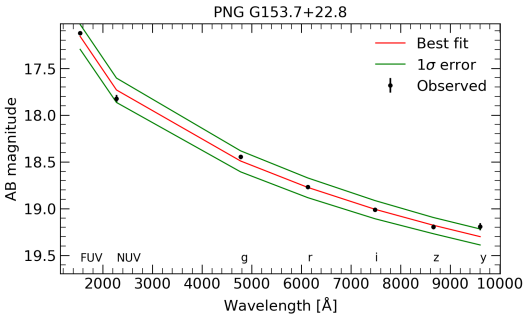

FIGURE 3.12— SED fit of the GALEX FUV, NUV + PS1 *g, r, i, z, y* photometry of the PN G153.7+22.8. Best fit and 1σ error are shown as red and green lines, respectively, and the black points are the observed photometry with error bars.

3.6.6 PN G171.3−25.8

The PN Ba 1 (PN G171.3−25.8) is a round, resolved, and faint PN, ideal for the analysis with UV and optical bands. Using the reddening value from GALEX database ($E(B-V)$=0.1; Schlegel et al., 1998), we derived $T_{\rm hot}$=30 000±100 K for the ionizing and $T_{\rm cool}$=8000 ± 300 K for the companion star (Figure 3.13). If we assume that the companion star is in the main-sequence, as similarly in Section 3.6.1, the spectral type is A5V star and its stellar radius would be $R \simeq$1.78 R$_\odot$ resulting in a ionizing star with a radius of $R \simeq$0.24 R$_\odot$.

This study reveals that Ba 1 is an apparently young PN with an unusually faint envelope. The presence of a binary companion and the fact that Ba 1 have low and extended surface brightness could be an indication that the system passed through the CE-phase, and expelled the outer layers faster than single star evolutionary models predictions, reaching enough effective temperature to ionize the PN.

3.6.7 PN G270.1+24.8

The PN K 1-28 (PN G270.1+24.8) is an elliptical, resolved, and faint PN, ideal for the analysis with UV and optical bands. Using the reddening value

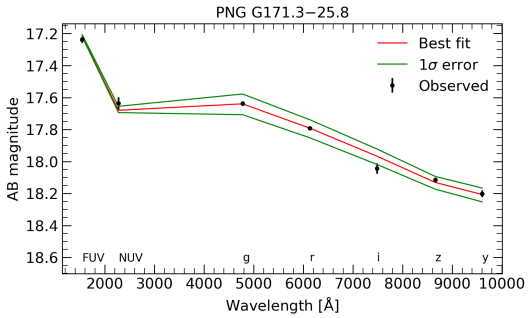

FIGURE 3.13— SED fit of the GALEX FUV, NUV + PS1 *g, r, i, z, y* photometry of the PN G171.3−25.8. Best fit and 1σ error are shown as red and green lines, respectively, and the black points are the observed photometry with error bars.

from GALEX database ($E(B-V)$=0.0454; Schlegel et al., 1998), we derived $T_{\rm hot}$=81 642 ± 15 000 K for the ionizing star and $T_{\rm cool}$=4000 ± 700 K for the companion star (Figure 3.14). If we assume that the companion star is in the main-sequence, as it must be the youngest star of the system, the spectral type is K2-0V with a radius of R ≃0.7 $R_\odot$. This implies that the radius of the ionizing star is R ≃0.3 $R_\odot$. The distance estimated wit this method is roughly d = 8.3 kpc.

3.6.8 PN G283.6+25.3

The PN K 1-22 (PN G283.6+25.3) is believed to be the twin of the Owl nebula because of its appearance. PN K 1-22 has a very wide companion with an orbit of the order of 500 AU (Ciardullo et al., 1999). Chu et al. (2011) showed that the IR excess found in their work for K 1-22 is due to a superposition of the photospheric emission of the CSPN and a red companion as well as dust component. In this work we confirmed the presence of a companion star with $T_{\rm cool}$=4000±300 K whereas the ionizing star have $T_{\rm hot}$ ≥70 000±4000 K.

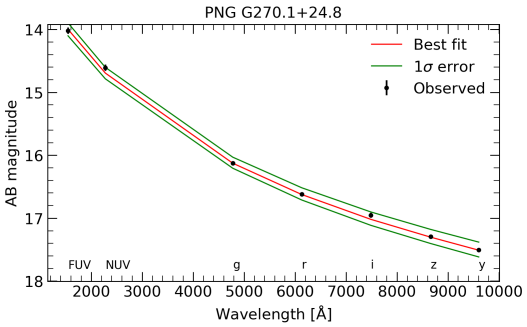

FIGURE 3.14— SED fit of the GALEX FUV, NUV + PS1 *g*, *r*, *i*, *z*, *y* photometry of the PN G270.1+24.8. Best fit and 1σ error are shown as red and green lines, respectively, and the black points are the observed photometry with error bars.

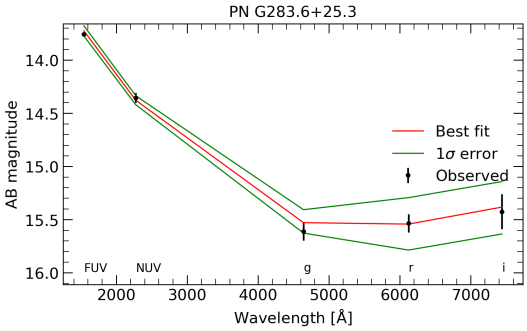

FIGURE 3.15— SED fit of the GALEX FUV, NUV + PS1 *g*, *r*, *i*, *z*, *y* photometry of the PN G283.6+25.3. Best fit and 1σ error are shown as red and green lines, respectively, and the black points are the observed photometry with error bars.

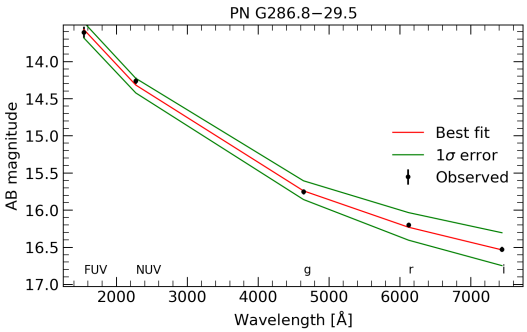

FIGURE 3.16— SED fit of the GALEX FUV, NUV + PS1 *g, r, i, z, y* photometry of the PN G286.8−29.5. Best fit and 1σ error are shown as red and green lines, respectively, and the black points are the observed photometry with error bars.

3.6.9 PN G286.8−29.5 and PN G291.4+19.2

The PN K 1-27 (PN G286.8−29.5) belong to an exotic group of He-dominated stars. The spectroscopic class is defined by almost pure He II absorption line spectrum in the optical wavelengths (Rauch et al., 1998). Reindl et al. (2014) made a detailed spectroscopic analysis based on optical and UV spectra and derive stellar parameters and distances. $T_{\rm hot} = 135\,000 \pm 5000$ K found for the ionizing star in Reindl et al. (2014) is very similar to that obtained by us of$T_{\rm hot} = 130\,700$ K (see Figure 3.16).

None of the single-star formation channels up to date seems convincing for the O(He) stars, and binary formation scenarios are becoming interesting. In this work we used an MCMC method to fit the SED of the PN from UV-optical data and found that the CSPN of K 1-27 is a binary system. We derived the stellar effective temperatures of both ionizing and companion star of $T_{\rm hot} = 130\,700$ K and $T_{\rm cool} = 4680 \pm 1000$ K, respectively. Using the distance calculated by Reindl et al. (2014) of $d = 2.0 \pm^{0.63}_{-0.84}$ kpc, we obtained a stellar radius for the ionizing star of $R = 0.064 \pm^{0.023}_{-0.031}$ $R_\odot$. It was also possible to obtain the stellar radius for the companion star of $R = 0.53 \pm 0.2$ $R_\odot$.

The PN LoTr 4 (PN G291.4+19.2) was also investigated by Reindl et al.

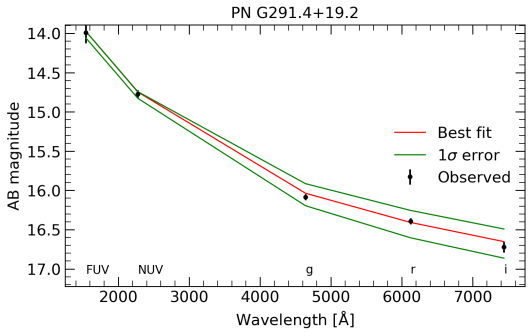

FIGURE 3.17— SED fit of the GALEX FUV, NUV + PS1 *g, r, i, z, y* photometry of the PN G291.4+19.2. Best fit and 1σ error are shown as red and green lines, respectively, and the black points are the observed photometry with error bars.

(2014). They found $T_{\rm hot} = 120\,000 \pm 12\,000$ K, very different to the temperature we obtained from the MCMC method of $T_{\rm hot} = 190\,808$ K. Differences could be arise because of the reddening value, $E(B-V)$, used. However, the $T_{\rm hot}$ estimated with MCMC method is very similar with either using $E(B-V) = 0.2$, as derived by Reindl et al. (2014), or $E(B-V) = 0.1488$, obtained from the Schlafly & Finkbeiner (2011) extinction map. However, it is clear from the Figure 3.18 that the MCMC method fits the SED accurately.

3.6.10 PN G219.1+31.2

Abell 31 (PN G219.1+31.2) is an old and extended PN with very low surface brightness. The CSPN was investigated by Douchin et al. (2015) searching for a binary system using the IR excess method. They found that the CSPN is composed by the ionizing star and a companion of M4 spectral type. The reported $T_{\rm hot} = 114\,024 \pm 20\,000$ K for the ionizing star is different to that found in this work ($T_{\rm hot} = 40\,000 \pm 5000$ K; see Figure 3.18). Such large differences could arise because we used the reported GALEX $E(B-V) = 0.04$, while Douchin et al. (2015) estimated a lower reddening of $E(B-V) = 0.01$. We input both ($E(B-V)$ values in the MCMC method and the model only converged

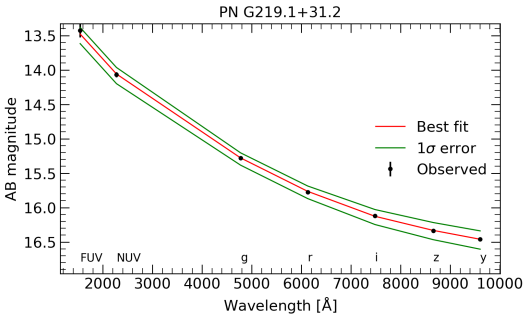

FIGURE 3.18— SED fit of the GALEX FUV, NUV + PS1 *g, r, i, z, y* photometry of the PN G219.1+31.2. Best fit and 1σ error are shown as red and green lines, respectively, and the black points are the observed photometry with error bars.

with the value reported in the GALEX database. We derived $T_{\rm cool}$=2700±200 K for the companion, which is presumed to be M4 spectral type as suggested by Douchin et al. (2015).

3.6.11 PN G326.7+42.2

From Figrue **??** the SED of IC 972 (PN G326.7+42.2) clearly shows a flux excess in the optical compared with the GALEX UV colors. Even at $E(B-V)$=0 or at higher amounts of reddening such flux excess will still be seen. However, it is difficult to estimate accurate values for the $T_{\rm eff}$ of both stars because, although the MCMC method converges at the lower limit of $T_{\rm hot}$, there is evidence that $T_{\rm hot} \geq$45 000 K due to the presence of He II emission lines (Phillips, 2003).

In this particular case, where the SED of the companion star is clearly visible through an optical flux excess, we examine the PS1 MDS multi-epoch photometry from the catalog GPNSPcat (see Chapter 2.5). The CSPN clearly shows a variation with an amplitude of the order of 0.2 mag in the $i_{\rm PS1}$ (see Figure 3.20). This makes difficult the fitting process and any value derived from the MCMC method would be unrealistic. However, the method clearly proves the presence of a companion star.

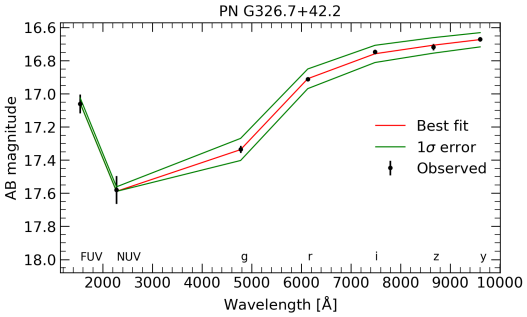

FIGURE 3.19— SED fit of the GALEX FUV, NUV + PS1 g, r, i, z, y photometry of the PN G326.7+42.2. Best fit and 1σ error are shown as red and green lines, respectively, and the black points are the observed CSPN photometry with error bars.

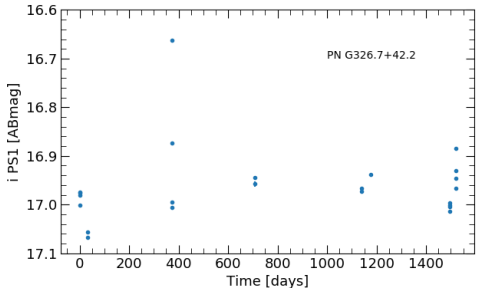

FIGURE 3.20— Photometric variability of the PN G326.7+42.2 in the $i_{\rm PS1}$ band.

3.7 Summary

In this chapter, we have analyzed the SED of 22 PNe resolved in GALEX Imaging, so that the CS flux can be measured. We developed a new method, based on the so-called MCMC method, to identify binary CS using single/mean epoch photometry from the UV to the broad optical bands.

We have constructed model magnitude tables in the UV-optical broad bands for a wide range of parameters to be used by the MCMC algorithm. The fitting process was carried out by using the color index of the observations to obtain the stellar temperatures and the ratio of the radii of the stars. This is useful because it is independent of the distance to the PN. After the first iteration, a second one was needed to find the scaling factor, the ratio of the central star and distance, by using the magnitude of each value of the SED.

Note that with this analysis made with UV and optical bands is possible to identify binary systems composed by a hot-WD and a cooler companion (Bianchi & Shiao, 2020). After dividing the sample of planetary nebulae in two groups, we have found a binary fraction of 85% (10 binary CSPNe out of 12 analyzed) for the first group (PNe with $|b| > 15$) and 40% (4 binary CSPNe out of 10 analyzed) for the second group (PNe with reliable Gaia DR2 distance). Hence, we found a global binary fraction of 63%, similar to that obtained in previous works (e.g., De Marco et al., 2013; Douchin et al., 2015; Barker et al., 2018).

Out of the 14 binary CSPNe, seven are new binary CSPNe candidates: PN G019.8−23.7, PN G144.3−15.5, PN G171.3−25.8, PN G270.1+24.8, PN G291.4+19.2, PN G144.5+06.5, and PN G326.7+42.2.

This work also demonstrated the potential of GALEX matched to optical surveys to study the PNe.

4

Grid of model spectral energy distributions of planetary nebulae in UV-optical range

No one has a perfect life. Everybody has something that he wishes was not the way it is.
−Stan Lee

In this chapter, we characterize the position of single planetary nebula (PN) and PNe with binary central star (CS) in color-color diagrams. We constructed a grid of synthetic spectral energy distributions (SEDs) of PNe using the photoionization code CLOUDY, and computed synthetic magnitudes in UV GALEX and optical SDSS *u g r i z*, PanSTARRS *g r i z y*, Gaia DR2 *Gbp G Brp*, and Jhonson *U B V R I* bands. We explore, in color space, how the position of the PNe observed compares with the PNe model colors as well as how they can be distinguished from model colors for other astrophysical objects such as main-sequence, supergiant or white-dwarf stars. We computed synthetic colors of PNe with both a single CS, and a binary CS including a cool stellar companion to each model SED to identify PNe with binary CS. We find that GALEX FUV−NUV versus SDSS $r-i$ color-color diagram is the best one for cleanly separating PNe and PNe with binary CS from other astrophysical objects.

4.1 Introduction

MOST of the astronomical surveys dedicated to finding binary CSPNe (see Chapter 1) are based on observations or follow-ups of resolved PNe (where the surface brightness of the PNe envelope is faint; see Chapter 1).

In Chapter 3, we have analyzed PNe resolved with GALEX. However, most of our sample of Galactic PNe are unresolved and is very difficult to isolate the CS flux. To analyze unresolved PNe, we computed a set of synthetic SEDs to determine GALEX UV and SDSS and PanSTARRS optical color-color spaces that can successfully identify PNe among other sources.

Here, we take advantage of the GALEX UV bands matched with optical SDSS and PanSTARRS bands to analyze the loci of unresolved PNe on the color-color diagrams using a different combination of colors. The characterization was carried out by creating synthetic PN magnitudes as a function of different stages of their CS evolution according to theoretical post-AGB evolutionary tracks, specifically those from Miller Bertolami (2016). Although this work is focused on the GALEX UV and SDSS and PanSTARRS optical bands, Gaia DR2, Jhonson and 2MASS broadbands are available in the online model grid[1].

In Section 4.2.1, we describe the photoionization code CLOUDY and its input/output parameters, and how we constructed the models. In Section 4.2.2 and 4.2.3, we present the results obtained for line emissivities and emergent spectra, respectively. Finally, we analyze the position of the synthetic models of unresolved PNe in color-color diagrams in Section 4.4.

4.2 Grid of PNe photoionization models computed with CLOUDY

In this section we describe the photoionization code used to compute the SEDs of PNe and the construction of the model grid.

4.2.1 Photionization code and model parameters

The model spectra were computed with the photoionization code CLOUDY, version c17.01 (Ferland et al., 2017), using the PyCloudy (Morisset, 2013a) python package. CLOUDY is a non-local thermodynamic equilibrium (non-LTE) spectral synthesis code and plasma simulation code designed to simulate astrophysical environments within clouds (e. g. PN, AGNs, and H II regions)

[1] http://dolomiti.pha.jhu.edu/PNgrid/

and predict their spectra. For a PN, CLOUDY takes the input of the central star spectrum (blackbody or a user-defined ionizing source) and the physical parameters of the PN (e.g., hydrogen density and chemical abundances of the nebular gas, distance of the ionizing source to the internal shells, geometry, and dust content) and computes the thermal, ionization, and chemical structure of the PN, returning the emerging spectrum.

The output of each model contains, beyond of physical and nebular parameters, and atomic properties, the information of incident radiation field (from the ionizing CS), the diffuse radiation (which includes emission lines), the transmitted incident continuum, and the total transmitted continuum (which is the sum of the transmitted incident continuum and nebular gas emitted continuum and lines; takin into account, e.g., the free-free, free-bound, and two-photon radiation), as well as the requested line emission per unit volume.

Our goal is to obtain model magnitudes that can describe the PN based on its different stratification components. We use an initial set of parameters that cover the ranges of known PN samples that we will describe in this section.

As stated before, CLOUDY requires two sets of input parameters: those for the ionizing source and those for the nebula. The ionizing source input parameters are the input SED of the CS, which depends on the stellar luminosity, $\log(L_*/L_\odot)$, effective temperature, $T_{\rm eff}$, gravity, $\log(g)$, and metallicity. The combination of these parameters were chosen according to the theoretical evolutionary post-AGB models of Miller Bertolami (2016), as shown in Figure 4.1 and Figure 4.2 for solar metallicity (z=0.01). Based on studies of CSPN masses (e.g., Stasińska et al., 1997; Moreno-Ibáñez et al., 2016), we begin by exploring CSPNe with a low and high final-mass of $M_* = 0.616{\rm M}_\odot$ and $M_* = 0.532{\rm M}_\odot$, respectively, for four CSPN $T_{\rm eff}$ (Table 4.1). Such final masses correspond to progenitor masses of 1 and 2.5 $M_\odot$, respectively. The $\log(L_*/L_\odot)$ of each CS was chosen according to its position in the HR diagram (Fig. 4.1), whereas $\log(g)$ has been selected based on the mass, luminosity, and $T_{\rm eff}$ of the CSPN according to the position in the $\log(T_{\rm eff}) - \log(L/L_\odot)$ plane (Fig. 4.2). For the input SEDs we used the solar composition H-He non-LTE atmosphere models, computed by Bianchi et al. (2007) using the TLUSTY code (Hubeny, 1988), which cover the range of $T_{\rm eff}$ from 30 000 K to 110 000 K, and $\log(g)$ from 4.0 to 9.0 dex. For higher $T_{\rm eff}$ we used the state-of-the-art solar composition H-Ni non-LTE Rauch atmosphere models (Rauch, 2003) which cover the range of $T_{\rm eff}$ from 50 000 K to 190 000 K and $\log(g)$ from 5.0 to 8.0. The wavelength range of the Rauch models is $4 - 2000$ Å and an extrapolation to lower energies using a Rayleigh-Jeans slope was done (see Hazy 1 of CLOUDY documentation), while the TLUSTY models cover $114 - 25\,000$ Å. Taking this into account, we found that the difference in the modeled broadband magnitudes between using a Rauch

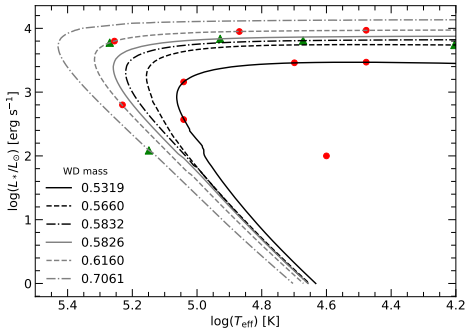

FIGURE 4.1— HR diagram showing the location of the modeled CSPNe (red dots) in the $\log(T_{\rm eff}) - \log(L/L_{\odot})$ plane. The evolutionary tracks of Miller Bertolami (2016) are shown for different WD masses. Up-sided triangles in the plots sets a 1000 yr mark for their age; so that more massive CS reach faster the WD stage.

or a TLUSTY model as the CSPN in the shared range of stellar parameters ($50\,000\,{\rm K}<T_{\rm eff}<110\,000\,{\rm K}$ and $5.0\ dex < \log(g) < 8.0\ dex$) was negligible.

The assumptions for the nebular parameters are the following:

- The nebula is spherically symmetric (Figure 4.3).
- The inner radius of the nebula ($R_{\rm in}$; the distance from the CS to the inner layers of the shell) was fixed to a value in the range 5.0×10^{16}–1.3×10^{18} cm. These values were obtained by comparing results of photoionization models fitted to observed PNe parameters (e.g., van Hoof & van de Steene, 1999; Bohigas, 2008; Barría & Kimeswenger, 2018), and by comparing sizes from morpho-kinematics studies (e.g., Gómez-Muñoz et al., 2015; Sabin et al., 2017; Ramos-Larios et al., 2018). Four $R_{\rm in}$ values were chosen to span the range of observed radius taking into account that the model colors do not change significantly in the range of $(1-0.2)R_{\rm in} < R_{\rm in} < (1+0.2)R_{\rm in}$ for each set of model parameters, although the flux does change.
- The density ($n_{\rm H}$) is constant inside the Strömgren radius (the radius at which the ionizing photons emitted by the CS balances the total number of

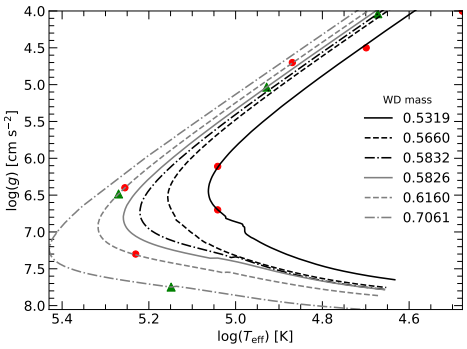

FIGURE 4.2— Same as Fig. 4.1 but in the $\log(T_{\rm eff}) - \log(g)$ plane.

TABLE 4.1— Input parameters for the grid of photoionization models.

Model	CS parameters			PN parameters	
	$T_{\rm eff}$ (10^4K)	$\log(g)$ (cm s^{-1})	$\log(L/L_\odot)$ (erg s^{-1})	$\log(n_{\rm H})$ (cm^{-3})	$R_{\rm in}$ (10^{17}cm)
$M = 0.616$ R$_\odot$					
cA_t3.0_l3.97_g4.00_nh4.30_r16.94	3.0	4.00	3.97	4.30	0.88
cA_t7.4_l3.95_g4.70_nh3.80_r17.00	7.4	4.70	3.95	3.80	1.00
cA_t18.0_l3.80_g6.40_nh3.30_r17.48	18.0	6.40	3.80	3.30	3.02
cA_t17.0_l2.80_g7.30_nh2.80_r17.71	17.0	7.30	2.80	2.80	5.11
$M = 0.532$ R$_\odot$					
cA_t3.0_l3.47_g4.00_nh4.30_r16.94	3.0	4.00	3.47	4.30	0.88
cA_t5.0_l3.46_g4.50_nh3.80_r17.00	5.0	4.50	3.46	3.80	1.00
cA_t11.0_l3.16_g6.11_nh3.30_r17.48	11.0	6.11	3.16	3.30	3.02
cA_t11.0_l2.57_g6.70_nh2.80_r17.71	11.0	6.70	2.57	2.80	5.11

recombination to excited levels) and decreases as $1/r^2$ outside it. That is, the photoionization will cause the gas to expand. This will be easiest for the gas inside the inner rim of the (previous) AGB shell as there is no gas further inward that would stop it. The deeper you get into the AGB shell, the more material there that will slow the expansion. So the innermost part of the AGB shell that has the highest density will expand the most, while the lower density material further out will expand less. Hence, the density in the ionized part of the nebula will be roughly constant, while the neutral part will decay as $1/r^2$ law like on the AGB. The Strömgren radius,$R_{\rm S}$, is calculated as follows:

$$R_{\rm s}^3 = \frac{3Q(H)}{4\pi n_{\rm H}^2 \alpha_\beta} - R_{\rm in}^3 \tag{4.1}$$

where Q(H) is the total number of ionizing photons, α_β is the Case B recombination coefficient, and $R_{\rm in}$ is the inner radius of the PN (distance from the central star to the nebular gas). Note that $R_{\rm s}$ is not strictly the outer radius of the PN, $R_{\rm out}$. The diffuse radiation field becomes important in the outer regions and the transition from ionized to neutral hydrogen is sharp, causing that $R_{\rm out}$ to be larger than $R_{\rm s}$ by a small amounts. The values of the density ($n_{\rm H}$) used are listed in Table 4.1. These values were chosen in the range $2.5 < \log(n_{\rm H}) < 4.8$, as reported in the literature (e.g., Stanghellini & Kaler, 1989; Zhang et al., 2004). The values were fixed according to the evolutionary state of the PN, this is, as the evolutionary age of the PN increase the $n_{\rm H}$ decrease and $R_{\rm in}$ increase.

- Abundances are set to the predefined PNe abundances included in CLOUDY, which are based on the works of Aller & Czyzak (1983) and Khromov (1989). The input abundances for the elements included in our model calculations, in units of $12 + \log(X/H)$, were $X_{\rm He} = 11.00$, $X_{\rm C} = 8.89$, $X_{\rm N} = 8.26$, $X_{\rm O} = 8.64$, $X_{\rm Ne} = 8.04$, $X_{\rm S} = 7.0$, $X_{\rm Cl} = 5.23$, and $X_{\rm Ar} = 6.43$.
- The dust grains considered in the models are a typical mixture of silicates and carbonates for the interstellar medium (ISM), as defined in the cloudy code, and also account for local absorption and scattering.
- The model fluxes in our grid are given for a distance of 1 kpc, for easy re-scaling to the observed objects.

The outer radius, $R_{\rm out}$, of the PN (Fig. 4.3) is not varied as an input parameter, but set equal to the ionization front of the H^+ region, beyond which

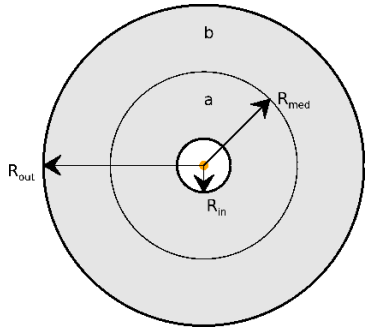

FIGURE 4.3— Sketch of the PN model used to explore the effect of the emission lines stratification for different shells.

the gas is no longer optically thick, as virtually all photons have been absorbed; the so-called ionization bounded (IB) PNe (e.g., NGC 7027; Rodríguez et al., 2009). In order to represent a PN that is optically thin to ionizing photons, often called density bounded (DB) PN (e.g. NGC 3242 and Hb 4; Barría & Kimeswenger, 2018; Rodríguez et al., 2009, , respectively), we trimmed the IB models to an outer radius, $R_{\rm med} < R_{\rm out}$.

To investigate the emission lines and nebular continuum emission at different radii inside the PN, we compare the resulting spectrum for the IB models (whole models) with the spectrum from the inner and outer shells. The inner shell, "a" (the DB PN) as indicated in the cartoon in Fig. 4.3, spans from $R_{\rm in}$ to $R_{\rm med}$, and the outer shell, "b", spans from $R_{\rm med}$ to $R_{\rm out}$ and its flux is defined as the difference between the IB and DB models. $R_{\rm med}$ is defined as the radius in which the ionization structure of the PN model is such that flux of C IV λ1549, seen prominent in the inner layers, becomes zero, or, if the PN results in a very thin shell, we chose $R_{\rm med} = R_{\rm in} + 0.6(R_{\rm out} - R_{\rm in})$ (see Subsect. 4.2.2). The emergent spectrum of shell "a" will contain most of the line emission from high ionization species, and shell "b" will contain most of the line emission from low ionization species.

Table 4.2 list the input parameters of the models used for CSPNe of final masses $0.616\,M_\odot$ and $0.532\,M_\odot$. Column 1 is the model name which fully describes the used input parameters as follows: `cA` indicates the case of density

law used, which in this models is constant (case A), `t00.0` indicates $T_{\rm eff}$ in units of 10^4 K (column 2), `l0.00` indicates $\log(L/L_{\odot})$ (column 3), `g0.00` indicates $\log(g)$ (column 4), `nh0.00` indicates $\log(n_{\rm H})$ (column 5), and `r00.00` indicates $\log(R_{\rm in})$ (column 6).

Caveats

The C/O ratio used in our PNe model spectra of 1.03, as predefined in the set of PNe abundances in CLOUDY, is different from those that correspond to the CS final masses of 0.532 and 0.616 $M_{\odot}$, with C/O=0.372 and C/O=2.48 (Miller Bertolami, 2016), respectively. For a CS final mass of 0.532 $M_{\odot}$, that corresponds to an initial mass of 1 $M_{\odot}$, the 3rd dredge-up is not efficient on the AGB phase and the CS final mass would be O-rich (see Table 2 from Miller Bertolami, 2016), while for a CS final mass of 0.616 $M_{\odot}$, that corresponds to an initial mass of 2.5 $M_{\odot}$, the 3rd dredge-up is very efficient on the AGB phase, transporting C to the stellar surface resulting in a C-rich CS final mass (see Table 2 from Miller Bertolami, 2016). These changes in C/O ratio may affect the C and O nebular emission lines resulted in our spectra model, and hence, changes in the modeled magnitudes are expected (e.g., C IV λ1549 and [O III] λ4959,5007 in GALEX FUV and SDSS r bands, respectively; see Subsect. 4.2.2).

The modeled PNe magnitudes could also be affected by the grains and dust used in this thesis; the default combination of silicates and carbonates included in CLOUDY – for the O-rich initial mass of 1 $M_{\odot}$, the dust would be mostly silicates, while for the C-rich initial mass of 2.5 $M_{\odot}$, the dust would be mostly carbonates.

This effects could be addressed in the future.

4.2.2 Line emissivities of principal ions

In this section we will describe the nebular emission (nebular continuum and line emission) obtained from the photoionization models that are likely affecting the UV and optical broad bands of GALEX and SDSS, respectively.

Figures from 4.4 to 4.7 show the emission lines as a function of the radius of the PN models. Most of the line emission of high ionization species (e.g., C IV λ5149 Å and C III] λ1909 Å) drop its emission when they reach a depth ($R_{\rm out} - R_{\rm in}$) close to ∼60% the size of the nebula, whereas the low ionization species (e.g., [O III] λ4959,5007 Å) are practically constant throughout the PN.

In the UV range, for $M_* = 0.616\,{\rm M}_{\odot}$ (Fig. 4.4), emission of C IV λ1549 is not present at $T_{\rm eff}$=30 000 K, while for $T_{\rm eff}\geq$50 000 K it may be present. In both hot-WD mass models, the emission of C IV λ1549 increases when the CS

reaches $T_{\rm eff}$=50 000 K, and then decreases at larger ages ($T_{\rm eff}$>110 000 K), and the density of the PN decreases due to the nebular expansion (increase of $R_{\rm in}$).

In the optical range, for both masses (Fig. 4.6 and 4.7), the emission of low ionization species, such as [N II] λ6548,6584 lines, increases with increasing radius. The emission increases more rapidly for low-density models than for the high-density models. An exception occurs for models with $T_{\rm eff}$=170 000 K and low density (bottom right panel of Fig. 4.6), since the emission line is decreasing as a function of the radius of the nebula. The [O III] λ4959,5007 emission lines are also constant on most of the models except for low density models where the emission lines rapidly decreases at ∼80% of $R_{\rm out}$ (bottom panels of Fig. 4.6 and 4.7). Models with the lower density (and higher $R_{\rm in}$) are also larger in size and in hydrogen mass (Hmass) as can be seen in column 4 of Table 4.2.

From the analysis of the UV and optical emission lines, we derived the best $R_{\rm med}$ value, shown from Fig. 4.4 to 4.7 as a vertical dashed line, to obtain DB models. The DB models were produced by reading the IB models from $R_{\rm in}$ to $R_{\rm med}$, whereas "b" models were produced by subtracting shell DB from the IB models.

The size of a PN will change over time, as it is getting older the nebular shell will expand and merge with the interstellar medium. As mentioned in Subsect. 2.3.2, the measured size and the morphology at different wavelengths of a PN depend on its ionization structure. As can be seen from Figs. 4.4–4.7, the ionization structure changes over time and it strongly depends of the emission line being measured. It is clear from the figures that the He II emission is stronger than other emission lines in the UV range, while H_α, [N II], and [O III] lines are the stronger emission lines in the optical range, which makes them suitable candidates for PN size measurements (e.g., Manchado, 2004). The real intensity of these emission lines will strongly depend on the nebular continuum (see Section 4.2.3).

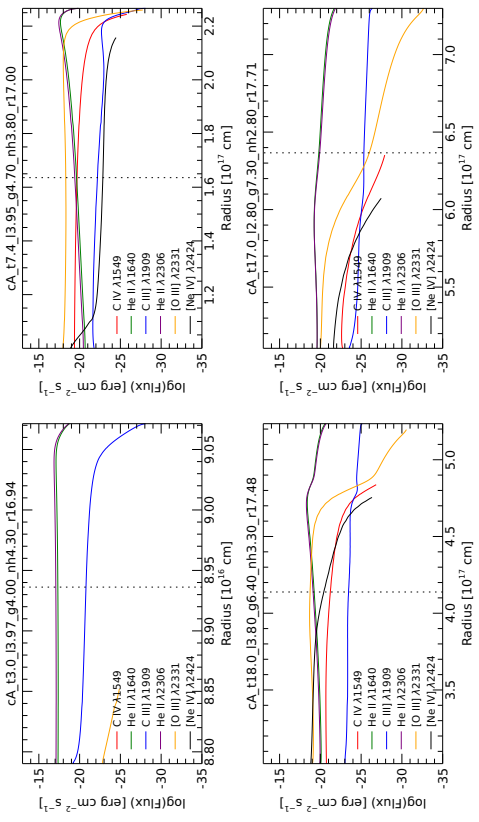

FIGURE 4.4— UV emission lines flux per unit volume as a function of the distance to the CS of the PN for a final mass of $M_* = 0.616 M_\odot$. The dotted line is the $R_{\rm med}$ defined according to the change of the ionization structure of the nebula (see text). The evolutionary state of the PN increases from left to right and from top to bottom.

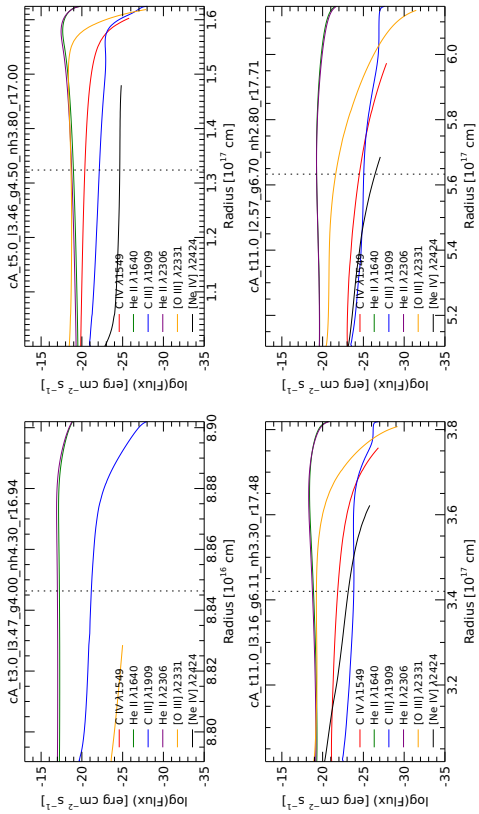

FIGURE 4.5— Same as Fig. 4.4 but for a mass of $M_* = 0.532 M_\odot$.

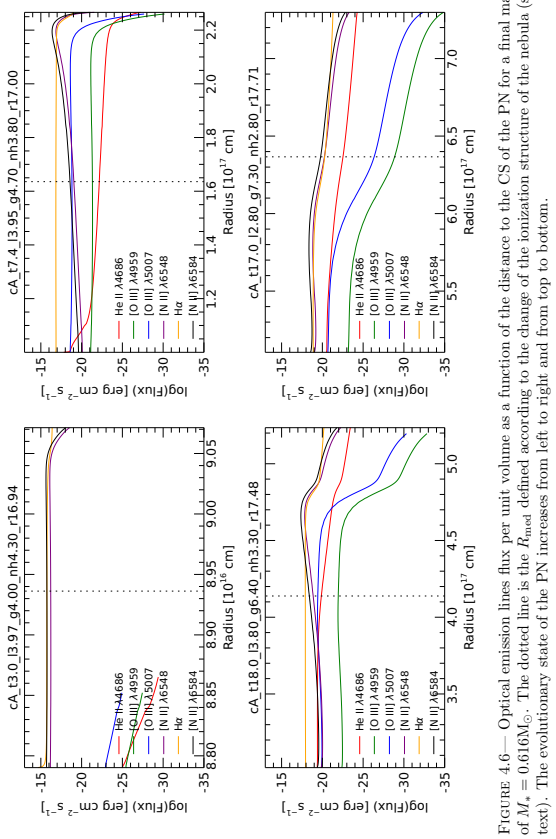

FIGURE 4.6— Optical emission lines flux per unit volume as a function of the distance to the CS of the PN for a final mass of $M_* = 0.616 M_\odot$. The dotted line is the $R_{\rm med}$ defined according to the change of the ionization structure of the nebula (see text). The evolutionary state of the PN increases from left to right and from top to bottom.

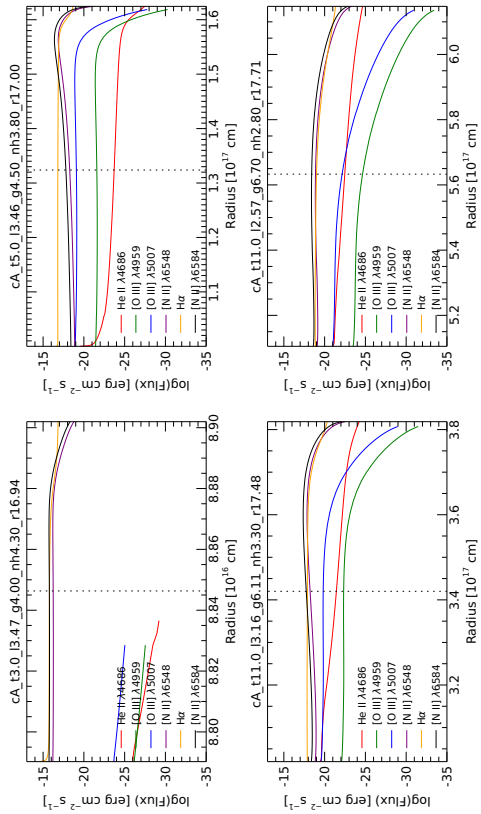

FIGURE 4.7— Same as Fig. 4.6 but for a mass of $M_* = 0.532 M_\odot$.

4.2.3 The PN model spectra computed with CLOUDY

Figures 4.8 and 4.9 show the UV emergent synthetic spectra from the PN models as well as the GALEX UV transmission curves[2]. In the range of low CS $T_{\rm eff}$ (top panels), the FUV band is dominated by the emission of the ionizing source, with no emission lines and weak nebular continuum for all models. In the NUV band all models contain strong emission lines of C III] λ1909, [O III] λ2331, and [O II] λ2470, with relatively strong contribution of nebular continuum emission. Also, as the PN evolutionary age increases, the CS's $T_{\rm eff}$ increases and the gas density $n_{\rm H}$ decreases, the contribution of emission lines in UV bands for the IB model and shell DB models becomes important, with the appearing of C IV λ1549 and He II λ1640 in FUV, and [Ne IV] λ2424 in NUV, as well as nebular continuum emission. In shell "b" (the outer shell), the emission lines in FUV are negligible and nebular continuum emission is the only nebular contribution to the total flux, whereas in NUV band, both emission lines and nebular continuum emission are important contributors to the flux. We measured the contribution of emission lines and nebular continuum emission to the ionizing source as the difference between the total emergent flux and the CS flux, integrating the GALEX FUV and NUV bands to this difference, yielding 2.80 ABmag and 4.1 ABmag, respectively, as measured in the IB model (shell "w") `cA_t17.0_l2.80_g7.30_nh2.80_r17.71`.

In addition to emission lines and nebular continuum emission, we also have to take into account the attenuation of the CS flux due to absorption and scattering opacity. If we increase $T_{\rm eff}$ and decrease $n_{\rm H}$, the attenuation of the CS is somewhat important. To quantify the effect of CS flux attenuation, we subtracted the attenuated CS flux from the unattenuated CS flux and integrated this difference in the GALEX FUV and NUV bands, both yielding −0.1 ABmag, as measured in the IB model `cA_t17.0_l2.80_g7.30_nh2.80_r17.71`.

In the optical range (see Figures 4.10 and 4.11) the models have a similar behavior. The nebular continuum and line emission increase increasing $T_{\rm eff}$. For $T_{\rm eff}\geq$50 000 K (top-right panel of Fig. 4.11), the nebular continuum emission is several orders of magnitude brighter than the CS flux (3.2 ABmag and 2.4 ABmag, for SDSS g and SDSS i, respectively, for the model `cA_t5.0_l3.46_g4.50_nh3.80_r17.00`).

Although shell "a" and "b" model fluxes vary from model to model, since they are dependent on the definition of $R_{\rm med}$, optical bands (SDSS bands in this case) are strongly affected by emission lines. In the u band the prominent emission lines are H_ϵ, H_ζ, and [O II] λ3726,3729, the g band is affected by

[2]GALEX UV transmission curves were obtained from the Spanish Virtual Observatory at `http://svo2.cab.inta-csic.es/theory/fps/`

TABLE 4.2— GALEX and SDSS model magnitudes for PN models in Table 4.1

Model	R_{in}	R_{out}	Hmass	FUV	NUV	u	g	r	i	z
	(10^{17}cm)		($M_\odot$)	(AB magnitude)						
IB models ("w" shell)										
cA_t3.0_l3.97_g4.00_nh4.30_r16.94	0.88	0.91	0.005	6.24	6.68	7.20	7.50	7.57	8.34	8.60
cA_t7.4_l3.95_g4.70_nh3.80_r17.00	1.00	2.27	0.237	8.18	7.95	7.13	5.49	6.30	7.62	7.44
cA_t18.0_l3.80_g6.40_nh3.30_r17.48	3.02	5.24	0.815	7.84	7.82	7.01	5.82	6.25	7.86	7.52
cA_t17.0_l2.80_g7.30_nh2.80_r17.71	5.11	7.30	0.525	10.54	10.09	8.63	8.68	7.81	10.04	9.83
cA_t3.0_l3.47_g4.00_nh4.30_r16.94	0.88	0.89	0.002	7.46	7.90	8.43	8.74	8.80	9.58	9.86
cA_t5.0_l3.46_g4.50_nh3.80_r17.00	1.00	1.62	0.073	8.61	8.71	8.14	7.03	7.36	8.75	8.51
cA_t11.0_l3.16_g6.11_nh3.30_r17.48	3.02	3.82	0.198	9.73	9.30	8.08	7.34	7.24	9.08	8.82
cA_t11.0_l2.57_g6.70_nh2.80_r17.71	5.11	6.15	0.221	11.14	10.68	9.11	9.55	8.24	10.54	10.38
DB models ("a" shell; R_{out}=R_{med})										
cA_t3.0_l3.97_g4.00_nh4.30_r16.94	0.88	0.89	0.002	6.23	6.67	7.22	7.52	7.76	8.37	8.65
cA_t7.4_l3.95_g4.70_nh3.80_r17.00	1.00	1.64	0.075	8.32	8.66	8.36	6.58	7.89	8.94	8.91
cA_t18.0_l3.80_g6.40_nh3.30_r17.48	3.02	4.14	0.305	7.95	8.32	8.12	6.41	7.61	8.72	8.22
cA_t17.0_l2.80_g7.30_nh2.80_r17.71	5.11	6.37	0.278	10.52	10.08	8.62	8.69	7.83	10.05	9.85
cA_t3.0_l3.47_g4.00_nh4.30_r16.94	0.88	0.89	0.001	7.46	7.90	8.45	8.75	8.97	9.61	9.90
cA_t5.0_l3.46_g4.50_nh3.80_r17.00	1.00	1.32	0.029	8.61	8.97	8.96	7.76	8.62	9.62	9.38
cA_t11.0_l3.16_g6.11_nh3.30_r17.48	3.02	3.42	0.088	10.10	9.97	9.13	7.66	8.45	9.81	9.35
cA_t11.0_l2.57_g6.70_nh2.80_r17.71	5.11	5.63	0.102	11.38	11.03	9.41	9.69	8.68	10.84	10.64
Shell "b" models ($R_{in} = R_{med}$)										
cA_t3.0_l3.97_g4.00_nh4.30_r16.94	0.89	0.91	0.003	6.25	6.68	7.24	7.54	7.81	8.39	8.68
cA_t7.4_l3.95_g4.70_nh3.80_r17.00	1.64	2.27	0.162	8.46	8.19	7.43	5.96	6.56	7.95	7.73
cA_t18.0_l3.80_g6.40_nh3.30_r17.48	4.14	5.24	0.510	9.93	8.84	7.49	6.76	6.61	8.52	8.32
cA_t17.0_l2.80_g7.30_nh2.80_r17.71	6.37	7.30	0.247	13.79	15.02	...	13.90	11.94	14.98	14.58
cA_t3.0_l3.47_g4.00_nh4.30_r16.94	0.89	0.89	0.001	7.47	7.91	8.48	8.78	9.09	9.64	9.94
cA_t5.0_l3.46_g4.50_nh3.80_r17.00	1.32	1.62	0.044	8.73	8.90	8.49	7.70	7.71	9.21	9.04
cA_t11.0_l3.16_g6.11_nh3.30_r17.48	3.42	3.82	0.110	10.43	9.96	8.57	8.83	7.67	9.83	9.84
cA_t11.0_l2.57_g6.70_nh2.80_r17.71	5.63	6.15	0.119	12.06	11.83	10.61	11.79	9.45	12.06	12.07

H_β and [O III] λ4959,5007 emission lines, the r band is affected by He I λ5876, [O I] λ6300, [S III] λ6312, [N II] λ5755,6548,6584, H_α, and [S II λ6717,6731 emission lines, the i band is affected by [Ar III] λ7135 and [O II] λ7323, and finally, the z band is affected by Paschen hydrogen lines and [S III] λ9069,9532 emission lines.

Table 4.2 summarizes the input parameters for the PN models and the resulting model UV/optical magnitudes as well as R_{out} and Hmass, while Table 4.3 shows the most important emission lines that contribute to the UV-optical bands.

TABLE 4.3— Fluxes of the major nebular emission lines in the range of GALEX and optical bands.

Model	C IV λ1549	He II λ1640	C III] λ1909	[O III] λ2331	[Ne IV] λ2424	He II λ4686	H_β	[O III] λ5007	[N II] λ6548	H_α	[N II] λ6584
					$(-\log(F)$ erg s^{-1} cm^{-2} Å$^{-1})$						
					$R_{\rm in}$ to $R_{\rm out}$						
cA_t3.0_l3.97_g4.00_nh4.30_r16.94	...	18.42	12.48	20.40	31.06	19.35	9.84	14.68	9.84	9.40	9.37
cA_t7.4_l3.95_g4.70_nh3.80_r17.00	12.96	10.11	8.59	12.72	12.02	11.11	8.77	7.58	9.09	8.33	8.63
cA_t18.0_l3.80_g6.40_nh3.30_r17.48	10.32	8.39	8.37	12.72	9.26	9.28	8.91	7.76	8.94	8.47	8.47
cA_t17.0_l2.80_g7.30_nh2.80_r17.71	13.83	9.49	9.67	14.10	11.51	10.38	9.86	8.99	9.43	9.41	8.96
cA_t3.0_l3.47_g4.00_nh4.30_r16.94	...	19.27	13.48	21.27	31.87	20.29	10.33	15.49	10.35	9.89	9.88
cA_t5.0_l3.46_g4.50_nh3.80_r17.00	20.45	12.38	9.34	13.55	16.24	13.96	9.26	8.26	9.48	8.81	9.01
cA_t11.0_l3.16_g6.11_nh3.30_r17.48	13.14	9.62	9.25	13.54	11.48	10.51	9.44	8.39	9.26	8.99	8.79
cA_t11.0_l2.57_g6.70_nh2.80_r17.71	15.75	10.55	10.13	14.65	13.29	11.43	10.03	9.40	9.60	9.58	9.14
					$R_{\rm in}$ to $R_{\rm med}$						
cA_t3.0_l3.97_g4.00_nh4.30_r16.94	...	18.42	12.72	20.40	31.06	19.35	10.05	14.68	10.13	9.62	9.66
cA_t7.4_l3.95_g4.70_nh3.80_r17.00	12.96	10.12	9.34	13.22	12.02	11.12	9.22	8.03	11.32	8.77	10.85
cA_t18.0_l3.80_g6.40_nh3.30_r17.48	10.32	8.43	8.56	12.93	9.27	9.32	9.18	8.01	10.25	8.74	9.78
cA_t17.0_l2.80_g7.30_nh2.80_r17.71	13.83	9.49	9.67	14.10	11.51	10.38	9.87	8.99	9.44	9.42	8.97
cA_t3.0_l3.47_g4.00_nh4.30_r16.94	...	19.27	13.68	21.27	31.87	20.29	10.49	15.49	10.58	10.05	10.11
cA_t5.0_l3.46_g4.50_nh3.80_r17.00	20.45	12.43	9.86	13.93	16.24	13.99	9.58	8.57	10.88	9.13	10.41
cA_t11.0_l3.16_g6.11_nh3.30_r17.48	13.14	9.63	9.47	13.66	11.48	10.52	9.66	8.50	9.96	9.22	9.49
cA_t11.0_l2.57_g6.70_nh2.80_r17.71	15.75	10.57	10.19	14.66	13.30	11.45	10.13	9.41	9.77	9.68	9.30
					$R_{\rm med}$ to $R_{\rm out}$						
cA_t3.0_l3.97_g4.00_nh4.30_r16.94	...	...	12.85	...	...	...	10.25	...	10.16	9.80	9.69
cA_t7.4_l3.95_g4.70_nh3.80_r17.00	...	11.56	8.67	12.89	...	13.31	8.96	7.77	9.10	8.52	8.63
cA_t18.0_l3.80_g6.40_nh3.30_r17.48	13.11	9.45	8.82	13.14	11.00	10.34	9.26	8.11	8.96	8.81	8.49
cA_t17.0_l2.80_g7.30_nh2.80_r17.71	...	11.72	13.21	20.30	16.35	12.60	11.62	14.76	11.36	11.16	10.89
cA_t3.0_l3.47_g4.00_nh4.30_r16.94	...	...	13.92	...	...	...	10.85	...	10.73	10.39	10.26
cA_t5.0_l3.46_g4.50_nh3.80_r17.00	...	13.30	9.49	13.78	...	15.17	9.54	8.54	9.50	9.09	9.03
cA_t11.0_l3.16_g6.11_nh3.30_r17.48	16.48	11.45	9.64	14.16	13.79	12.37	9.83	9.03	9.35	9.38	8.88
cA_t11.0_l2.57_g6.70_nh2.80_r17.71	...	11.93	10.89	16.42	15.44	12.82	10.71	11.19	10.11	10.25	9.64

TABLE 4.4— Model UV/optical magnitudes from the synthetic spectra of PNe models with a binary nuclei. Each set describes the nucleus components.

Model	FUV	NUV	u	g	r	i	z	Comp.	Shell
				(AB magnitude)					
			CS $M = 0.616$ M$_\odot$						
cA_t3.0_l3.97_g4.00_nh4.30_r16.94	6.21	6.64	7.13	7.27	7.53	8.05	8.29	A0III	w
	6.22	6.66	7.19	7.39	7.63	8.16	8.40	F0III	
	6.22	6.67	7.21	7.48	7.70	8.23	8.47	G0III	
	6.22	6.67	7.21	7.43	7.57	7.98	8.13	K0III	
	6.22	6.67	7.21	7.42	7.43	7.61	7.54	M0III	
	6.23	6.65	7.10	7.25	7.35	8.02	8.25	A0III	a
	6.24	6.68	7.16	7.37	7.43	8.12	8.36	F0III	
	6.24	6.68	7.19	7.46	7.49	8.20	8.43	G0III	
	6.24	6.68	7.18	7.42	7.39	7.95	8.09	K0III	
	6.24	6.68	7.19	7.41	7.27	7.59	7.52	M0III	
cA_t7.4_l3.95_g4.70_nh3.80_r17.00	8.23	8.53	8.15	6.58	7.69	8.48	8.54	A0III	w
	8.30	8.66	8.32	6.64	7.81	8.65	8.68	F0III	
	8.30	8.69	8.38	6.68	7.89	8.78	8.78	G0III	
	8.30	8.69	8.38	6.66	7.74	8.38	8.34	K0III	
	8.30	8.69	8.40	6.66	7.58	7.88	7.66	M0III	
	8.09	7.87	6.98	5.48	6.22	7.44	7.32	A0III	a
	8.15	7.94	7.04	5.51	6.25	7.50	7.37	F0III	
	8.15	7.96	7.06	5.52	6.27	7.54	7.39	G0III	
	8.15	7.96	7.06	5.51	6.23	7.40	7.25	K0III	
	8.15	7.96	7.06	5.51	6.19	7.17	6.95	M0III	
cA_t17.0_l2.80_g7.30_nh2.80_r17.71	10.09	9.60	8.19	8.08	7.55	8.99	9.00	A0III	w
	10.56	10.00	8.37	8.36	7.65	9.27	9.22	F0III	
	10.58	10.10	8.44	8.59	7.72	9.50	9.38	G0III	
	10.58	10.10	8.43	8.48	7.59	8.83	8.71	K0III	
	10.58	10.10	8.45	8.45	7.45	8.14	7.84	M0III	
	10.11	9.61	8.20	8.08	7.53	8.98	8.99	A0III	a
	10.58	10.01	8.37	8.35	7.63	9.27	9.22	F0III	
	10.60	10.11	8.44	8.58	7.70	9.49	9.38	G0III	
	10.60	10.11	8.44	8.47	7.57	8.83	8.70	K0III	
	10.60	10.11	8.46	8.44	7.43	8.14	7.84	M0III	
cA_t18.0_l3.80_g6.40_nh3.30_r17.48	7.84	8.21	7.84	6.38	7.43	8.31	8.00	A0III	w
	7.89	8.31	7.96	6.43	7.51	8.46	8.08	F0III	
	7.89	8.33	8.01	6.47	7.58	8.56	8.13	G0III	
	7.89	8.33	8.01	6.45	7.46	8.23	7.87	K0III	
	7.89	8.33	8.02	6.45	7.34	7.78	7.39	M0III	
	7.74	7.75	6.81	5.80	6.16	7.64	7.39	A0III	a
	7.79	7.81	6.86	5.83	6.19	7.72	7.43	F0III	
	7.79	7.82	6.87	5.85	6.21	7.77	7.46	G0III	
	7.79	7.82	6.87	5.84	6.17	7.60	7.31	K0III	
	7.79	7.82	6.88	5.83	6.14	7.33	7.00	M0III	
			CS $M = 0.532$ M$_\odot$						
cA_t3.0_l3.47_g4.00_nh4.30_r16.94	7.42	7.82	8.18	8.11	8.36	8.80	9.01	A0III	w
	7.46	7.89	8.35	8.38	8.58	9.04	9.25	F0III	
	7.46	7.90	8.42	8.62	8.76	9.22	9.41	G0III	
	7.46	7.90	8.42	8.51	8.45	8.67	8.72	K0III	
	7.46	7.90	8.44	8.48	8.16	8.05	7.85	M0III	
	7.43	7.82	8.16	8.10	8.25	8.79	8.99	A0III	a
	7.46	7.89	8.33	8.37	8.44	9.02	9.22	F0III	
	7.46	7.90	8.40	8.61	8.60	9.19	9.38	G0III	
	7.46	7.90	8.40	8.49	8.33	8.66	8.70	K0III	
	7.46	7.90	8.41	8.47	8.07	8.04	7.84	M0III	
cA_t5.0_l3.46_g4.50_nh3.80_r17.00	8.51	8.78	8.57	7.51	8.17	8.82	8.79	A0III	w
	8.61	8.94	8.82	7.66	8.35	9.07	8.97	F0III	
	8.61	8.98	8.93	7.78	8.50	9.25	9.10	G0III	
	8.61	8.98	8.92	7.73	8.25	8.69	8.54	K0III	
	8.61	8.98	8.95	7.71	8.00	8.06	7.77	M0III	
	8.52	8.55	7.88	6.89	7.18	8.30	8.20	A0III	a
	8.61	8.69	8.01	6.97	7.25	8.45	8.30	F0III	
	8.61	8.71	8.06	7.04	7.29	8.55	8.37	G0III	
	8.61	8.72	8.05	7.01	7.20	8.22	8.05	K0III	
	8.61	8.72	8.07	7.00	7.10	7.77	7.50	M0III	
cA_t11.0_l2.57_g6.70_nh2.80_r17.71	10.55	10.11	8.77	8.53	8.18	9.23	9.29	A0III	w
	11.39	10.83	9.08	8.98	8.36	9.60	9.60	F0III	
	11.42	11.06	9.23	9.43	8.51	9.92	9.83	G0III	
	11.42	11.07	9.22	9.20	8.25	9.04	8.92	K0III	
	11.42	11.07	9.25	9.15	8.01	8.24	7.94	M0III	
	10.42	9.94	8.55	8.48	7.86	9.15	9.20	A0III	a
	11.12	10.53	8.80	8.90	8.00	9.48	9.49	F0III	
	11.14	10.69	8.91	9.32	8.10	9.77	9.70	G0III	

Continued on next page

Table 4.4 – *Continued from previous page*

Model	FUV	NUV	u	g	r	i	z	Comp.	Shell
	(AB magnitude)								
	11.14	10.70	8.90	9.10	7.92	8.97	8.86	K0III	
	11.14	10.70	8.93	9.06	7.73	8.21	7.91	M0III	
cA_t11.0_l3.16_g6.11_nh3.30_r17.48	9.79	9.55	8.66	7.43	8.07	8.91	8.77	A0III	w
	10.12	9.92	8.94	7.57	8.23	9.18	8.95	F0III	
	10.13	10.02	9.06	7.68	8.36	9.38	9.07	G0III	
	10.13	10.02	9.05	7.63	8.13	8.77	8.53	K0III	
	10.13	10.02	9.08	7.62	7.91	8.11	7.76	M0III	
	9.48	9.05	7.77	7.16	7.06	8.51	8.41	A0III	a
	9.73	9.27	7.89	7.26	7.12	8.69	8.54	F0III	
	9.73	9.32	7.93	7.34	7.17	8.82	8.63	G0III	
	9.73	9.32	7.93	7.30	7.09	8.41	8.24	K0III	
	9.73	9.32	7.94	7.30	7.00	7.90	7.61	M0III	

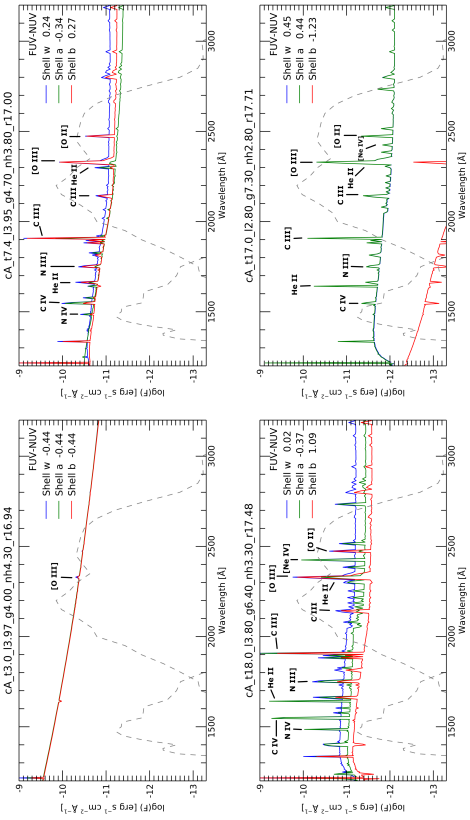

FIGURE 4.8— UV spectra of the computed PN models with CS final mass $M_* = 0.616 M_\odot$. The $T_{\rm eff}$ increase from top-left ($T_{\rm eff}$=170 000 K) to bottom-right ($T_{\rm eff}$=30 000 K) and the $n_{\rm H}/R_{\rm in}$ increases/decreases from top-left ($n_{\rm H}$=4.30 and $\log(R_{\rm in})$=16.94) to bottom-right ($n_{\rm H}$=2.80 and $\log(R_{\rm in})$=17.71), respectively. The GALEX FUV and NUV bands are overlaid. In each panel, we give the synthetic FUV−NUV color computed by convolving the emerging flux with the GALEX transmission curves, for the inner shell ("a"), the outer shell ("b") and the whole-PN model flux ("w").

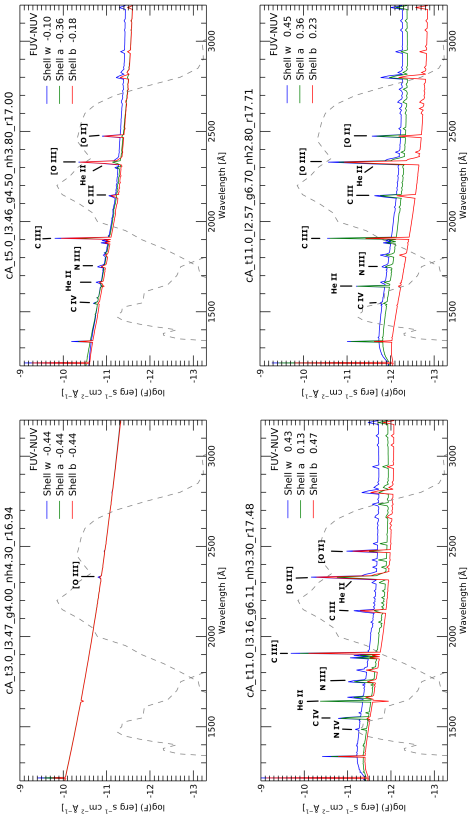

FIGURE 4.9— UV spectra of the computed PN models with CS final mass $M_* = 0.532 M_\odot$. $T_{\rm eff}$ increase from top-right ($T_{\rm eff}$=30000 K) to bottom-right ($T_{\rm eff}$=110000 K) and the $n_{\rm H}/R_{\rm in}$ increase/decrease from top-left ($n_{\rm H}$=4.30 and $\log(R_{\rm in})$=16.94) to bottom-right ($n_{\rm H}$=2.80 and $\log(R_{\rm in})$=17.71), respectively. The GALEX FUV and NUV bands are overlaid. In each panel, we give the synthetic FUV−NUV color computed by convolving the emerging flux with the GALEX transmission curves, for the inner shell ("a"), the outer shell ("b") and the whole-PN model flux ("w").

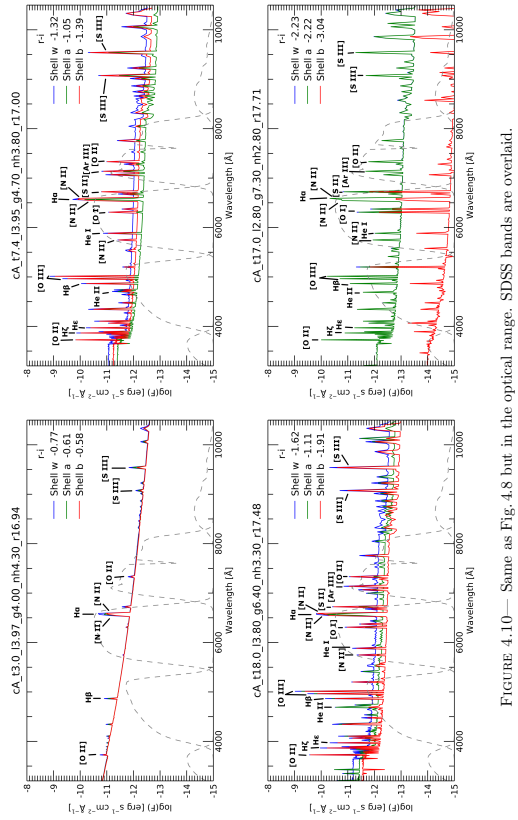

FIGURE 4.10— Same as Fig. 4.8 but in the optical range. SDSS bands are overlaid.

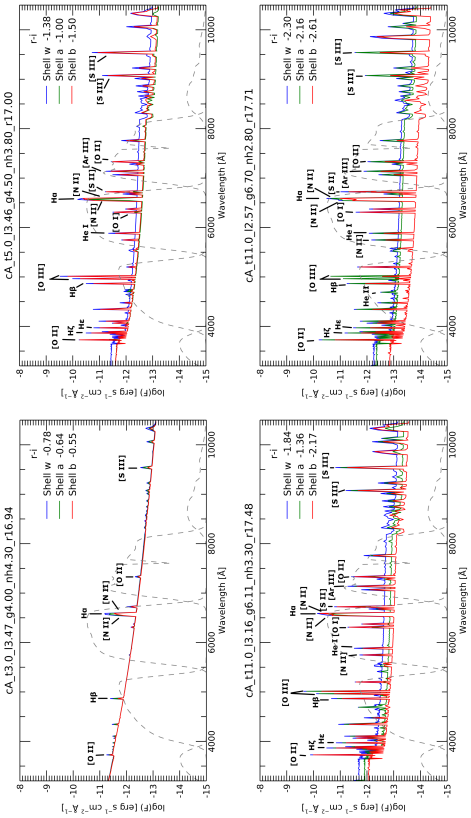

FIGURE 4.11 — Same as Fig. 4.9 but in the optical range. SDSS bands are overlaid.

4.3 Model magnitudes

In this section we analyze the colors of the grid of model spectra of PNe in the GALEX UV and SDSS optical broad bands.

For each PN model computed (Section 4.2.1), we estimated synthetic magnitudes in the GALEX FUV and NUV, and SDSS u g r i z broad bands (Table 4.2) in order to characterize the colors of the PNe. The synthetic magnitudes are in the AB magnitude system and were calculated as follows:

$$m_{\rm AB} = -2.5\log(F_\nu) - 48.6 \tag{4.2}$$

with F_ν defined as

$$F_\nu = \frac{1}{c}\frac{\int F_\lambda R(\lambda)\lambda\, d\lambda}{\int R(\lambda)/\lambda\, d\lambda} \tag{4.3}$$

where c is the speed of light (2.99792458×10^{18} Å s^{-1}), F_λ is the emergent spectrum from the models, and $R(\lambda)$ is the filter response[3] for each broad band. Model colors for major classes of astrophysical objects, described by Bianchi et al. (2007), are also shown in Figures 4.12 to 4.15.

Theoretical stellar colors for main-sequence (MS; Z=0.02) and supergiant (SG; Z=0.02) stars are derived from the stellar libraries of Castelli & Kurucz (2003), respectively. We also used the stellar library from Bianchi et al. (2007) of WD models for various gravities and solar (Z=0.02), pure H, pure He abundances. In Figures 4.12 to 4.15 a stellar sequence of $\log(g)$ =3, 5, and 7 dex for SG, MS, and WD, respectively, is shown for a range of $T_{\rm eff}$. Although we are using the theoretically post-AGB tracks from Miller Bertolami (2016) with solar metallicity Z=0.01 dex, similar to recent values of solar metallicity reported in the literature (Z=0.012; Grevesse et al., 2007), effects on the model colors by using Z=0.01 or Z=0.02 are negligible (see Figure 6 and 5 from Bianchi et al., 2007, 2011a, respectively, which show a comparison between metallicities Z=0.02 and Z=0.002).

To analyze the position of PNe with a binary nucleus, we added models of giant star companions of M0III, K0III, G0III, F0III, and A0III spectral types to IB models (see Table 4.4). We also added a MS companion of M0V, K0V, F0V, G0V, and A0V to IB models. However, the nebular continuum and line emission are several orders of magnitude brighter than the MS star, and therefore, we do not show them in color-color figures. The companion stars were added separately to each PNe model spectrum.

[3]Transmission curves were obtained from the Spanish Virtual Observatory at `http://svo2.cab.inta-csic.es/theory/fps/`

4.4 Color-color diagrams

4.4.1 PNe locus in color-color diagrams

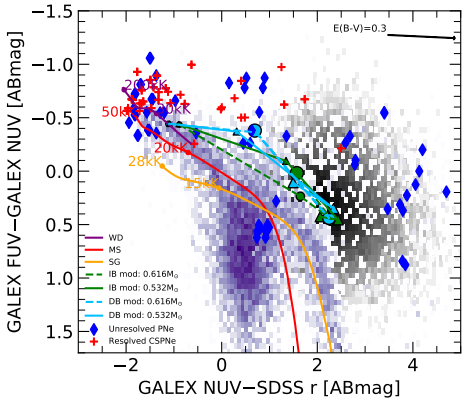

FIGURE 4.12— Color-color diagram for GUVcat_AIS_SDSSdr14 in GALEX and SDSS bands. The purple/black densities indicate the point-like/extended sources, respectively, as described in Bianchi et al. (2011a) and Bianchi & Shiao (2020). The red/orange/purple stellar sequences are model colors for MS, supergiant, and WD stars, respectively. The PNe IB ("w") and DB ("a") models are over-plotted in green and cyan, respectively. The dashed and solid green lines indicate CS final masses of $M_* = 0.532\,M_\odot$ and $M_* = 0.616\,M_\odot$, respectively. Symbols sizes for each PN model indicates the $T_{\rm eff}$ from lower to higher and $n_{\rm H}$ from higher to lower (see Table 4.1). Unresolved PNe (blue diamonds) and resolved PNe (red pluses) from GPNSPcat are also shown.

Figures 4.12 to 4.15 show different combinations of colors from the model magnitudes computed in Section 4.3 with our model grid. In the figures we also show the catalog of GALEX-SDSS matched sources from Bianchi & Shiao (2020) (using the GUVcat_AIS from Bianchi et al., 2017, and SDSS DR14), which is an improved and expanded version of the UV source catalogs of Bianchi et al. (2011a) and Bianchi (2014). For the color-color diagram analysis we used

the GUVCat_AIS matched with SDSS DR14 (Bianchi et al., 2019) sample restricted to Galactic latitudes ($70 \leq b \leq 90$) to avoid high extinction (according to the extinction maps from Schlafly & Finkbeiner, 2011). The catalog GUVCat_AIS×SDSS DR14 is shown as a density map of point-like/extended sources, represented as blue/black density points, respectively, according to the classification of SDSS catalog measurements. Error cuts of 0.3 mag in GALEX and 0.05 mag in SDSS were applied.

The intervening dust must be taken into account for analyzing and identifying objects via photometric colors. The interstellar extinction will redden an object, changing its position in a color-color diagram. To draw a reddening vector, we applied to the model spectra the reddening law of CCM89 with a Galactic extinction of $R_V = 3.1$ and $E(B-V)$=0.3. All figures presented in this section show a typical reddening vector for $E(B-V) = 0.3$ mag.

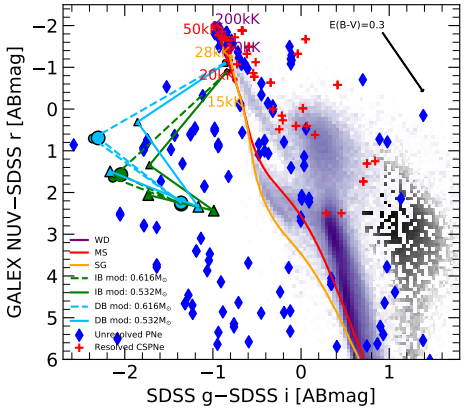

FIGURE 4.13— Same data and symbols as in Figure 4.12. Plot show the SDSS $g-i$ versus GALEX NUV−SDSS r diagram.

In order to validate the model spectra with data of known samples we also use our catalog of known PNe detected in UV-optical bands, as described in Chapter 2. This catalog is a compilation of coordinates of Galactic PNe

matched with GALEX GR6/7, and with SDSS DR14 and PanSTARRS (GPNcatxSDSSDR14xPS1DR2, GPNSPcat for short; see Section 2.5). In the case of PanSTARRS, we only use r and i in the color-color diagrams, since the differences with respect to SDSS r and i are practically negligible (Tonry et al., 2012).

In all color-color diagrams the PNe model colors are relatively well separated from the theoretical model colors for other astrophysical sources. An exception is in the FUV−NUV versus NUV−SDSS r color-color diagram (Fig. 4.12), in which the locus of the PNe models lies somewhat in between and is occupied in this diagram by the cloud of the SDSS extended sources (black density points). Also, in this figure, the PNe model colors are also separated from the observed PNe. In this particular figure, this could be explained by the combination of GALEX NUV and SDSS r, as the absorption due to reddening in GALEX NUV is much higher than in optical bands. Hence, the colors are very sensitive to moderate reddening amounts (e.g., for $E(B-V) = 0.3$ mag, the GALEX NUV−SDSS r changes ∼1.56 mag, as seen in Figure 4.12).

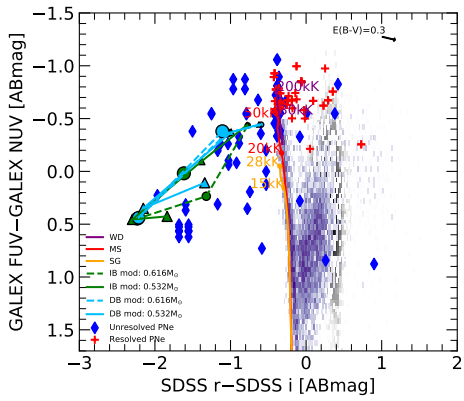

FIGURE 4.14— Same data and symbols as in Figure 4.12. Plot show the SDSS $r-i$ versus GALEX FUV −NUV diagram.

In Figure 4.13 the PNe models occupy a separated space from other astrophysical objects with SDSS $g-i$ between -0.8 and -3.0 and with GALEX NUV−SDSS r between -1.5 and 3.0. Also, DB ("a")models and IB ("w") models, shown as green and cyan lines (solid and dashed lines for CS masses of 0.616 and 0.532 $M_{\odot}$, respectively), occupy a separate space between them. The DB models have redder color in GALEX NUV−SDSS r than the IB models as expected, because of DB models contain less nebular continuum. This is useful for DB and IB classification. Similar behavior can be seen in Figures 4.14 and 4.15, where the PNe models also occupy a separated space from other astrophysical objects. Although these 3 diagrams are useful in identifying new PN candidates of all ages, the best choice is the SDSS $r-i$ versus GALEX FUV−NUV color-color diagram (Figure 4.14) as these combination of colors are not very sensitive (for $E(B-V)=0.3$ the color SDSS$r-i$ is affected by 0.2 mag) to interstellar extinction (it can be seen, in the figure, that PNe models and observed unresolved PNe occupy the same color space).

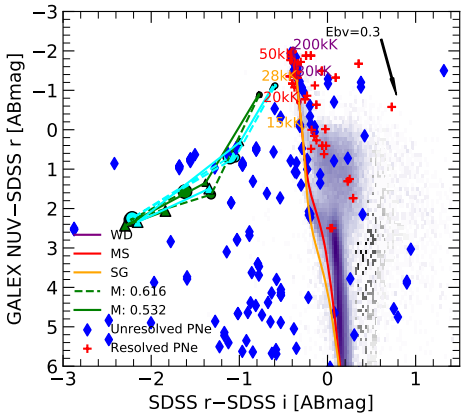

FIGURE 4.15— Same data and symbols as in Figure 4.12. Plot show the SDSS $r-i$ versus GALEX NUV−SDSS r diagram.

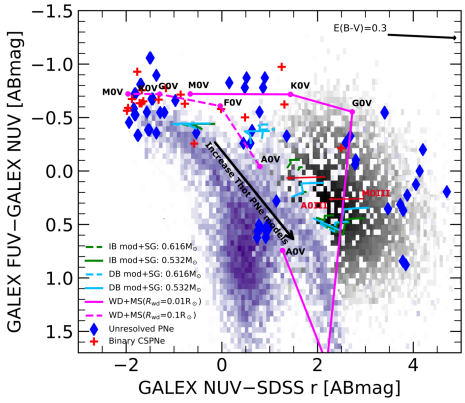

FIGURE 4.16— Color-color diagram for the GUVcat_AIS_SDSSdr14 in the GALEX and SDSS bands. The gray blue/black densities indicate the point-like/extended sources, respectively, as described in Bianchi et al. (2011a) and Bianchi & Shiao (2020). Binary PNe model magnitudes are over-plotted in green and cyan, for the IB ("w") and DB ("a") models, respectively. The dashed and solid green/cyan lines indicates CS mass $M_* = 0.532\,M_\odot$ and $M_* = 0.616\,M_\odot$, respectively. The black arrow indicates the increase direction of $T_{\rm hot}$ of PNe models (see Table 4.1 for values of $T_{\rm hot}$ for each model). Red arrow indicates the direction of PNe models+SG from M0II to A0II. Unressolved PNe (blue diamonds) and binary CSPNe (also resolved PNe; red pluses) from GPNSPcat are also shown.

Vejar et al. (2019) found a hook-like shape in their analysis of color-color diagrams using only the Large Synoptic Survey Telescope SDSS *ugriz* bands convolved to PNe photoionization models for a CS mass of $M = 0.616\ M_\odot$. In this work we found a similar behavior in all color-color diagrams. This hook-shaped follows the PNe evolution. As the PN evolutionary age increases, the density decreases and the shell expands and merges with the interstellar medium, becoming transparent to ionizing photons. After several thousands years in the evolution of a PN ($\geq$1000yrs for a final mass of 0.616 $M_\odot$ according to Figure 4.1) the emission from the nebula no longer contributes to the overall

flux and the colors describe the evolution of a WD star (i.e., the colors will evolve to the WD loci).

We note that the outer shell ("b") models are practically indistinguishable from IB and DB models in all colors maps and hence removed from the color analysis.

4.4.2 PNe with binary CS

To analyze the locus of PNe with a binary nuclei, we added a giant star companion of M0III, K0III, G0III, and F0III spectral types (see Table 4.4 for the model magnitudes) to the already calculated IB ("w") and DB ("a") PNe models.

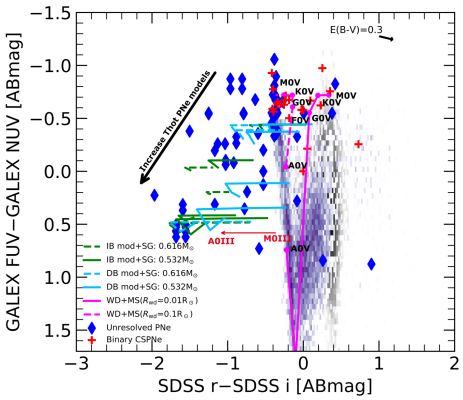

FIGURE 4.17— Same data and symbols as in Figure 4.16. Plot show the GALEX NUV−SDSS r versus GALEX FUV−NUV diagram.

Bianchi et al. (2011a) investigated the power of different color-color-diagrams to accurately separate the hot stellar sources from other astrophysical objects. They found that the GALEX NUV−SDSS r vs GALEX FUV−NUV color-color diagram, with colors GALEX FUV−NUV< -0.13 and GALEX NUV−SDSS $r < 0.1$, separates single hot-stars, while the colors GALEX NUV−SDSS $r > 0.1$ separates binary star candidates. Figures 4.16 and 4.17 show theoretical tracks

of WD+MS companion for different spectral types labeled in the figure for a WD ($\log(g)$=7 dex) with radius of 0.01 $R_\odot$ (pink solid line) and 0.1 $R_\odot$ (pink dashed line) and $T_{\rm eff}$=100 000 K. Such figures also show binary PNe+SG companion for different spectral types (see Table 4.4).

As shown in Figure 4.16, observed binary CSPNe, from GPNSPcat, could be easily identified by applying the color cuts described by Bianchi et al. (2011a). This is expected as the binaries CSPNe from GPNSPcat do not have nebular contribution. However, using this color-color diagram to identify binaries CSPNe requires accurate reddening, $E(B-V)$, correction. Note, from the figure, that CSPNe with high amounts of extinction could mimic the colors of a binary CSPNe (see Figure 3.7 in Section 3.5).

However, the color-color diagram presented in Figure 4.17 is very sensitive to our models of binary stars (Table 4.4). The colors GALEX FUV−NUV<1 and SDSS $r-i$ <0.4 define the region of the binary models. Also, note that the combination of colors are also not very sensitive to moderate amounts of extinction (for a Galactic type dust; $R_{\rm V}=3.1$ mag). Therefore, this, in principle, is useful for the identification of new binary CSPNe for unresolved PNe.

4.5 Summary

As discussed in previous sections, color-color diagrams can be used to separate objects by astrophysical class, and in particular to select hot-WDs with a cool companion (MS or G; Bianchi & Shiao, 2020).

Several studies have shown that emission line objects, such as PNe, can be identified or characterized by broadband filters. Kniazev et al. (2014) used the SDSS colors to separate PNe from other sources in the outskirts of M31. Parker et al. (2016) developed a method using mid-IR colors to identify Galactic PN candidates using available data from the Galactic Legacy Infrared Mid-Plane Survey Extraordinaire I archive. But so far, binaries in unresolved or compact PNe are not studied in detail (an exception is the work of Ciardullo et al. (1999), who used the Hubble Space Telescope Snapshot survey to locate binary CSPNe by physical association).

In this work, we used the photoionization code CLOUDY to model PNe following the evolutionary tracks of Miller Bertolami (2016) with final masses of 0.616 $M_\odot$ and 0.532 $M_\odot$, for four different stages of PNe evolution. We found by analyzing UV-optical color-color diagrams, that PNe models occupy a color space relatively well separated from other astrophysical objects in the combination of GALEX FUV−NUV and SDSS $r-i$, ranging from −1 to 3.0 and −0.8 to −2.4, respectively. We also find that PNe with an evolved companion is not

easy to identify.

The methodology and results presented in this thesis demonstrate the potential of using synthetic UV/optical PNe spectra and a set of filters to produce accurate magnitudes and colors. However, we have only modeled CSs with final masses of 0.616 and 0.532 $M_{\odot}$. By expanding these models to a wider range of final masses we would have a better understanding of the distribution of single and binary PNe.

5

The central star of NGC 2346, as a clue to binary evolution through the common envelope phase

Based on
Gómez-Muñoz et al. 2019, ApJ, 885, 1

Abstract – **We present an analysis of the binary central star of NGC 2346 based on archival data from the International Ultraviolet Explorer, and new observations of low- and high-resolution optical spectra. By including the stellar and nebular continuum, we reconcile log-time discrepancy UV and optical diagnostics from the literature and derive $E(B-V) = 0.18 \pm 0.01$. We classified the companion star's spectral type as A5IV by analyzing the wings of the Balmer absorption lines of the high-resolution (R = 67 000) optical spectra (3700–7300 Å). Using the distance to the nebula of 1400 pc from Gaia DR2, we constructed a photoionization model based on abundances and line intensities derived from the low-resolution optical spectra to obtain the temperature ($T_{\rm eff}$=130 000 K) and luminosity ($L = 170\,{\rm L}_{\odot}$) of the ionizing star, which are consistent with the UV continuum. This analysis allows us to better constrain the binary system. We conclude that the progenitor star of NG 2346 has evolved through a common envelope phase, in which the companion star has evolved off the main-sequence.**

5.1 Introduction

The planetary nebula (PN) NGC 2346 ($07^{\rm h}09^{\rm m}22.52^{\rm s} - 00^{\rm d}48'23.61''$, J2000), is a bipolar PN with a single-lined spectroscopic binary central star (CS)

with an orbital period of 16 d (Mendez & Niemela, 1981, hereafter MN81) recently confirmed by (Brown et al., 2019). The binary system consists of the ionizing star, presumably a sdO star (Feibelman & Aller, 1984) with a derived temperature of ∼100 000 K by using the Zanstra method (Calvet & Cohen, 1978), and an A-type star companion (Kohoutek & Senkbeil, 1973). Feibelman & Aller (1983) obtained several *International Ultraviolet Explorer* (IUE) spectra in which the hot stellar continuum was present. Based on the observed emission lines of C IV 1550λ, He II 1641λ, and N V1243λ, *MN81* suggested a $T_{\rm eff}$ in the range of 60 000 K–100 000 K, but they did not fit a stellar model to the spectra. A Luminosity class III of the A-type star was inferred by Kohoutek & Senkbeil (1973), using photoelectric UBV photometry, whereas MN81 obtained a luminosity class V by fitting the width of the Hγ absorption line, however this method is relatively insensitive to $\log(g)$ for stars hotter than ∼ 8000 K. Latter Smalley (1997), fitting the wings of the Hβ balmer line in a medium-resolution spectrum, obtained a maximum value of $\log(g) = 3.5$. Recently, Brown et al. (2019) obtained $T_{\rm eff}$= 7750 ± 200 K and $\log(g) = 3.0 \pm 0.25$ for the cool star.

The orbital separation of this binary system, ∼0.16 AU, was calculated by Manchado et al. (2015), who assumed a mass of 1.8 $M_\odot$ for the cool star with an orbital inclination angle set to that of the bipolar lobes. Manchado et al. (2015) suggested that the system could be a remnant of a common-envelope (CE) evolution. The common envelope is short-lived phase in the life of a binary system during which two stars orbit inside a single, shared envelope (Ivanova et al., 2013). Hall et al. (2013) discussed the formation of PNe in binary systems via a CE phase starting when a giant star overflows its Roche lobe. Other works suggest that NGC 2346 did not undergo CE evolution, mass transfer occurred instead from an evolved primary onto the companion via Roche Lobe Overflow (de Kool & Ritter, 1993).

NGC 2346 is also remarkable because of photometric variability reported during certain periods of the order of years. No luminosity variations were reported for the A5 star until magnitude variations in form of eclipse, by up to 2 mag in the V band, occurred from 1981 to 1986 (Costero et al., 1986). As we will see in section 5.2.3, using the IUE archival data, these variations were seen until 1993. Schaefer (1985) suggested that the light variation is related to an obscuring dust cloud (expanding material from the hot component). Alternative explanations have been presented by Costero et al. (1986), who suggested an ellipsoidal cool dust cloudlet with mass of $10^{-13} M_\odot$ was responsible for the variation, and by Peña & Hobart (1994), who proposed that the variation is due to the pulsation and eclipse of a triple system. Circumstellar dust was observed with the *Spitzer* Multiband Imaging Photometer (MIPS) (Su et al., 2004), near the waist part of the bipolar nebula. Using *Multi-conjugate adaptive*

optics H_2 maps (90 milliarcseconds resolution), Manchado et al. (2015) have resolved this structure into clumps and knots.

There are discrepancies between the $E(B-V)$ values calculated from the nebular Hβ emission (0.164−0.68, Aller & Czyzak, 1979; Calvet & Cohen, 1978; Méndez, 1978; Phillips & Cuesta, 2000) and the CS photometry (0.07, Méndez, 1978)) to NGC 2346. Phillips & Cuesta (2000) found this discrepancy to be strongly dependent on the extinction determination for the central star, based mostly on photographic or photoelectric scans (Méndez, 1978). Also, Phillips & Cuesta (2000) have found, by means of narrowband images in the transitions of H I λ6563+λ4861 and [O III] λ5007, that the extinction of the central region of the nebula is surprisingly uniform ($E(B-V) = 0.64 - 0.78$) with a little evidence for reddening variation along the nebula.

We use the distance scale of Bailer-Jones et al. (2018), derived from Gaia DR2 parallaxes, to derive a value of 1401^{+93}_{-84} pc for NGC 2346. This distance is a factor of two different from the often assumed value of ∼700 pc (MN81) derived from a probably incorrect reddening determination. This chapter aims to constrain the atmospheric parameters and the evolutionary state of the binary system of NGC 2346, and analyze the implications regarding the past evolution of this binary system.

5.2 Observations

5.2.1 High-resolution optical spectra

High-resolution optical spectra were taken in 2018 January 12 using the Fiber-fed Echelle Spectrograph (FIES, Telting et al., 2014) mounted on the 2.5m Nordic Optical Telescope (NOT) at Roque de Los Muchachos Observatory on La Palma (Spain). We used the high-resolution mode, which provides a resolution of R=67 000 in the whole visible spectral range (3700–7300Å). The exposure time was set to 1 hr, divided into four exposures of 900 s, to obtain a S/N≈30 at 5550Å per exposure.

FIES data were reduced with the dedicated PYTHON reduction software FIEStool[1] based on IRAF[2]. The standard procedures have been applied, which include bias subtraction, extraction of scattered light produced by the optical system, cosmic ray filtering, division by a normalized flat-field, wavelength calibration by a ThAr lamp, and order merging. We combined all merged spectra to obtain a S/N of ∼62 at 5550Å. After radial velocity correction of the spectrum,

[1] http://www.not.iac.es/instruments/fies/fiestool/
[2] Image Reduction and Analysis Facility. `http://ast.noao.edu/data/software`

we normalize the flux to the local continuum using iSpec (Blanco-Cuaresma et al., 2014) by fitting a low-order polynomial to the continuum.

5.2.2 Low-resolution optical spectra

Long-slit spectra of NGC 2346 were obtained with the Boller & Chivens spectrograph mounted on the 2.1m telescope at the Observatorio Astronómico Nacional, San Pedro Mártir (OAN-SPM) in México, during three observing runs: 2015 February 7, 9, and 11. An E2V CCD with 2048×2048 pixel array and a plate scale of $1.18''\,\mathrm{pix}^{-1}$ (in a 2×2 binning mode) was used as a detector. The $400\,\mathrm{lines\,mm}^{-1}$ grating was used with a $2''$-wide slit yielding a spectral resolution of ≈ 5.5Å (FWHM; R=900), as judged by the arc calibration lamp spectrum, covering the 4100–7600Å spectral range. Slit positions, labeled s1–s3, are shown in Figure 5.1. The position angles (PAs) for these observations were +75° for s1 and s2, and -15° for s3. The exposure times were 600, 1200, and 800 s, respectively.

The spectra were reduced using standard procedures for long-slit spectra within the IRAF package. We flux-calibrated the spectra by using the standard star Feige 34. For each slit position, the observed spectra were extracted with the APALL task to separate the stellar component from the surrounding nebular emission. Line fluxes for each extracted region were measured using the *splot* task and fitting a Gaussian function to each line. The errors were estimated according to the RMS noise measured from flat spectral regions and then adding >100 Monte-Carlo simulations for each measurement (i.e., errors were estimated as the standard deviation of >100 random flux variations in a normal distribution, with μ=0 and σ=1, as a function of the RMS value). Table 5.1 lists the lines intensity (see 5.3.2). UV emission lines (Sec. 5.2.3) are also included in this table.

5.2.3 Low-resolution UV spectra

We have retrieved all the *International Ultraviolet Explorer* (IUE) archival spectra available for NGC 2346 from the IUE *Newly Extracted Spectra* (INES)[3].

Short-wavelength (SW 1200–2000 Å) and long-wavelength (LW 2000–3300 Å) spectra were obtained from 1981 to 1993. The spectra are shown in Figure 5.3.

We integrated the flux in three different narrow bands $F_{1220-1280}$ (1220–1280Å), $F_{1830-1870}$ (1830–1870Å), and F2750 − 2800 (2750–2800Å) to analyze differences between the spectra. Fluxes were integrated, avoiding bad pixels according to the QUALITY flag. The spectra are listed in Table 5.4, with dates,

[3] http://sdc.cab.inta-csic.es/cgi-lines/IUEdbsMY

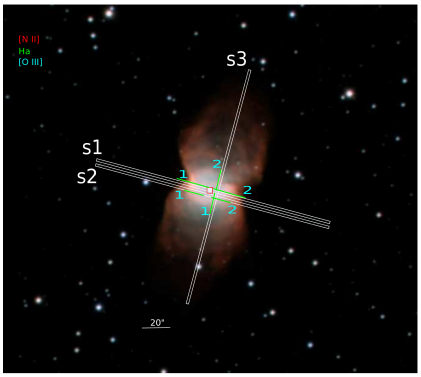

FIGURE 5.1— Image of NGC 2346 taken with the 0.84 m telescope at the OAN-SPM in three different filters. The image is composed by colors red for [N II] λ6584 Å, green for H_α, and blue for [O III] λ5007 Å. The red square shows the position of the CS. Overplotted are the slits positions of the low-resolution optical spectra. North is up and East is left.

exposure times, phase of the orbit (calculated with $t_0 = 2443142$ d and period of 16 d, MN81), integrated flux in the $F_{1288-1305}$, $F_{1825-1845}$, and $F_{2670-2750}$ narrow bands, and comments related to the quality of the spectra. The UV line fluxes were measured using the *splot* task in IRAF and fitting a Gaussian profile to each line. Errors were calculated integrating the sigma flux (SIGMA) in the same wavelength range as the line flux. Table 5.5 shows the measured line intensities in the UV range. The reddening correction is discussed in Section 5.3.2.

5.3 Results

5.3.1 The A-type companion of the CSPN

In order to derive the stellar parameters of the CSPN companion, we compare the stellar lines of the observed high-resolution optical spectra to the library of high-resolution solar-composition Coelho stellar models (Coelho, 2014)

TABLE 5.1— Intrinsic line intensities of NGC 2346.

Line	fλ	s1R1[a]	s1R2[a]
1551λ C IV	1.949	27.74±2.98	31.59±3.40
1640λ He II	1.819	95.34±3.10	108.56±3.54
1666λ O III]	1.796	6.50±1.60	7.41±1.82
1749λ N III]	1.769	7.98±1.69	9.08±1.93
1907-09λ C III]	1.999	139.80±1.90	159.19±2.17
3726-29λ [O II]	0.38	376.30±37.64	376.32±37.64
4102λ Hδ+He II	0.263	24.97±0.33	25.62±0.32
4341λ Hγ	0.175	46.60±0.29	46.01±0.27
4363λ [O III]	0.167	7.98±0.16	7.70±0.20
4471λ He I	0.128	5.54±0.25	6.87±0.35
4686λ He II	0.054	14.73±0.27	16.77±0.26
4711λ He I+[Ar IV]	0.046	1.96±0.37	1.51±0.33
4740λ [Ar IV]	0.037	4.04±0.41	0.56±0.20
4861λ H_β	0.0	100.00±0.27	100.00±0.30
4922λ He I	-0.017	2.26±0.47	2.01±0.30
4959λ [O III]	-0.027	338.05±0.69	305.32±0.68
5007λ [O III]	-0.04	1002.14±1.92	898.54±1.93
5198λ [N I]	-0.086	7.24±0.18	7.74±0.28
5518λ [Cl III]	-0.149	...	0.96±0.31
5538λ [Cl III]	-0.152	0.66±0.21	0.50±0.24
5755λ [N II]	-0.187	7.41±0.20	8.12±0.19
5876λ He I	-0.205	15.57±0.15	15.12±0.15
6300λ [O I]	-0.26	27.75±0.20	31.12±0.17
6312λ [S III]+He II	-0.262	0.59±0.09	0.73±0.09
6364λ [O I]	-0.268	9.07±0.22	9.69±0.15
6548λ [N II]	-0.29	155.20±0.31	176.87±0.39
6563λ H_α	-0.292	287.94±0.57	287.49±0.63
6584λ [N II]	-0.294	475.51±0.93	535.35±1.15
6678λ He I	-0.305	4.47±0.23	4.52±0.20
6716λ [S II]	-0.31	7.51±0.15	11.25±0.16
6731λ [S II]	-0.312	6.13±0.17	9.97±0.16
7065λ He I	-0.35	4.03±0.17	4.59±0.18
7136λ [Ar III]	-0.359	27.32±0.22	26.74±0.19
7281λ He I	-0.375	0.35±0.19	...
7320λ [O II]	-0.38	5.62±0.20	7.60±0.23
7330λ [O II]	-0.381	5.61±0.21	6.83±0.20
$\log(F(H_\beta))$[b]	...	-12.422	-12.341

[a] All line intensities were derredened using $E(B-V) = 0.18$. The intensities are with respect to $F(H_\beta)$=100.0.
[b] $F(H_\beta)$ in units of erg s^{-1} cm^{-2} .

by degrading the resolution of the observed spectra to an FWHM of 0.282 Å (R∼20 000).

We then analyzed the wings of the Balmer absorption lines from the observed spectra by fitting the set of Coelho models convolved with a FWHM of 0.282 Å. Additionally, the models were convolved with the projected rotation velocity, $V_{\rm rot}$=47.8 km s^{-1}, as obtained from the stellar Mg II λ4481 absorption line by fitting a rotational profile defined by Gray (2005). We employed a reduced $\chi^2_{\rm Red}$ statistic,

$$\chi^2_{\rm Red} = \frac{1}{N-k}\sum_{i=1}^{N}\left(\frac{O_i - E_i}{\sigma_i}\right)^2 \quad (5.1)$$

where N is the number of wavelength points, k is the number of free parameters (in this case just two, $T_{\rm eff}$ and log(g)), E_i is the synthetic normalized spectra, O_i the observed normalized spectra, and σ_i=1/(S/N). We minimized the fit for Hγ and H$_\beta$ to obtain log(g) for each of several plausible values of $T_{\rm eff}$ (7000–9750 K). For $T_{\rm eff}$ and log(g), the best fit yield $T_{\rm eff}$=8000±250 K and log(g) = 3.5±0.5 (Figure 5.2). The $\chi^2_{\rm Red}$ were only estimated in the wings of the Balmer absorption lines since the core of the lines are contaminated by the nebular emission lines. Different values of the obtained $\chi^2_{\rm Red}$ are plotted as contours in the lower panel of Fig. 5.2.

We also fitted the high-resolution spectra using the spectral synthesis and modelling tool iSpec[4]. A reasonable fit was obtained iteratively by using Kurucz model atmospheres (Castelli & Kurucz, 2003) to produce synthetic spectra with the SYNTHE spectral synthesis code (Kurucz, 1993). The iteration process and χ^2 minimization routine are outlined in Blanco-Cuaresma et al. (2014). To obtain the atmospheric parameters we follow the steps recommended by Blanco-Cuaresma et al. (2014), varying $T_{\rm eff}$, log(g), [M/H], micro-turbulence ($v_{\rm micro}$), and macro-turbulence ($v_{\rm macro}$), and setting $V_{\rm rot}$=2 km s^{-1}. The resulting effective temperature, $T_{\rm eff}$=8130±130 K, and surface gravity, log(g)=3.43±0.10, are both consistent with our previous results. In addition, it was possible to fit the micro-turbulence parameter, resulting in $v_{\rm micro}$=3.28 km s^{-1}. With all these parameters fixed, a second run with iSpec was necessary to find $V_{\rm rot}$, resulting in $V_{\rm rot}$=52±17.0 km s^{-1}. We have combined the values from both methods, with a statistical weight, to obtain a mean value of $T_{\rm eff}$=8065±180 K and log(g)=3.43±0.10. These values along with the $v_{\rm micro}$ value, indicate that the A-type star is more probably a sub-giant rather than a main-sequence star (Gray et al., 2001, , A5IV).

[4]https://www.blancocuaresma.com/s/iSpec

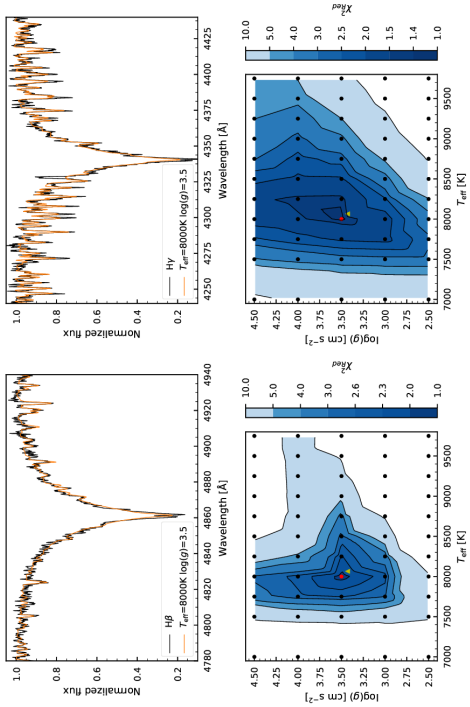

FIGURE 5.2 — Spectra model fit to the normalized H_β and H_γ of NGC 2346 (top panel). The best fit was obtained using the $\chi^2_{\rm red}$ for a grid of atmosphere models (black dots) and each fit is represented as a contour plot of different linearly-interpolated levels of $\chi^2_{\rm Red}$ in the $T_{\rm eff}$ vs $\log(g)$ plane. The best-fit was expected to be close the unity and is represented as a red dot. The best-fit obtained with iSpec is also plotted (yellow triangle). The mean-weighted effective temperature and gravity are $T_{\rm eff}$=8065±180K and $\log(g)$=3.43±0.1.

5.3.2 Extinction determination from nebular lines

A reddening of $E(B-V) = 0.18 \pm 0.01$ was obtained from a least-square fit to the different H_α/H_β, H_γ/H_β, and H_γ/H_α flux ratios for each extracted spectral region of NGC 2346. We assumed a Case B recombination ($n_e = 10^2$ and $T_e = 10^4$) and theoretical ratios of 2.863, 0.468, and 0.1635, respectively (Osterbrock & Ferland, 2006), in conjunction with the extinction law of Cardelli et al. (1989, , hereafter CCM89). A Monte-Carlo simulation around the flux errors was added to each line. The results from the least-square fit for the different ratios were mean-weighted to obtain the final extinction coefficient value. The errors that we are reporting are purely obtained from the least-squares fitting and the Monte-Carlo simulation (flux errors, for the nebular Balmer lines, are less than 5%).

The value obtained using the Balmer decrement is in agreement with that measured by Aller & Czyzak (1979).

5.3.3 Physical conditions of the PN

We used the PYNEB code (Luridiana et al., 2015), a tool for analyzing emission lines, to calculate n_e and T_e from diagnostics diagrams using the corresponding line intensities and errors. The physical conditions were estimated only for the central regions in slit s1 as is the only slit passing through the CS. To obtain the physical conditions in NGC 2346, an extinction correction to the line intensities of $E(B-V) = 0.18$ obtained from the Balmer decrement ratio in Sect. 5.3.2 was used. T_e was determined from [O III] (λ5007+λ4959)/λ4363 and [N II] (λ6548+λ6583)/λ5755, for high- and low-excitation regions, respectively (Osterbrock & Ferland, 2006), and n_e was determined from [S II] λ6716/λ5731. Although the [Cl III] λ5517-37 and [Ar IV] λ4711-40 emission lines are present in most of the regions, the uncertainty was very high and they were not used. The electron density n_e and temperature T_e are reported in Table 5.2 for the different regions.

5.3.4 Nebular abundances

Ionic and elemental abundance values obtained with the PYNEB code are presented in Table 5.2. Ionization correction factors are needed because of the limited ionization stages observed for each element. We used the ionization correction factors (ICFs) obtained by Kingsburgh & Barlow (1994). Some exceptions were the Cl and He abundances. For Cl we used the Delgado-Inglada et al. (2014) ICF because the correction considers only the optical range, and

for He we used the Vazquez et al. (1998) ICF, which includes the correction for collisional effects.

In order to determine the C abundance, we used the collisionally excited C III] λ1909 line from the IUE spectra, scaled to the observed H_β flux according to the theoretical ratio of He II 1640/4686 Å (ratio of 6.474, assuming a Case B recombination), because no C optical recombination emission lines were found in the optical spectra. This ratio has a little temperature and density dependence. For the O abundance, we do not consider the [O II]λ7320-30 lines since they are affected by fluorescence and sky-subtraction. We used the [O II] λ3726 obtained from the literature (Kaler et al., 1976).

Abundances for NGC 2346 were estimated before (Stanghellini et al., 2006b) and the results reported here could differ slightly from those due to different apertures, position, and extinction correction. The elemental abundance results indicate that NGC 2346 is a non-Type I PN because of the ratio of He/H=0.1283±0.017 and N/O=0.75±0.04 (Type I: He/H≥0.14 and log(N/O) >0, Peimbert & Serrano, 1980). Accordingly to García-Hernández et al. (2016), these abundances indicate that the progenitor star has a mass larger than 3 $M_\odot$ and probably between 3.5 and 4.5 $M_\odot$, as expected from the AGB models predictions and Galactic PNe sample therein.

5.3.5 Photoionization model

In order to obtain the different emission components in the UV spectra (ionizing star + nebular continuum), we computed a photoionization model using PYCLOUDY (Morisset, 2013b), a set of tools for dealing with the photoionization code CLOUDY v.17.00 (Ferland et al., 2017), based on our observed emission lines and chemical abundances. The luminosity and stellar temperature for the ionizing star, nebular diameter, and elemental abundances were optimized to reproduce the observed line fluxes in the UV/optical range, as well as that of the [O II] 3729λ line from the literature. The optimization procedure tells the code to vary one or more stellar or nebular parameters to reproduce observations, in this case the observed line intensities.

The optimized values were $T_{\rm eff}$=130 000 K, L=170 $L_\odot$, internal radius 0.043 parsecs, and logarithm of the hydrogen density 2.72.

The model considers the PN as a sphere since we do not attempt to simulate an observation with a slit position, and the long-slit low-resolution spectra do not provide enough observational constraints to model the morphology realistically. A comparison of observed and modeled line ratios is presented in Table 5.3.

TABLE 5.2— Physical parameters and abundances.

Line	s1R1	s1R2
N_e[S II]	179.66±43.45	290.23±32.22
T_e[N II]	10146±107	10046±88
T_e[O III]	10647±70	10903±92
He^{+2} ($\times10^2$)	11.42±0.14	11.68±0.51
He^{+} ($\times10^2$)	1.19±0.02	1.35±0.02
He/H ($\times10^2$)	12.62±0.14	13.04±0.51
C^{+2} ($\times10^5$)	21.50±2.65	16.81±3.28
C/H ($\times10^5$)	33.11±8.32	28.18±10
N^{+} ($\times10^5$)	9.22±0.17	10.76±0.25
N^{+0} ($\times10^5$)	0.96±0.04	1.05±0.06
N/H ($\times10^5$)	32.00±0.95	31.41±0.96
O^{+2} ($\times10^5$)	28.86±0.09	23.9±0.64
O^{+} ($\times10^5$)	12.82±3.03	13.80±3.18
O^{+0} ($\times10^5$)	5.01±0.06	5.71±0.20
O/H ($\times10^5$)	44.53±3.74	40.44±3.8
Ar^{+3} ($\times10^6$)	0.76±0.11	0.22±0.06
Ar^{+2} ($\times10^6$)	1.96±0.03	1.82±0.04
Ar/H ($\times10^6$)	3.67±0.05	3.42±0.07
S^{+2} ($\times10^6$)	1.05±0.16	1.16±0.15
S^{+} ($\times10^6$)	0.34±0.01	0.55±0.02
S/H ($\times10^6$)	1.60±0.17	1.78±0.15
Cl^{+2} ($\times10^8$)	8.02±2.48	6.83±2.67
Cl/H ($\times10^8$)	11.42±3.41	9.77±2.74
N/O	0.71±0.03	0.78±0.03
C/O	0.74±0.2	0.70±0.25

TABLE 5.3— Comparison of observed line ratios and those obtained with our CLOUDY model. Observed flux ratios are the average value of s1R1 and s1R2.

Ion	Line	Observed	Modelled
[O III]	(λ5007+λ4959)/λ4363	163.12	167.91
[N II]	(λ6548+λ6583)/λ5755	87.19	82.46
[S II]	λ6716/λ6731	1.16	1.14
C IV	λ1551	29.7	27.52
He II	λ1640	102.0	112.30
C III]	λ1909	150.0	159.20
[O II]	λ3726-29	376.0	319.30
Hγ	λ4341	46.1	47.22
[O III]	λ4363	7.8	7.90
He I	λ4471	6.2	6.18
He II	λ4686	15.8	14.56
He I	λ4922	2.1	1.66
[O III]	λ4959	322.0	332.99
[O III]	λ5007	950.3	993.5
[N I]	λ5198	7.5	10.32
[Cl III]	λ5538	0.5	0.40
[N II]	λ5755	7.7	7.44
He I	λ5876	15.3	15.98
[N II]	λ6548	166.0	155.40
H_α	λ6563	287.1	279.35
[N II]	λ6583	505.4	458.1
He I	λ6678	4.5	4.46
[S II]	λ6716	9.4	9.2
[S II]	λ6731	8.1	8.04
[Ar III]	λ7136	26.6	26.74

Note: All line intensities are with respect to $F(H_\beta) = 100.0$.

TABLE 5.4— IUE archive spectra observations of NGC 2346.

Date	Spec. No.	Exp. Time (min)	ϕ^{b}	$F_{1268-1305}$ (10^{-14} erg s^{-1} cm^{-2} Å^{-1})	$F_{1825-1845}$	$F_{2670-2750}$	Comments
81/02/06	LWR09869	90	0.78	...	...	14.7±1.98	CS.
	SWP11247	36	0.78	...	...	...	No spectrum visible.
	SWP11248	105	0.78	6.83±2.95	25.67±1.75	...	CS. Geocoronal Lyα saturated.
82/02/25	LWR12680	60	0.76	...	...	...	No spectrum visible.
	SWP16420	50	0.76	12.21±7.17	9.41±3.47	...	Underexposed.
	SWP16421	113	0.77	8.82±5.11	9.78±1.8	...	CS. Very weak continuum.
82/04/06	LWR12970	30	0.32	...	...	19.34±9.87	CS. Background radiation.
	SWP16704	40	0.31	6.08±21.22	31.53±9.65	...	Underexposed.
82/05/05	LWR13172	60	0.12	...	...	15.61±5.51	CS. Saturated 2810–2820 Å.
	SWP16895	75	0.11	...	...	...	Saturated.
82/05/13	SWP16950	120	0.61	9.21±3.09	11.66±1.55	...	CS.
82/09/05	LWR14091	60	0.80	...	...	...	No spectrum visible.
	SWP17850	120	0.79	11.41±8.08	10.83±3.46	...	Underexposed. C III] saturated.
83/04/17	LWR15756	25	0.80	...	...	...	No spectrum visible.
	LWR15757	75	0.81	...	...	...	Saturated.
	SWP19740	150	0.80	6.15±2.52	5.68±1.28	...	Underexposed. Geocoronal Lyα saturated.
	SWP19741	105	0.80	9.86±10.54	13.09±4.0	...	Underexposed.
83/04/20	SWP19768	165	0.98	10.65±6.52	10.11±1.24	...	CS. Weak continuum. Geocoronal Lyα saturated.
83/05/13	LWR15928	120	0.42	...	...	3.25±1.06	CS.
	SWP19967	180	0.42	8.21±2.16	7.68±1.08	...	CS . Geocoronal Lyα saturated.
85/02/09	SWP25202[b]	415	0.30	...	...	...	Underexposed.
85/04/30	SWP25821	160	0.33	9.52±3.44	8.39±1.81	...	CS.
85/05/08	LWP05934	60	0.83	...	...	17.08±2.12	CS.
	SWP25889	120	0.82	7.84±4.69	26.77±2.14	...	CS.
86/05/03	SWP28258	150	0.33	8.86±3.45	30.35±1.59	...	CS.
86/05/07	SWP28266	120	0.58	12.43±5.34	34.97±2.13	...	CS.
93/12/15–16	LWP27055	90	0.38	...	...	40.34±1.74	CS. Saturated 1800–1930 Å.
	SWP49603	270	0.31	10.00±2.47	37.64±1.17	...	CS. Geocoronal Lyα saturated.

[a] Phases of the binary CSPN are based on orbital elements of MN81, t_{0}=2443142.0 and 15.995 d period. The phase shown refers to the midpoint of the exposure time.
[b] High dispersion spectrum.
Note: Comments are based mostly on the visual inspection of the 2D images available in MAST (`https://archive.stsci.edu/`). Underexposed means that there is no evidence of the CS spectrum, in the 2D image and that the spectrum has data numbers (DNs) below 100 DNs above background in most of the wavelength range. Saturated means that the whole 2D image is saturated.

TABLE 5.5— UV emission lines of IUE spectra.

Spec. No.	C IV	He II	C III]
(SWP)	(10^{-13} erg s^{-1} cm^{-2})		
11248	2.60±0.76	12.69±0.81	14.96±0.48
16420	...	11.61±1.46	15.39± 1.04
16421	...	10.73±0.83	17.35± 0.62
16704	...	...	8.35± 2.31
16950	4.52±0.98	12.30±0.80	15.86± 0.47
17850	4.72±3.17	15.27±2.83	12.46± 0.65
19740	1.84±0.62	8.44±0.56	14.18± 0.47
19741	...	7.08±1.76	15.96± 1.18
19768	3.60±0.60	12.07±0.66	14.72± 0.34
19967	2.59±0.54	11.21±0.87	14.71± 0.32
25821	2.74±1.09	12.73±0.99	15.04± 0.46
25889	2.60±1.35	12.51±1.29	14.70± 0.67
28258	2.51±1.19	10.10±0.86	13.85± 0.47
28266	3.36±1.60	11.99±1.61	11.95± 0.55
49603	2.01±0.52	11.17±0.55	14.80± 0.43

5.4 Analysis

5.4.1 Stellar parameters and UV extinction determination

Our main purpose is to determine the stellar and nebular parameters, which require us to take into account concurrently and consistently the effects of reddening.

In Figure 5.3, we present all the IUE spectra found in INES database (except for those flagged with 'No spectrum visible' and 'Saturated' comments in Table 5.4). Most of the spectra include a stellar and nebular continuum, and nebular emission lines. All the spectra contain prominent C IV, He II, and C III] emission lines, which are affected by the flux variation. In the spectra in the upper panel of Fig. 5.3, which span the dates between 1981/02/06–1982/09/05, the flux is almost constant, whereas in the lower panel, the flux varies, reaching a maximum value on 1993/12/15-16 and a minimum value on 1983/05/13. The flux variation is greater around 2800 Å and is practically constant around 1300˚Å. The continuum in the LWR15928 spectrum, which presents the minimum flux, shows almost exclusively nebular emission, whereas in the LWP27055 spectrum, which presents the maximum flux, the flux is only stellar.

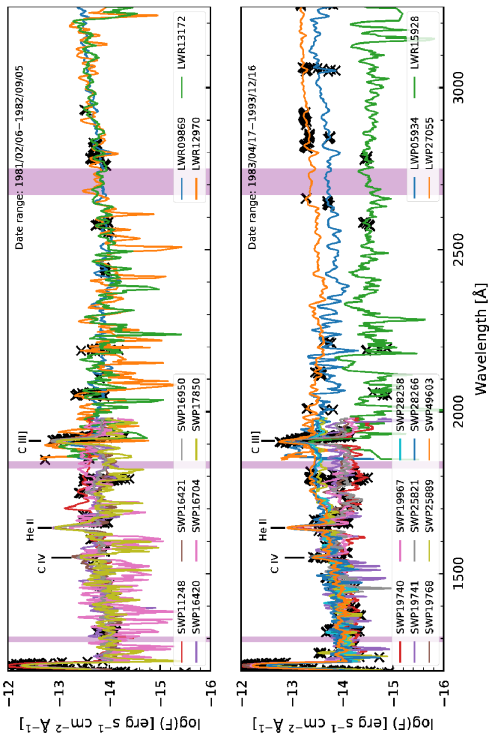

FIGURE 5.3— NGC 2346 IUE UV archive spectra. Notice that the flux is constant around 1300 Å where the flux is mainly composed by the hot-star, whereas the flux around 2300 Å varies for each epoch suggesting a strong contribution of the companion star. Black crosses indicates the bad pixel points. The purple filled bands indicates the width of the narrow bands $F_{1288-1305}$, $F_{1825-1845}$, and $F_{2670-2750}$ (see text).

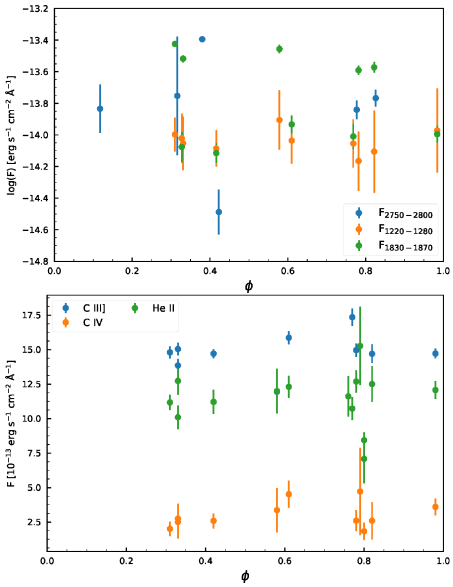

FIGURE 5.4— Integrated $F_{1288-1305}$, $F_{1825-1845}$, and $F_{2670-2750}$ narrow bands as a function of the binary CSPN orbital phase (upper panel). The $F_{1288-1305}$ band is practically constant during all phases, whereas $F_{1825-1845}$, and $F_{2670-2750}$ bands show different emission for different phases. The UV emission lines (lower panel) shows the same behavior as the integrated narrow bands. The variation is likely not related with the binary CSPN orbital period.

Figure 5.4 (upper panel) shows the integrated narrow bands $F_{1288-1305}$, $F_{1825-1845}$, and $F_{2670-2750}$ as a function of the phase (ϕ) of the binary CSPN orbital period for the spectra that show stellar continuum (marker as 'CS' in Table 5.4). In the $F_{1288-1305}$ column, the flux is practically constant. This indicates that the ionizing source of the CSPN is not varying, as opposed to

its A-type star companion in the optical range (Costero et al., 1986; Peña & Hobart, 1994). The flux of the IUE spectra varies for a different values of ϕ, as shown by the integrated narrow bands $F_{1825-1845}$ and $F_{2670-2750}$. Figure 5.4 (lower panel) shows the emission lines as a function of ϕ. Although emission lines vary by a factor of ~ 2.5, the flux increases with increasing ϕ. In both cases, the variation, either for the narrow bands or for the emission lines, is not correlated with ϕ. In fact, we can see a maximum brightness near 1993/12/15-16 ($\phi = 0.38$) and a minimum near 1983/05/13 ($\phi = 0.42$), the flux on 1993/12/15-16 being ~ 13 times brighter than on 1983/05/13 in the $F_{2670-2750}$ band (Table 5.4). This difference is comparable with the light variation obtained by Costero et al. (1986), being of $\sim$2 mag in the optical range. It is very likely that the light variations seen in the IUE spectra are related with the flux of the A-type star, as suggested by Feibelman & Aller (1983). Nevertheless, we have to take into account that the IUE spectra is taken through a $10 \times 20''$ aperture, and that the flux could be the sum of a hot-star and nebular continuum emission, and the A-type star.

For the reddening analysis we choose the IUE spectra in which the contribution of the A-type stellar companion flux is not present and where the CS continuum is evident. As judged from our Table 5.4 and our Figure 5.3, the best spectra are SWP19967 and LWR15928. We have analyzed the SWP19967 and LWR15928 spectra, fitting non-LTE plane-parallel TLUSTY (Hubeny, 1988) models, which are suitable for high $T_{\rm eff}$ and high gravity stars. If the IUE flux comes solely from a hot stellar source, its shape would depend on stellar $T_{\rm eff}$, $\log(g)$, and interstellar extinction. Using TLUSTY models, the UV continuum can be matched by a hot model with $T_{\rm eff}$=125 000 K and reddening values of $E(B-V)$ in the range 0.4–0.6. The exact $E(B-V)$ value depends on the stellar model, but under the assumption that the flux is only stellar, no acceptable fit can be found for $E(B-V) < 0.4$ mag (Fig. 5.5) using the extinction law of CCM89. At a distance of 1400^{+93}_{-81} pc (Gaia DR2), a model with $T_{\rm eff}$=125 000 K and $E(B-V)$=0.5 mag, the fits in Figure 5.5 (upper panel) imply a radius for the CS of $R = 0.10 \pm 0.03\,R_\odot$.

We have also compared the optical magnitude for a A5V stellar companion with Kurucz models consistent with A5 types. But a reddening of $E(B-V) > 0.4$ mag would imply that the A5 star should have luminosity class corresponding to a giant star according to its optical magnitude.

However, if the IUE spectrum contains a nebular continuum contribution, the TLUSTY model + nebular continuum will need less reddening to fit the IUE spectrum. To explore this possibility, the IUE spectrum was fitted with the sum of the hot star and nebular continuum, as obtained from our photoionization model in Section. 5.3.5, reddened with $E(B-V) = 0.18$ (see lower panel of

Fig. 5.5). The hot star was scaled to match the 1250 Å flux (since this region is less affected by nebular continuum), whereas the nebular continuum was scaled in such a way that the sum of the hot-component + nebular continuum matched the 2600 Å flux. The corresponding scaling factor imply a radius for the hot star of 0.019 $R_\odot$.

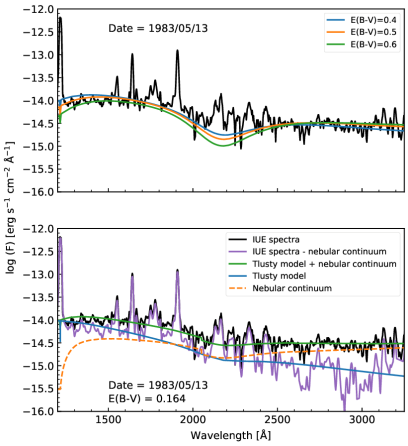

FIGURE 5.5— NGC 2346 IUE archival spectral (black), and TLUSTY model with $T_{\rm eff}$=125 000 K, reddened with different amounts of extinction (see legend, upper panel). The three reddened models have been scaled to match the observed flux at 2600 Å; the corresponding scaling factors imply a radius for the hot star between 0.071 and 0.130 $R_\odot$, using the distance from the Gaia DR2 catalogue. If the IUE spectra are the sum of a hot-atmosphere and a nebular continuum, we can fit the observed spectra with a lower reddening value (lower panel). We computed a nebular continuum using the TLUSTY model with typical abundances and nebular parameters with the CLOUDY code. All model components were reddened using $E(B-V) = 0.18$ and then, the hot-component was scaled to match the 1250 Å (since this region is less affected by nebular continuum), whereas the nebular continuum was scaled in such a way that the sum of the hot-component + nebular continuum matched at 2600 Å; the corresponding scaling factor implies a radius for the hot star of 0.019 $R_\odot$.

TABLE 5.6— Stellar parameters of the A5IV companion and the CSPN.

	A5IV companion	CSPN
$T_{\rm eff}$ [K]	8065 ± 180	130 000
$\log(g)$	3.43 ± 0.10	7.0[a]
Mass [$M_\odot$]	2.26 ± 0.32	$0.7^{+0.2}_{-0.3}$
Radius [$R_\odot$]	4.8 ± 0.3	0.019
Luminosity [$L_\odot$]	87.82 ± 11.84	170
Orbital separation [AU]	0.180–0.189	
$E(B-V)$ [mag]	0.18 ± 0.01	

[a] Fixed in the photoionization model.

5.4.2 UV flux analysis

As mentioned in the introduction, eclipses in the A5IV star brightness are observed in the IUE spectra (Feibelman & Aller, 1983) and in optical magnitudes (Kohoutek, 1982). Such eclipses are presumed to be caused by obscuring dust clouds (Schaefer, 1985) or an ellipsoidal cool dust cloudlet (Costero et al., 1986). Since this does not affect the CSPN (as seen in Fig. 5.3) and the nebular continuum may not vary (the PN is a much larger region than the orbital separation of the stars) we may infer the stellar radius of the A5IV star by subtracting the minimum (date 1993/12/15–16) from the maximum brightness (date 1983/05/13) spectra detected in the IUE spectra (see Fig. 5.6 upper panel). This is

$$(IS + NC + A)_{\rm max} - (IS + NC)_{\rm min} = A \tag{5.2}$$

where IS is the ionizing star brightness, NC is the nebular continuum emission, and A is the A5IV star brightness. Scaling a solar-composition Kurucz stellar model, using the values for $T_{\rm eff}$ and $\log(g)$ found from the fit of the Balmer lines, for the Gaia distance, we obtain the stellar radius of the A5IV star. We found the stellar radius to be R=4.8±0.3 $R_\odot$ or R=8.8±0.5 $R_\odot$ for $E(B-V)$ of 0.18 and 0.4, respectively. The filled areas in the lower panel in Fig. 5.6 represent the obtained errors in $T_{\rm eff}$ and $\log(g)$. Nevertheless, the major uncertainty is related to the 7% error in the distance from which the radius errors were calculated.

Using $E(B-V) = 0.18$, derived from the nebular line ratios and the Gaia DR2 distance, values for the A5IV star, as shown in Table 5.6, are $R = 4.8 \pm 0.3\,R_\odot$, $M = 2.26 \pm 0.315\,M_\odot$ and $L = 87.82 \pm 11.84\,L_\odot$. This radius for the A5IV star suggests that it has already been evolved off the main-sequence.

In Figure 5.7 we present the result from the IUE spectral flux decomposi-

tion into different emission components from the photoionization model: the nebular emission, the A5IV companion, and the CSPN for different epochs (see, Table 5.4). The observed spectra were de-reddened using $E(B-V) = 0.18$ and CCM89 extinction law. The CSPN emission was fitted to match the 1250 Å region and the nebular continuum was fitted around 2600 Å in the spectrum in which no contamination of the A5IV star was observed (Date 1983 May 13). We only varied the A5IV star continuum since the eclipses do not affect the hot-star and nebular continuum emission. Most of the spectra can be explained with our assumptions for all components by varying the A5IV companion. The flux variation (of 2.88 mag) of the A5IV companion is consistent with the value observed by Costero et al. (1986).

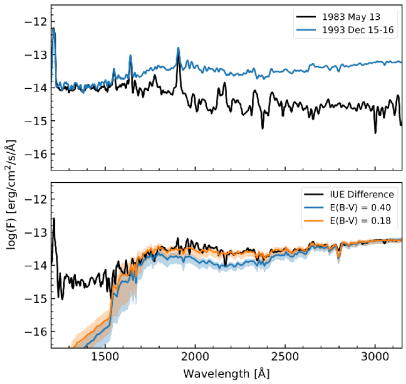

FIGURE 5.6— IUE spectral data from different epochs for the maximum and minimum brightness variation observed (upper panel) for the companion A5 star. The difference between the two epochs was fitted using Kurucz stellar models according to the range of $T_{\rm eff}$ and $\log(g)$ (solid line represent the middle value and were filled between maximum and minimum values), and Gaia DR2 distance. The two extinction values discussed in the text are labeled in the figure (lower panel). The radius estimated were 4.8 $R_\odot$ and 8.8 $R_\odot$ for extinction of 0.18 mag and 0.4 mag, respectively.

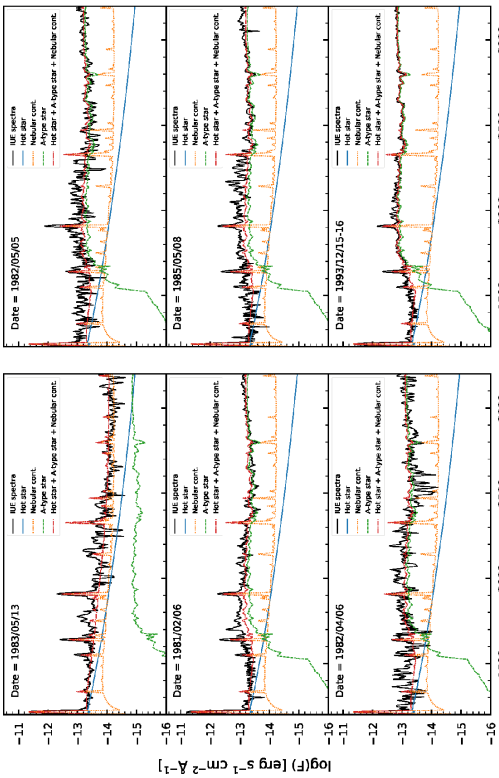

FIGURE 5.7 — AIV variation of the binary CSPN of NGC 2346 using de-reddened ($E(B-V) = 0.18$) IUE archive spectra. The different flux components are labelled in the figure as well as the corresponding date of observation. There is no evidence of a relationship between phase of the binary orbit and eclipses of the A5IV star.

5.5 Discussion

We estimated the extinction based in two methods: with nebular emission lines and with UV flux from the CSPN. Our analysis of the IUE flux, accounting for CSPN continuum, nebular continuum, emission lines, and A5IV companion, yield an upper limit for the extinction ($E(B-V) = 0.18 \pm 0.01$).

Our results of nebular density $n_e \approx 200\,\mathrm{cm}^{-3}$ of NGC 2346 suggest that the torus-like feature in the central region is probably a projection effect. This is also supported by the study of Manchado et al. (2015), who found that the torus-like shape is formed by clumps and cometary knots with sizes of 225–470 AU (we rescale their results with Gaia distance). Such knots and clumps could also be related with the drop in brightness of the A5IV star.

Schaefer (1985) postulated that the variability can be explained by a cloud of material moving across the line of sight, which was part of the shell ejected by the compact star. This is supported by a blue-shifted component of C IV λ1550 (Roth et al., 1984), with a radial velocity of $\approx$1000 km s^{-1}, which is not present in the [C III] λ1909, indicating that the blue-shifted emission becomes from a very hot region presumably near the surface of the CSPN.

Temperature and luminosity for the ionizing star from the photoionization model are $L \approx 170\,L_\odot$ and $T_{\rm eff} \approx 130,000$ K. Although these values can not be used as an unique solution owing to the optimization process developed in CLOUDY (which means that other possible solutions could satisfy our observations), such values are in good agreement with those predicted by Feibelman & Aller (1984); Calvet & Cohen (1978) and more recently by Manchado et al. (2015).

Manchado et al. (2015) calculated the mass of the ionizing star, being of 0.32–0.72 $M_\odot$ for a range of inclination angles (120±25 deg with respect to the line of sight). Their results are based in the assumption that the companion star was a A5V and a distance of 700 pc. For an A5IV secondary, with mass of 2.26±0.31 $M_\odot$, using the Gaia DR2 distance, the range of mass for the primary is 0.41–0.90 $M_\odot$. This gives a range for the orbital separation of 0.180–0.189 AU (38.70–40.64 $R_\odot$). It is then likely that the system passed through a CE phase, in which the initial orbital separation decreased, since the ionizing star should have already reached a radius larger than the orbital separation during its AGB (or even in the RGB) phase. We may infer, as Manchado et al. (2015) did, that NGC 2346 did not result in a merger and that the minimum mass of the PN progenitor should be greater than the mass of the A5IV companion during its main-sequence phase.

The A5IV star companion in the CSPN shares the same systemic velocity, ruling out the possibility for a foreground object. Arias et al. (2001) obtained

a PN kinematical age of ∼3500 yrs (assuming a distance of 700 pc) from the near-IR H_2 lines, whereas (Espinoza-Zepeda et al., in preparation) obtained an age of ∼17000 yrs by using high-resolution optical spectra, from the nebular gas, and Gaia DR1 distance (1.285 kpc) to model the system (∼ 18000 yr with Gaia DR2 distance). The kinematical age of the system suggest that NGC 2346 CS should be in the constant-luminosity phase in the H-R diagram, whereas the luminosity of the CSPN suggest that is located in the white dwarf cooling phase, and could be starting the final shell flash (Iben et al., 1983; Schaefer, 1985). The discrepancy between the kinematical age and the age of the CS could be explained by the CE phase. The system would have likely evolved through the CE phase faster than for a single star, reaching its critical effective temperature (at least 30 000 K to ionize the nebula) within 10 000 yrs after the CE remnant (Iben & Tutukov, 1993). The low luminosity could also be explained by the CE since the luminosity of the remnant when emerging from the CE phase is essentially the same at the start of the CE phase. We argue that the CE phase must have started in the AGB phase, since this would give the progenitor enough time to build up a large CO core to sustain the photoionization of the nebula (Manchado et al., 2015). From Vassiliadis & Wood (1993) evolutionary tracks, the initial mass of the ionizing star, with L=170 $L_\odot$, is close to 3.5 $M_\odot$, which is consistent with a remnant of ≈0.75 $M_\odot$. This is consistent with the chemical abundances derived in section 5.3.4, that indicate a mass larger than 3 $M_\odot$, and probably between 3.5 and 4.5 $M_\odot$ for the progenitor star.

Not enough information exist related to the nebular abundances for a post-CE phase (see De Marco, 2009, for a review). We derived ionic and elemental abundances from our low-resolution optical spectra. From imaging, NGC 2346 could be considering a Type I PN (Corradi & Schwarz, 1995), although, the ratio of N/O is less than 0.8. This also may be an indication that the binary system has passed through the CE phase (e.g., Jones et al., 2015) since it is known that the binary interaction is capable to cut short the chemical evolution for high-mass progenitor stars (De Marco, 2009).

Inference concerning the system's evolutionary stage has drastically changed with the direct distance determination from Gaia, leading to a re-classification of the A-type stellar companion as a sub-giant star and the obtaining of the stellar parameters of the CSPN. The results suggest a binary system which evolved to a PN passing through the CE phase, with a A5IV companion star that has evolved off the main-sequence. The orbital period, close to 16 days (**?**), unusually high for objects supposedly evolved in a CE scenario, will provide an interesting case study for future CE evolution studies.

6

Conclusions

We summarize the main findings of the thesis.

6.1 Catalog of Planetary Nebulae detected by GALEX and optical corollary data

A photometric catalog of PNe covering a unique spectral range from UV to optical wavelengths was made (1340−10 838 Å) using the GALEX GR6/7 UV matched to SDSS DR14 and PS1 MDS optical surveys. Out of the 3687 coordinates of PNe taken from public PN databases, only 328 unique PNe are in GALEX, SDSS, and PS1 MDS surveys.

The PNe contained in our catalog, called `GPNcatxSDSSDR14xPS1DR2`, were separated in resolved and unresolved objects in GALEX imaging where resolved objects are all PNe with sizes at least twice the resolution of GALEX (5 ″). We analyze the different aperture magnitudes provided by the GALEX pipeline and found that, by comparing known PN diameters from previous catalogs (included in our catalog), the difference `NUV_MAG_APER_4`−`NUV_MAG_APER_5`>0 is a good indicator of a resolved PN. A total of 222 PNe are classified as resolved objects that have optical counterparts in SDSS and/or PS1, while only 106 PNe are unresolved. For those resulted resolved in GALEX imaging, we extracted the CS flux using aperture photometry techniques. Since SDSS and PS1 MDS only covered the northern hemisphere, we obtained new photometric optical observations (at LCO) of 13 resolved PNe in GALEX images located in the southern hemisphere.

The final catalog, GPNcatxSDSSDR14xPS1, contain a total of 8917 rows, which includes the multiple measurements and multiple matches found for each PN in PNcat in a 5 ″ match radius. We ranked each multiple measurement according to its distance to the PN and classified them using the tag `PNRank` for the unique and primary PN UV-optical counterparts (`PNRank=0 and 1, respectively`), "repeated" measurements (re-observations; `PNRank`=2), and field stars (`PNRank>2`).

In general, for statistical analyses, taking `PNRank`=0–1, may result in the requested PNe measurements. However, for individual SED analysis, each PN should be treated carefully as the catalog may contain fluxes from nearby objects to it. Also, special attention should be made when for a given GALEX source multiple SDSS or PS1 matches are found. This may indicate that the GALEX flux is a composition of at least two stellar sources that are not resolved by GALEX.

6.2 Characterization of binary central stars of Planetary Nebulae detected by GALEX

We have analyzed the SED of 23 resolved PNe in GALEX images, as found in our catalog `GPNcatxSDSSDR14xPS1DR2` (`galexType`=1), so that the CS flux can be measured. A binary CSPN is composed by the ionizing star (hot-star with $T_{\rm eff}$>35 000 K) and a cool companion (mostly main-sequence stars) and although the main-sequence star is dim compared to the CS flux, they can be still detected in a spatially unresolved binary system (i.e., no visual binaries). This is because the CS radiates mostly at UV wavelengths, while the main-sequence stars mainly radiates at optical and near-IR wavelengths (optical excess). Hence, the PNe sample was selected according to their position in color-color diagrams; PNe with optical or IR excess and the PNe with faint and extended envelopes.

We have constructed a program to identify and characterize single and binary CSPNe based on the MCMC method. The color indexes of the observed CSPNe were used as an input to the MCMC program to fit the stellar parameters of the CSPN, which makes the fitting procedure independent of the distance to the PN. We divided the sample into two groups, the first group composed by all PNe at |b| >15 and the second one with all PNe with known GAIA distances. A binary fraction of 85% and 40% was found for the first and second group, respectively, with a global binary fraction of 63%, which is similar to the one obtained in previous works.

Note that with this analysis made here with UV and optical bands is possible

to identify binary systems composed by a hot-WD and a cooler companion.

Out of the 14 binary CSPNe characterized, seven are new binary CSPNe candidates: PN G019.8−23.7, PN G144.3−15.5, PN G171.3−25.8, PN G270.1+24.8, PN G291.4+19.2, PN G144.5+06.5, and PN G326.7+42.2.

6.3 Grid of spectral energy distribution of Planetary Nebulae in UV-optical broad bands

We have characterized the position of unreseolved PNe (in GALEX images) and PNe with binary CS in color-color diagrams by constructing a grid of SED of PNe with the photoionization code CLOUDY, and obtaining synthetic magnitudes in the UV and optical bands. A comparison of our model colors with other theoretical and observed colors for different astrophysical objects was made to identify the position of PNe in the color space. The photionization models were made following theoretical evolutionary post-AGB tracks with initial masses of 1 $M_\odot$ and 2.5 $M_\odot$ for four different evolutionary stages during the PNe evolution. We found that all the PNe model colors are separated from those of any other astrophysical object, specially at GALEX FUV−GALEX NUV> -1 and SDSS r−SDSS $i < -0.4$. Using this color-color diagram was also possible to identify PNe with binary nuclei composed by a hot-WD and a giant or supergiant companion. The colors of the PNe models are in agreement with those observed in the unresolved PNe, as extracted from `GPNcatxSDSSDR14xPS1DR2`, in the color-color diagrams with a combination of colors that are less affected by reddening (e.g., GALEX NUV−NUV and SDSS $r-i$).

The intervening dust poses a severe problem for observing and identifying binary objects with photometric colors. The interstellar extinction will dim and redden an object, changing its position in a color-color diagram. In fact, an overestimation of $E(B-V)$ will cause that any companion's contribution to the overall flux to be reduced in the dereddening process. However, the colors we used here, GALEX FUV−GALEX NUV and SDSS r−SDSS i, are not very sensitive to moderate amounts of extinction making these colors ideal for PNe characterization.

The methodology and results presented in this work demonstrate the potential of using synthetic optical PNe spectra and a set of filters to produce accurate magnitudes and colors. However, we have only taken into account PNe with initial masses of 1 $M_\odot$ and 2.5 $M_\odot$. The extension of these models to a broader range of progenitor masses would provide a better understanding of the distribution of single and binary PNe.

6.4 The central star of NGC 2346, as a clue to binary evolution through the common envelope phase

NGC 2346 is a bipolar PN with a single-lined spectroscopic binary CS with an orbital period of 16 d; one of the few well studied binary CSPN in the literature. However, discrepancies in the characterization of the binary CS from different authors were found and, as a consequence, the evolutionary stage of NGC 2346 was unclear.

The SED analysis and the use of IUE spectra for different epochs in conjunction with low- and high-resolution optical spectra, allowed us to solve the discrepancy of the extinction values reported in the literature to find a value of $E(B-V) = 0.18 \pm 0.01$. We reclassify the A5 companion (which was previously classified as a main-sequence star) luminosity class as A5IV and find that it probably evolved off the main-sequence due to its stellar radius ($4.8\,R\odot$), mass ($2.26\pm0.315\,M\odot$), and micro-turbulence($3.28\,km\,s^{-1}$).

We have derived $T_{\rm eff}$=130 000 K and L=170 $L_\odot$ for the CSPN of NGC 2346 obtained from a photoionization model based on observed nebular abundances and emission lines. We propose that the CSPN of NGC 2346 has evolved trough the CE phase owing to the inferred orbital separation and the insights found in the disparity of the evolutionary and kinematical ages.

7

Future Work

This thesis has been centered in the topic of binary CSPNe, which was additionally separated in three different studies. First, we have compiled a UV-optical photometric catalog of PNe using GALEX, SDSS, and PS1 databases. A curve-of-growth analysis was made to each PNe to separate the resolved PNe from the unresolved ones. The contribution of the nebular emission lines was also analyzed and the flux of the CS was extracted for the resolved PNe. Second, we developed an MCMC program to fit the SED of the extracted CS that displayed an optical color excess as a signature of a binary component. Third, we analyzed the single PNe and those with binary nuclei in a more general way by using a photoionization code to compute a grid of synthetic SED of PNe. Here we enumerate a natural continuation of the work presented in this thesis.

- For the first study, we propose a broader investigation of the Galatic PNe population included in the GALEX, SDSS, and PS1 databases. For this we would need to include the fluxes of emission lines in the UV-optical range as well as the abundances derived by different authors, in order to study their chemistry and previous nucleosynthesis. The catalog includes information related to the size of the PNe, as extracted from the HASH database. However, a sound morphological study is necessary to investigate the Galactic population of PNe and completely understand the formation (e.g., aspherical PNe) and evolution of PNe (both for single and binary CS). This could be achieved with low-resolution, for abundance determination (e.g., INT telescope and IDS instrument), and high-dispersion spectroscopy observations, for radial/expansion velocities mea-

surements (e.g., 2 m telescope in San Pedro Martir Observatory and MES instrument), centered on important emission lines such as [O III] λ5007. UV-optical imaging using space-base facilities such as ASTROSAT-UVIT satellite and HST or ground-based optical telescopes, respectively, would help in the study of the structure of extended features on different wavelength ranges.

- Regarding the SED fitting process using the MCMC method, we have used only objects with GALEX both FUV and NUV data. However, it would be worth to investigate PNe with only GALEX NUV photometry in combination with optical bands. We plan to keep improving the fitting procedure and the values of $E(B-V)$ used to obtain the stellar parameters of the stars to understand better the evolution of binary CSPNe. Follow-up observations of the resulted new binary CSPNe candidates are also needed to confirm its binary nature. By the mid-end of this thesis, the PanSTARRS group made publicly available the second data release that now includes multi-epoch photometry. We have already compiled such data in our catalog but we would like to explore in more detail the flux variability for the new binary CSPNe candidates found in this thesis.

- In order to study seven binary CSPNe, found in Chapter 3, and the structure of the PNe extended emission in FUV wavelengths, an observational proposal to ASTROSAT-UVIT satellite for cycle A09 was made. This proposal, with ID A09_006, was successfully accepted for observation. The analysis of the images will be carried out once we obtain the observed images from the satellite.

- We have explored in a more general way the position of PNe in color space using a grid of synthetic SED of PNe computed with the CLOUDY code for two initial masses selected from the theoretical post-AGB tracks used. We would like to compare the resulted color-color cuts to search for new PNe and new PNe with binary nuclei using the GALEX, SDSS, and PS1 databases. Model colors of other CSPNe initial masses are needed in order to better characterize the observed PNe in the color-color diagrams. Long-term spectroscopic monitoring to the PNe located in the same color-space as the PNe with binary nuclei would be made to confirm their binary nature. We would obtain the stellar parameters with more precision once the period is known.

- Concerning to NGC 2346, is it necessary to obtain high-resolution UV-optical spectroscopy observations in order to confirm the stellar parame-

ters of both the ionizing star and the companion star. Spectroscopy observations using STIS at the HST would be needed in order to fully confirm the nature of the ionizing star, while ground-based high-resolution optical spectroscopy would be desirable to confirm the presumed A5IV spectral type of the companion.

Bibliography

Abolfathi, B., Aguado, D. S., Aguilar, G., et al. 2018, ApJS, 235, 42

Acker, A., Cuisinier, F., Stenholm, B., & Terzan, A. 1992a, A&A, 264, 217

—. 1992b, A&A, 264, 217

Acker, A., Marcout, J., & Ochsenbein, F. 1996, First Supplement to the Strasbourg-ESO Catalogue of Galactic Planetary Nebulae (SECGPN)

Allard, F., Homeier, D., & Freytag, B. 2012, Philosophical Transactions of the Royal Society of London Series A, 370, 2765

Aller, L. H., & Czyzak, S. J. 1979, Ap&SS, 62, 397

—. 1983, ApJS, 51, 211

Arias, L., Rosado, M., Salas, L., & Cruz-González, I. 2001, AJ, 122, 3293

Bailer-Jones, C. A. L., Rybizki, J., Fouesneau, M., Mantelet, G., & Andrae, R. 2018, AJ, 156, 58

Balick, B., Preston, H. L., & Icke, V. 1987, AJ, 94, 1641

Barbary, K. 2016, Journal of Open Source Software, 1, 58

Barker, H., Zijlstra, A., De Marco, O., et al. 2018, MNRAS, 475, 4504

Barría, D., & Kimeswenger, S. 2018, MNRAS, 480, 1626

Bertin, E., & Arnouts, S. 1996, A&AS, 117, 393

Bianchi, L. 2009, Ap&SS, 320, 11

—. 2014, Ap&SS, 354, 103

Bianchi, L., de la Vega, A., Shiao, B., & Souter, B. J. 2019, ApJS, 241, 14

Bianchi, L., Efremova, B., Herald, J., et al. 2011a, MNRAS, 411, 2770

Bianchi, L., Herald, J., Efremova, B., et al. 2011b, Ap&SS, 335, 161

Bianchi, L., Keller, G. R., Bohlin, R., Barstow, M., & Casewell, S. 2018a, Ap&SS, 363, 166

Bianchi, L., & Shiao, B. 2020, ApJS, submitted

Bianchi, L., Shiao, B., & Thilker, D. 2017, ApJS, 230, 24

Bianchi, L., Shiao, B., Thilker, D., Barr, R., & Girardi, L. 2018b, in American Astronomical Society Meeting Abstracts, Vol. 231, American Astronomical Society Meeting Abstracts #231, 362.01

Bianchi, L., & Thilker, D. 2018, Ap&SS, 363, 85

Bianchi, L., Rodriguez-Merino, L., Viton, M., et al. 2007, ApJS, 173, 659

Bilikova, J., Chu, Y.-H., Gruendl, R., Su, K. Y. L., & De Marco, O. 2009, IR Excesses of Central Stars of Planetary Nebulae, NOAO Proposal

Binette, L., Wang, J. C. L., Zuo, L., & Magris, C. G. 1993, AJ, 105, 797

Blanco-Cuaresma, S., Soubiran, C., Heiter, U., & Jofré, P. 2014, A&A, 569, A111

Bohigas, J. 2008, ApJ, 674, 954

Bond, H. 2000, Binary Stars in Planetary Nebulae, ed. P. Murdin, 2382

Bond, H. E. 1976, PASP, 88, 192

Bond, H. E., & Livio, M. 1990, ApJ, 355, 568

Bonnarel, F., Fernique, P., Bienaymé, O., et al. 2000, A&AS, 143, 33

Brown, A. J., Jones, D., Boffin, H. M. J., & Van Winckel, H. 2019, MNRAS, 482, 4951

Calvet, N., & Cohen, M. 1978, MNRAS, 182, 687

Cardelli, J. A., Clayton, G. C., & Mathis, J. S. 1989, ApJ, 345, 245

Castelli, F., & Kurucz, R. L. 2003, in IAU Symposium, Vol. 210, Modelling of Stellar Atmospheres, ed. N. Piskunov, W. W. Weiss, & D. F. Gray, A20

Chambers, K. C., Magnier, E. A., Metcalfe, N., et al. 2016, arXiv e-prints, arXiv:1612.05560

Chu, Y.-H., Su, K. Y. L., Bilikova, J., et al. 2011, AJ, 142, 75

Ciardullo, R., Bond, H. E., Sipior, M. S., et al. 1999, AJ, 118, 488

Coelho, P. R. T. 2014, MNRAS, 440, 1027

Corradi, R. L. M., & Schwarz, H. E. 1995, A&A, 293, 871

Costero, R., Tapia, M., Méndez, R. H., et al. 1986, RMxAA, 13, 149

de Kool, M., & Ritter, H. 1993, A&A, 267, 397

de la Vega, A., & Bianchi, L. 2018, ApJS, 238, 25

De Marco, O. 2009, PASP, 121, 316

De Marco, O., Hillwig, T. C., & Smith, A. J. 2008, AJ, 136, 323

De Marco, O., Passy, J.-C., Frew, D. J., Moe, M., & Jacoby, G. H. 2013, MNRAS, 428, 2118

Delgado-Inglada, G., Morisset, C., & Stasińska, G. 2014, in Revista Mexicana de Astronomia y Astrofisica Conference Series, Vol. 44, Revista Mexicana de Astronomia y Astrofisica Conference Series, 17–17

Douchin, D., De Marco, O., Frew, D. J., et al. 2015, MNRAS, 448, 3132

Ercolano, B., Barlow, M. J., Storey, P. J., & Liu, X. W. 2003, MNRAS, 340, 1136

Farrow, D. J., Cole, S., Metcalfe, N., et al. 2014, MNRAS, 437, 748

Feibelman, W. A., & Aller, L. H. 1983, ApJ, 270, 150

Feibelman, W. A., & Aller, L. H. 1984, in NASA Conference Publication, Vol. 2349, NASA Conference Publication, ed. J. M. Mead, R. D. Chapman, & Y. Kondo, 159–162

Ferland, G. J., Korista, K. T., Verner, D. A., et al. 1998, PASP, 110, 761

Ferland, G. J., Chatzikos, M., Guzmán, F., et al. 2017, RMxAA, 53, 385

Foreman-Mackey, D., Hogg, D. W., Lang, D., & Goodman, J. 2013, PASP, 125, 306

Frank, A., & Mellema, G. 1994, ApJ, 430, 800

Frew, D. J., Bojičić, I. S., & Parker, Q. A. 2013, MNRAS, 431, 2

Frew, D. J., & Parker, Q. A. 2007, in Asymmetrical Planetary Nebulae IV, 475–482

García-Hernández, D. A., Ventura, P., Delgado-Inglada, G., et al. 2016, MNRAS, 461, 542

García-Segura, G., Ricker, P. M., & Taam, R. E. 2018, ApJ, 860, 19

García-Segura, G., Villaver, E., Langer, N., Yoon, S. C., & Manchado, A. 2014, ApJ, 783, 74

Gawryszczak, A. J., Mikołajewska, J., & Różyczka, M. 2002, A&A, 385, 205

Gómez-Muñoz, M. A., Blanco Cárdenas, M. W., Vázquez, R., et al. 2015, MNRAS, 453, 4175

Gómez-Muñoz, M. A., Manchado, A., Bianchi, L., Manteiga, M., & Vázquez, R. 2019, ApJ, 885, 84

González-Santamaría, I., Manteiga, M., Manchado, A., Ulla, A., & Dafonte, C. 2019, A&A, 630, A150

Gray, D. F. 2005, The Observation and Analysis of Stellar Photospheres

Gray, R. O., Graham, P. W., & Hoyt, S. R. 2001, AJ, 121, 2159

Green, G. M., Schlafly, E. F., Finkbeiner, D., et al. 2018, MNRAS, 478, 651

Grevesse, N., Asplund, M., & Sauval, A. J. 2007, SSRv, 130, 105

Guerrero, M. A., Manchado, A., & Serra-Ricart, M. 1996, ApJ, 456, 651

Hall, P. D., Tout, C. A., Izzard, R. G., & Keller, D. 2013, MNRAS, 435, 2048

Harrington, J. P. 1969, ApJ, 156, 903

Hauschildt, P. H. 1999, Model Atmospheres for Novae in Outburst: Summary of Research, Tech. rep.

Hauschildt, P. H., & Baron, E. 2010, A&A, 509, A36

Herald, J. E., Bianchi, L., & Hillier, D. J. 2005, ApJ, 627, 424

Hermes, J. J., Kawaler, S. D., Bischoff-Kim, A., et al. 2017, ApJ, 835, 277

Herwig, F. 2005, ARA&A, 43, 435

Hubeny, I. 1988, Computer Physics Communications, 52, 103

Iben, I., J., Kaler, J. B., Truran, J. W., & Renzini, A. 1983, ApJ, 264, 605

Iben, Icko, J., & Tutukov, A. V. 1993, ApJ, 418, 343

Icke, V. 1988, A&A, 202, 177

Icke, V., Preston, H. L., & Balick, B. 1989, AJ, 97, 462

Ivanova, N., Justham, S., Chen, X., et al. 2013, A&ARv, 21, 59

Jones, D., & Boffin, H. M. J. 2017a, Nature Astronomy, 1, 0117

—. 2017b, MNRAS, 466, 2034

Jones, D., Boffin, H. M. J., Rodríguez-Gil, P., et al. 2015, A&A, 580, A19

Jones, D., Boffin, H. M. J., Sowicka, P., et al. 2019, MNRAS, 482, L75

Jones, D., Mitchell, D. L., Lloyd, M., et al. 2012, MNRAS, 420, 2271

Jones, D., Van Winckel, H., Aller, A., Exter, K., & De Marco, O. 2017, A&A, 600, L9

Juan de Dios, L., & Rodríguez, M. 2017, MNRAS, 469, 1036

Kaler, J. B., Aller, L. H., & Czyzak, S. J. 1976, ApJ, 203, 636

Karakas, A. I., & Lattanzio, J. C. 2014, PASA, 31, e030

Kerber, F., Mignani, R. P., Guglielmetti, F., & Wicenec, A. 2003, A&A, 408, 1029

Khromov, G. S. 1989, SSR, 51, 339

Kingsburgh, R. L., & Barlow, M. J. 1994, MNRAS, 271, 257

Kniazev, A. Y., Grebel, E. K., Zucker, D. B., et al. 2014, AJ, 147, 16

Kohoutek, L. 1982, Information Bulletin on Variable Stars, 2113, 1

—. 2001, A&A, 378, 843

Kohoutek, L., & Senkbeil, G. 1973, in Liege International Astrophysical Colloquia, Vol. 5, Liege International Astrophysical Colloquia, ed. L. Remy-Battiau, J. M. Vreux, & D. H. Menzel, 485

Kurucz, R. L. 1993, SYNTHE spectrum synthesis programs and line data

Kwok, S., Purton, C. R., & Fitzgerald, P. M. 1978, ApJL, 219, L125

Luridiana, V., Morisset, C., & Shaw, R. A. 2015, A&A, 573, A42

Luridiana, V., García-Rojas, J., Aggarwal, K., et al. 2011, arXiv e-prints, arXiv:1110.1873

Manchado, A. 2004, Astronomical Society of the Pacific Conference Series, Vol. 313, Correlation of PN Morphologies and Nebular Parameters, ed. M. Meixner, J. H. Kastner, B. Balick, & N. Soker, 3

Manchado, A., Stanghellini, L., Villaver, E., et al. 2015, ApJ, 808, 115

Martin, D. C., Fanson, J., Schiminovich, D., et al. 2005, ApJL, 619, L1

Mellema, G., Eulderink, F., & Icke, V. 1991, A&A, 252, 718

Méndez, R. H. 1978, MNRAS, 185, 647

Méndez, R. H. 1989, in IAU Symposium, Vol. 131, Planetary Nebulae, ed. S. Torres-Peimbert, 261–272

Mendez, R. H., & Niemela, V. S. 1981, ApJ, 250, 240

Miller Bertolami, M. M. 2016, A&A, 588, A25

Miszalski, B., Acker, A., Moffat, A. F. J., Parker, Q. A., & Udalski, A. 2009, A&A, 496, 813

Miszalski, B., Boffin, H. M. J., Frew, D. J., et al. 2012, MNRAS, 419, 39

Miszalski, B., Parker, Q. A., Acker, A., et al. 2008, MNRAS, 384, 525

Moreno-Ibáñez, M., Villaver, E., Shaw, R. A., & Stanghellini, L. 2016, A&A, 593, A29

Morisset, C. 2013a, pyCloudy: Tools to manage astronomical Cloudy photoionization code

—. 2013b, pyCloudy: Tools to manage astronomical Cloudy photoionization code

Morrissey, P., Conrow, T., Barlow, T. A., et al. 2007, ApJS, 173, 682

Osterbrock, D. E., & Ferland, G. J. 2006, Astrophysics of gaseous nebulae and active galactic nuclei

Parker, Q. A., Bojičić, I. S., & Frew, D. J. 2016, in Journal of Physics Conference Series, Vol. 728, Journal of Physics Conference Series, 032008

Peña, J. H., & Hobart, M. A. 1994, RMxAA, 28, 165

Peimbert, M., & Serrano, A. 1980, RMxAA, 5, 9

Phillips, J. P. 2003, MNRAS, 344, 501

Phillips, J. P., & Cuesta, L. 2000, AJ, 119, 335

Ramos-Larios, G., Guerrero, M. A., Nigoche-Netro, A., et al. 2018, MNRAS, 475, 932

Rauch, T. 2003, A&A, 403, 709

Rauch, T., Dreizler, S., & Wolff, B. 1998, A&A, 338, 651

Rebassa-Mansergas, A., Agurto-Gangas, C., Schreiber, M. R., Gänsicke, B. T., & Koester, D. 2013, MNRAS, 433, 3398

Rebassa-Mansergas, A., Nebot Gómez-Morán, A., Schreiber, M. R., et al. 2012, MNRAS, 419, 806

Reindl, N., Rauch, T., Werner, K., Kruk, J. W., & Todt, H. 2014, A&A, 566, A116

Ricker, P. M., & Taam, R. E. 2012, ApJ, 746, 74

Rodríguez, L. F., Gómez, Y., & Guzmán, L. 2009, RMxAA, 45, 85

Roth, M., Echevarria, J., Tapia, M., et al. 1984, A&A, 137, L9

Rubin, R. H. 1968, ApJ, 153, 761

Sabin, L., Gómez-Muñoz, M. A., Guerrero, M. A., et al. 2017, MNRAS, 467, 3056

Sandquist, E. L., Taam, R. E., Chen, X., Bodenheimer, P., & Burkert, A. 1998, ApJ, 500, 909

Schaefer, B. E. 1985, ApJ, 297, 245

Schlafly, E. F., & Finkbeiner, D. P. 2011, ApJ, 737, 103

Schlegel, D. J., Finkbeiner, D. P., & Davis, M. 1998, ApJ, 500, 525

Seaton, M. J. 1959, MNRAS, 119, 81

Shklovsky, I. S. 1956, AZh, 33, 315

Smalley, B. 1997, The Observatory, 117, 338

Soker, N. 1992, ApJ, 389, 628

Sorensen, P., & Pollacco, D. 2004, Astronomical Society of the Pacific Conference Series, Vol. 313, The Binary Fraction of Planetary Nebula Central Stars, ed. M. Meixner, J. H. Kastner, B. Balick, & N. Soker, 515

Stanghellini, L., Guerrero, M. A., Cunha, K., Manchado, A., & Villaver, E. 2006a, ApJ, 651, 898

—. 2006b, ApJ, 651, 898

Stanghellini, L., & Haywood, M. 2010, ApJ, 714, 1096

Stanghellini, L., & Kaler, J. B. 1989, ApJ, 343, 811

Stasińska, G., Gorny, S. K., & Tylenda, R. 1997, A&A, 327, 736

Storey, P. J., & Hummer, D. G. 1995, MNRAS, 272, 41

Stoughton, C., Lupton, R. H., Bernardi, M., et al. 2002, AJ, 123, 485

Su, K. Y. L., Kelly, D. M., Latter, W. B., et al. 2004, ApJS, 154, 302

Sutherland, R., Dopita, M., Binette, L., & Groves, B. 2013, MAPPINGS III: Modelling And Prediction in PhotoIonized Nebulae and Gasdynamical Shocks

Taylor, M. B. 2005, Astronomical Society of the Pacific Conference Series, Vol. 347, TOPCAT & STIL: Starlink Table/VOTable Processing Software, ed. P. Shopbell, M. Britton, & R. Ebert, 29

Telting, J. H., Avila, G., Buchhave, L., et al. 2014, Astronomische Nachrichten, 335, 41

Tonry, J. L., Stubbs, C. W., Lykke, K. R., et al. 2012, ApJ, 750, 99

van Hoof, P. A. M., & van de Steene, G. C. 1999, MNRAS, 308, 623

Vassiliadis, E., & Wood, P. R. 1993, ApJ, 413, 641

Vazquez, R., Kingsburgh, R. L., & Lopez, J. A. 1998, MNRAS, 296, 564

Vejar, G., Montez, Rodolfo, J., Morris, M., & Stassun, K. G. 2019, ApJ, 879, 38

Villaver, E., Manchado, A., & García-Segura, G. 2002, ApJ, 581, 1204

Virtanen, P., Gommers, R., Oliphant, T. E., et al. 2020, Nature Methods

Weidmann, W. A., & Gamen, R. 2011, A&A, 526, A6

Werner, K., Dreizler, S., & Rauch, T. 2012, TMAP: Tübingen NLTE Model-Atmosphere Package

Williams, R. E. 1967, ApJ, 147, 556

York, D. G., Adelman, J., Anderson, John E., J., et al. 2000, AJ, 120, 1579

Zanstra, H. 1927, ApJ, 65, 50

Zhang, Y., Liu, X. W., Wesson, R., et al. 2004, MNRAS, 351, 935

Zuckerman, B., Becklin, E. E., & McLean, I. S. 1991, Astronomical Society of the Pacific Conference Series, Vol. 14, Central stars of planetary nebulae in the infrared., ed. R. Elston, 161–166

8

Appendix A: Logs of the Observations

We present the logs of our observations in Table 2.7.

TABLE 8.1— Log of the observations taken with the LCO network.

PN G	RA	DEC	UT of the observation	Filter[a]	Exp. time (sec)
243.8−37.1	05:03:02	−39:45:44	2018-01-01T21:08:19	g	40.287
243.8−37.1	05:03:02	−39:45:44	2018-01-01T21:06:25	r	40.284
243.8−37.1	05:03:02	−39:45:44	2018-01-01T21:07:22	i	40.287
274.3+09.1	10:05:46	−44:21:34	2017-04-08T12:11:27	g	900.296
274.3+09.1	10:05:46	−44:21:34	2017-04-08T12:26:55	r	900.285
274.3+09.1	10:05:46	−44:21:34	2017-04-08T12:42:26	i	900.286
283.6+25.3	11:26:44	−34:22:10	2017-04-01T07:49:50	g	899.950
283.6+25.3	11:26:44	−34:22:10	2017-04-01T08:05:19	r	899.950
283.6+25.3	11:26:44	−34:22:10	2017-04-01T08:20:47	i	899.946
286.8−29.5	05:57:02	−75:40:22	2018-01-02T20:00:52	g	900.285
286.8−29.5	05:57:02	−75:40:22	2018-01-02T20:16:19	r	900.285
286.8−29.5	05:57:02	−75:40:22	2018-01-02T20:31:41	i	900.284
291.4+19.2	11:52:29	−42:17:39	2017-04-07T09:30:07	g	900.295
291.4+19.2	11:52:29	−42:17:39	2017-04-07T09:45:30	r	900.290
291.4+19.2	11:52:29	−42:17:39	2017-04-07T10:00:55	i	900.288
308.2+07.7	13:28:05	−54:41:58	2017-04-01T10:22:12	g	100.283
308.2+07.7	13:28:05	−54:41:58	2017-04-01T10:24:17	r	100.283
308.2+07.7	13:28:05	−54:41:58	2017-04-01T10:26:27	i	100.285
309.1−04.3	13:53:57	−66:30:51	2017-04-01T10:52:32	g	100.284
309.1−04.3	13:53:57	−66:30:51	2017-04-01T10:54:44	r	100.284
309.1−04.3	13:53:57	−66:30:51	2017-04-01T10:57:00	i	100.284
316.1+08.4	14:18:09	−52:10:38	2017-04-01T11:23:01	g	100.278
316.1+08.4	14:18:09	−52:10:38	2017-04-01T11:25:07	r	100.291
316.1+08.4	14:18:09	−52:10:38	2017-04-01T11:27:17	i	100.283
326.0−06.5	16:15:42	−59:53:59	2017-04-01T15:55:26	g	100.282
326.0−06.5	16:15:42	−59:53:59	2017-04-01T15:57:37	r	100.281
326.0−06.5	16:15:42	−59:53:59	2017-04-01T16:00:01	i	100.282
329.0+01.9	15:51:41	−51:31:29	2017-04-01T12:45:23	g	100.290
329.0+01.9	15:51:41	−51:31:29	2017-04-01T12:47:24	r	100.284
329.0+01.9	15:51:41	−51:31:29	2017-04-01T12:49:31	i	100.283
331.3+16.8	15:12:51	−38:07:31	2017-04-01T12:05:12	g	8.291
331.3+16.8	15:12:51	−38:07:31	2017-04-01T12:05:40	r	8.289
331.3+16.8	15:12:51	−38:07:31	2017-04-01T12:06:10	i	8.280
349.3−01.1	17:22:16	−38:28:60	2017-04-01T14:22:16	g	100.289
349.3−01.1	17:22:16	−38:28:60	2017-04-01T14:24:23	r	100.283
349.3−01.1	17:22:16	−38:28:60	2017-04-01T14:26:33	i	100.286
358.9−00.7	17:45:58	−30:11:60	2017-05-02T12:37:32	g	100.286
358.9−00.7	17:45:58	−30:11:60	2017-05-02T12:39:44	r	100.281
358.9−00.7	17:45:58	−30:11:60	2017-05-02T12:41:50	i	100.287

[a] SDSS bands.